Future of Carbon Capture: Materials and Strategies

by

Francisco Javier Sotomayor

A dissertation submitted in partial fulfillment
of the requirements for the degree of
Doctor of Philosophy
(Environmental Engineering)
in the University of Michigan
2016

Doctoral Committee:

Associate Professor Christian M. Lastoskie, Chair
Associate Professor Terese M. Olson
Associate Professor Donald J. Siegel
Assistant Professor Ming Xu

DEDICATION

To my mother.

Thank you for convincing me this was all possible.

ACKNOWLEDGEMENTS

This work was funded in part by the National Science Foundation (Award Number: 1034116).

There are a number of people who deserve special thanks. Their contributions as mentors, teachers, and friends made this work possible.

First and foremost, I would like to thank my advisor and committee chair, Dr. Christian Lastoskie. Your mentorship and guidance has brought me successfully to this point and I will be forever grateful. I would also like to thank my committee members: Dr. Terese Olson, Dr. Donald Siegel, and Dr. Ming Xu. Your insights and suggestions have improved the breadth, depth, and impact of this dissertation in all the ways I had hoped for, but never quite imagined, when I asked you to serve on my committee. I would also like to thank current and previous research group members Christina Reynolds, Sahithya Reddivari, Margaret Reuter, Dr. Trinh Tran, Dr. Dong Hee Lim, and Dr. Qiang Dai. Your friendships have been incredibly important to me in ways I cannot even begin to describe here. Suffice to say, without all of you, this whole research thing would be incredibly boring and nothing would ever get done. I would also like to thank my family: my mom, dad, and sister. Your love has supported me over many years. Everything I am, I can attribute originally to you.

Finally, I would like to give special thanks to my wife, Lauren. I could never have finished this without your love and support. Every day I am with you is the best day of my life.

TABLE OF CONTENTS

LIST OF TABLES

LIST OF FIGURES

LIST OF ABBREVIATIONS

5MeO-ip	5-methoxyisophthalate
$5NO_2$-ip	5-nitroisophthalate
ACF	Activated Carbon Fiber
BF_4	Tetrafluoroborate
bdc	1,4-benzenedicarboxylate
bpdc	4,4’-biphenyl dicarboxylate
bpee	1,2-bis(4-pyridyl)ethylene
bpp	1,3-bis(4-pyridyl)propane
bpy	4,4’-bipyridine
btc	1,3,5-benzene tricarboxylate
CCS	Carbon Capture and Storage
CF_3BF_3	(Trifluoromethyl)trifluoroborate
CH_4	Methane
CID	Coordination Polymer with Inter-Digitated Structure
CID-5	$[Zn(5NO_2\text{-ip})(bpy)]_n$
CID-6	$[Zn(5MeO\text{-ip})(bpy)]_n$
CO_2	Carbon Dioxide
dabco	1,4-diazabicyclo[2.2.2]octane
DAC	Direct Air Capture
DFT	Density Functional Theory
dhbc	2,5-dihydroxybenzoate
dobdc	2,5-oxidobenzene-1,4-dicarboxylate
EIA	U.S. Energy Information Administration
ELM	Elastic Layer-Structured Metal-Organic Framework

ELM-11	$Cu(bpy)_2(BF_4)_2$
ELM-12	$Cu(bpy)_2(OTf)_2$
ELM-21	$Co(bpy)_2(BF_4)_2$
ELM-22	$Co(bpy)_2(OTf)_2$
ELM-31	$Ni(bpy)_2(BF_4)_2$
ELM-32	$Ni(bpy)_2(OTf)_2$
EOR	Enhanced Oil Recovery
EPA	U.S. Environmental Protection Agency
ETS	Emissions Trading Scheme
GCMC	Grand Canonical Monte Carlo
H_2	Hydrogen
H_2O	Water
HKURST	Hong Kong University of Science and Technology
HKURST-1	$Cu_3(btc)_2$
IAST	Ideal Adsorbed Solution Theory
IPCC	Intergovernmental Panel on Climate Change
IR	Infrared (e.g., infrared spectroscopy)
IUPAC	International Union of Pure and Applied Chemistry
MCC	Mobile Carbon Capture
MCC-1	Type 1 Mobile Carbon Capture. Regeneration of sorbent and compression of CO_2 occurs on-board the vehicle.
MCC-2	Type 2 Mobile Carbon Capture. Regeneration of sorbent and compression of CO_2 occurs off-board the vehicle.
MEA	Monoethanolamine
MIL	Matériaux de l'Institut Lavoisier (Material from the Lavoisier Institute)
MIL-53	A series of MOFs made up of metal hydroxides and terephthalate linkers. The specific metal is listed in parenthesis.
MOF	Metal-Organic Framework
MOF-5	$Zn_4O(bdc)_3$
N_2	Nitrogen
NO_x	Mono-Nitrogen Oxides

O_2	Oxygen
OFAST	Osmotic Framework Adsorbed Solution Theory
OTf	trifluoromethanesulfonate ($CF_3SO_3^-$)
PCP	Porous Coordination Polymer
PCC	Post-Combustion Carbon Capture
PCN	Porous Coordination Network (a.k.a. PCP)
PF_6	Hexafluorophosphate
PhIM	benzimidazolate
pre-ELM-11	$[Cu(bpy)(BF_4)_2(H_2O)_2]bpy$
PSA	Pressure Swing Adsorption
SO_x	Sulphur Oxides
SPC	Soft Porous Crystal (a.k.a. Flexible MOF)
TSA	Temperature Swing Adsorption
U.S.	United States
VSA	Vacuum Swing Adsorption
XRD	X-ray Powdered Diffraction
ZIF	Zeolite Imidazolate Framework
ZIF-7	$Zn(PhIM)_2 \cdot (H_2O)_3$

LIST OF SYMBOLS

E_i	Total Electronic Energy of DFT Optimized Component i
ΔF^{host}	Free Energy Difference between Open and Closed Structures
K_i	Henry Constant for Structure i
M_i	Molecular Weight of i
n_i	Number of Moles of Component i
$N_{max}^{(i)}$	Maximum Adsorbed Quantity of Structure i
ΔN_{tot}	Difference in Total Quantity of fluid Adsorbed
$\Delta \Omega^{os}$	Osmotic Potential Difference between Open and Closed Structures
P	Total Pressure
$P_i(w)$	Pressure of at which the Experimental Isotherm *i* has an Equilibrium Loading of *w*
Pgate	Pressure at Which the Gating Transition Occurs
Q_{st}	Isosteric Heat of Adsorption
R	Ideal Gas Constant (8.314 J/mol K)
S	Selectivity Factor
T	Absolute Temperature
ΔV	Change in Unit Cell Volume
W_{min}	Thermodynamic Minimum Work
w_{min}	Minimum Work per Unit Mass
y	Mixture Composition in the Gas Phase
y_i	Mole Fraction of Component i

ABSTRACT

Emissions of greenhouse gases into the atmosphere represent a long-term social and environmental challenge. Fossil fuels, which are the main source of these emissions, will likely continue to be used in energy production and transportation for the foreseeable future. In order to mitigate these emissions and prevent the worst potential effects of climate change, carbon capture technologies will need to achieve widespread use across various industries. To inform further development of next-generation carbon capture systems, two potential technologies were explored.

The first technology, flexible metal-organic frameworks, represent alternative materials for carbon capture. A group of flexible frameworks known as elastic layer-structured metal organic frameworks (ELMs) were chosen as a representative class. These crystalline materials have exotic "gated" isotherms which show abrupt reversible transitions from nonporous structures to porous structures through cooperative adsorption of guest molecules between layer planes. These unique materials show potential for selective CO_2 capture combined with energy efficient adsorbent regeneration.

Two aspects of CO_2 capture using ELMs were investigated in detail. First, the ability of ELMs to maintain their structure and capture performance in the presence of unwanted trace species present in flue gas streams, such as NO_x, SO_x, and water vapor, was analyzed using both experimental and computational techniques. It was found that ELMs can be tailored for robust

performance through careful choice of framework components, such as metal ion or counter ion substitution. Second, the breakthrough performance of ELMs was explored using a combination of experimental breakthrough curves and theoretical treatment. ELMs show a "stepped" breakthrough curve not seen in rigid adsorbents. These "stepped" curves are representative of the breakthrough curves of flexible frameworks and pose a potential hurdle to their use in carbon capture applications.

The second technology, mobile carbon capture, represents an alternative strategy for mitigating emissions from the transportation sector. Using a combination of techniques, the potential costs and design trade-offs associated with implementing a mobile carbon capture scheme were explored. It was found that mobile carbon capture could greatly reduce transportation emissions while being cheaper to implement than competing direct air capture schemes, which suffer from significant thermodynamic penalties.

CHAPTER 1

Introduction

1.1 Climate Change and the Need for Carbon Capture and Storage

Warming of the climate system is unequivocal. According to the Intergovernmental Panel on Climate Change (IPCC) (IPCC 2013), each of the last three decades has been successively warmer at the Earth's surface than any preceding decade since 1850. In the Northern Hemisphere, 1983 to 2012 was likely the warmest 30-year period of the last 1400 years. This warming in the climate system is above what would be expected without anthropogenic forcing. In fact, it is extremely likely that human influence is the dominant cause of the observed warming since the mid-20th century (Figure 1).

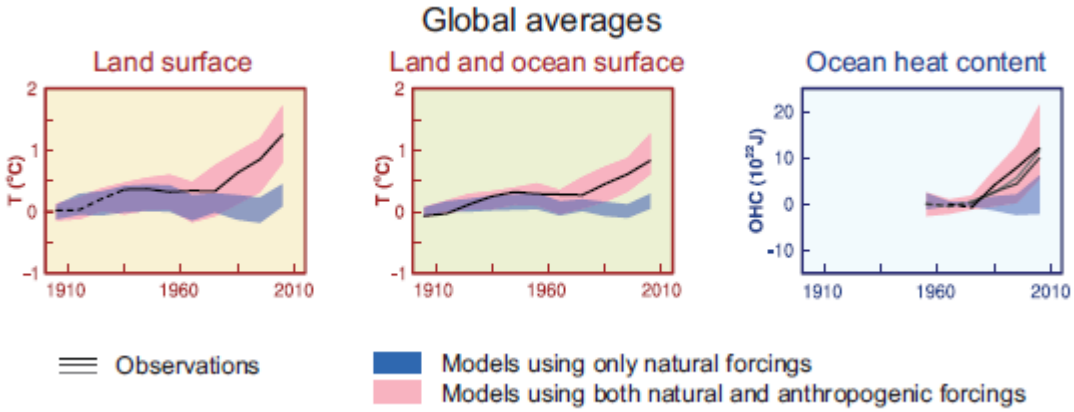

Figure 1. Global average comparisons of observed and simulated climate change based on surface temperature and ocean heat content in major ocean basins. Anomalies are given relative to 1880-1919 for surface temperatures and 1960-1980 for ocean heat content. All time-series are decadal averages plotted at the center of the decade. Model results shown are Coupled Model Inter-comparison Project Phase 5 multi-model ensemble ranges, with shaded bands indicating the 5 to 95% confidence intervals. Modified from (IPCC 2013).

Emissions of greenhouse gases into the atmosphere from anthropogenic sources have been recognized as the largest contributors to positive radiative forcing and global climate change. The IPCC (IPCC 2013) reports that atmospheric concentrations of carbon dioxide (CO_2), methane (CH_4), and nitrous oxide have increased to levels unprecedented in at least the last 800,000 years. CO_2 concentrations have increased by 40% since pre-industrial times, primarily from fossil fuel emissions and secondarily from net land use change emissions. Controlling such emissions is a long-term challenge to achieving energy and environmental sustainability.

A significant source of fossil fuel emissions is electricity generation. The U.S. Environmental Protection Agency (EPA) reports (EPA 2016) that electricity generators consumed 34 percent of U.S. energy from fossil fuels and emitted 39 percent (approximately 2,039 million metric tons) of the CO_2 from fossil fuel combustion in 2014. This is due in part to a heavy reliance on carbon intensive coal as the main fuel source for electricity production. Although it would be preferable to replace highly carbon intensive fuels like coal with low carbon intensive sources

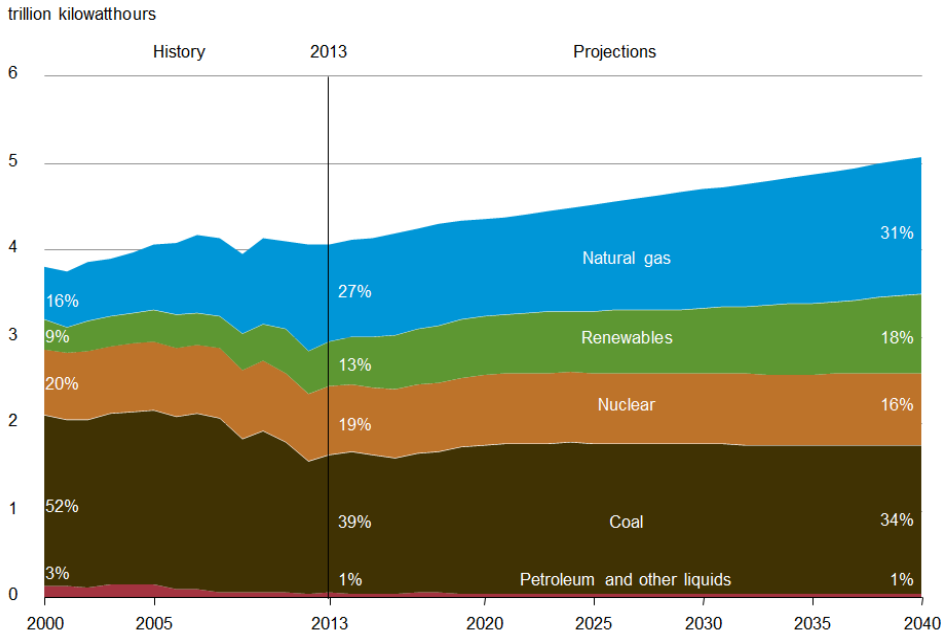

Figure 2. Electricity generation by fuel type in the U.S. (Reference Case) 2000-2040 (EIA 2015)

like renewables and nuclear, fuel switching from coal to other sources will take many years. The U.S. Energy Information Administration forecasts (EIA 2015) that coal will still make up 34% of electricity generation in the U.S. in 2040, comparable with the combined production forecast of both renewables (18%) and nuclear (16%) (Figure 2).

Even with significant effort, the low energy density and high land use commitments of renewables make it unlikely that we can replace all fossil fuel based electricity generation with wind, solar, and other renewables. Capture and storage of CO_2 will therefore be required to mitigate current and near-future emissions from existing fossil fuel based power plants. Technological roadmaps developed by the International Energy Agency (IEA 2008) depend on broad use of carbon capture and storage technology to achieve 14 to 19% of the future CO_2 emission reductions required to mitigate global climate change.

1.2 Carbon Capture and Storage Technology: Current State and Future Needs

In general, carbon capture and storage (CCS) can be considered a three-step process (Pires et al. 2011): CO_2 capture at the point of generation, compression/transport of the captured CO_2, and storage in a suitable reservoir (Figure 3). In principle, CCS can be applied to any industrial source of CO_2, such as steel, fertilizer, and cement manufacturing facilities; however, these applications have been slow to develop and current CCS research focuses on capture of CO_2 emissions from the combustion of fossil fuels at large single sources such as power plants (Haszeldine 2009).

Of the three steps in CCS, CO_2 transportation is the most mature and well understood as the technical requirements are similar to those applied to other gases (Pires et al. 2011). Indeed, several million tons of CO_2 are already transported by pipelines, due to its use in enhanced oil

recovery (EOR) fields. Effective methods of CO_2 storage are still under investigation but can be grouped into three categories (Pires et al. 2011): geological storage, ocean storage, or mineralization. Mineralization consists of the conversion of CO_2 to solid inorganic carbonates using chemical reactions. This process offers the opportunity of permanent and safe storage of CO_2 for long periods, but is high cost. Ocean storage consists of CO_2 injection at great depths where it dissolves or forms hydrates. This process accelerates the natural transfer of CO_2 to the oceans which are considered the largest repository of CO_2.

Although similar to natural processes, the increase of CO_2 concentrations in the ocean can have serious consequences in marine life. Increased CO_2 concentrations lead to ocean acidification, which can damage ecosystems like coral reefs. Geological storage options include oil and gas reservoirs, saline aquifers, and un-minable coal seams. Geological storage is considered the

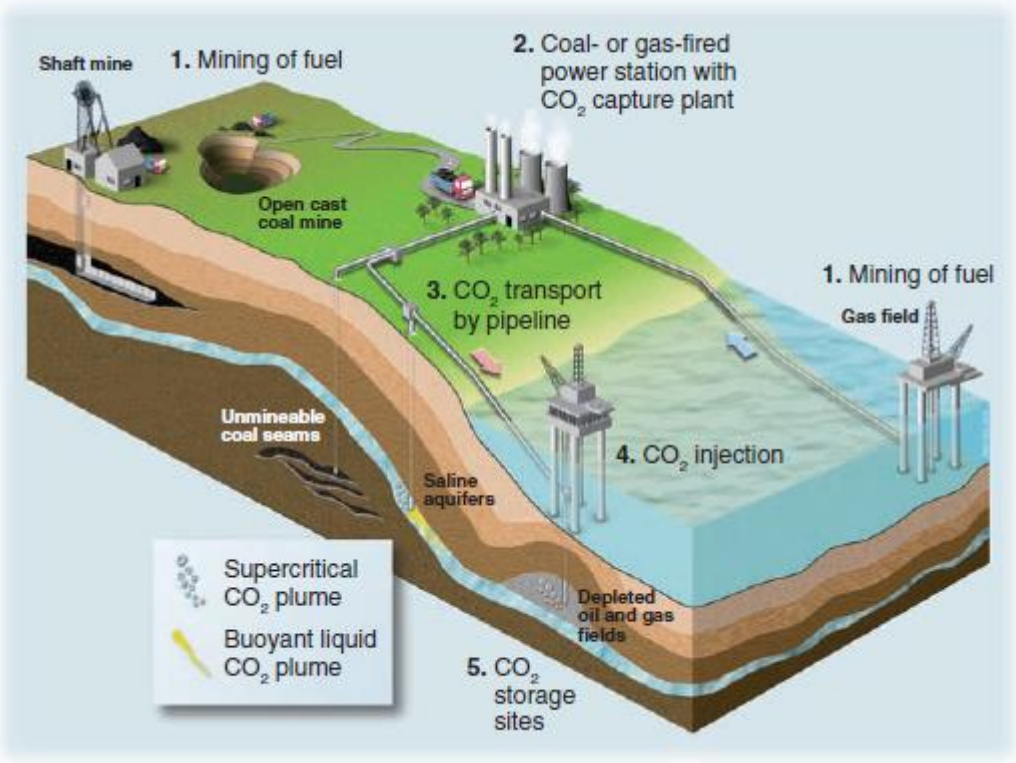

Figure 3. Diagrammatic representation of CCS incorporation into the life-cycle chain of fossil fuel use (Haszeldine 2009)

most viable option because the cost of CO_2 injection can be mitigated if combined with EOR, enhanced gas recovery, or enhanced coal bed methane recovery (Pires et al. 2011). As mentioned previously, oil and gas reservoirs are already being used to store CO_2 in EOR operations. With respect to CO_2 transport and storage, research needs are mostly focused on two areas: the impact of impurities on CO_2 transport/storage, and prevention/safety in the case of CO_2 leaks from pipelines or reservoirs.

In comparison to transport and storage, the CO_2 capture step represents the major fraction of energy consumption and cost (Haszeldine 2009; Pires et al. 2011). It is estimated that retrofitting of current U.S. pulverized-coal power plants with modern temperature-swing separation systems could result in energy penalties of 34 to 52% (House et al. 2009). The estimated cost for CO_2 capture ranges from 60 to 80% of the total cost of the CCS chain (Pires et al. 2011).

In general, CO_2 capture technologies can be divided into three technological concepts (Haszeldine 2009; Pires et al. 2011; Notz et al. 2011): post-combustion capture, pre-combustion capture, and oxy-fuel capture systems (Figure 4). Oxy-fuel technology is based on fuel combustion in the presence of pure oxygen, which is usually obtained from air using cryogenic distillation, but can be obtained through membrane separation or other processes. The resulting flue gas consists mainly of CO_2 and water vapor, which can be removed through condensation. In pre-combustion capture systems, the fuel is first converted to a mixture of hydrogen (H_2) and CO_2 through oxygen or steam reforming. The CO_2 is then separated out and the remaining pure H_2 is combusted in the power plant.

In post-combustion capture, CO_2 is separated from the flue gas stream after the conventional power plant process and flue gas treatment in an end-of-pipe process. In terms of retrofitting

current power plants for CO_2 capture, pre-combustion capture is infeasible and incorporation of oxyfuel technology is often too costly and complex. This leaves only post-combustion capture as an appealing retrofit alternative (Notz et al. 2011). The rest of this section will therefore focus on current and upcoming post-combustion CO_2 separation technology for CCS retrofit of power plants.

The main challenge that needs to be overcome in post-combustion capture of CO_2 is the low CO_2 concentration (4-14% by volume) present in the flue gas (Zhao, Minett, and Harris 2013). The low concentration of CO_2 mean that post-combustion separations require processes that are highly selective for CO_2 and can handle large volumes of gas. Figure 5 illustrates the maturity and potential for cost reduction of various proposed post-combustion CO_2 capture technologies. The underlying principles of these processes are numerous but they can be grouped into three general categories: liquid absorption processes, solid adsorbent processes, and membrane processes.

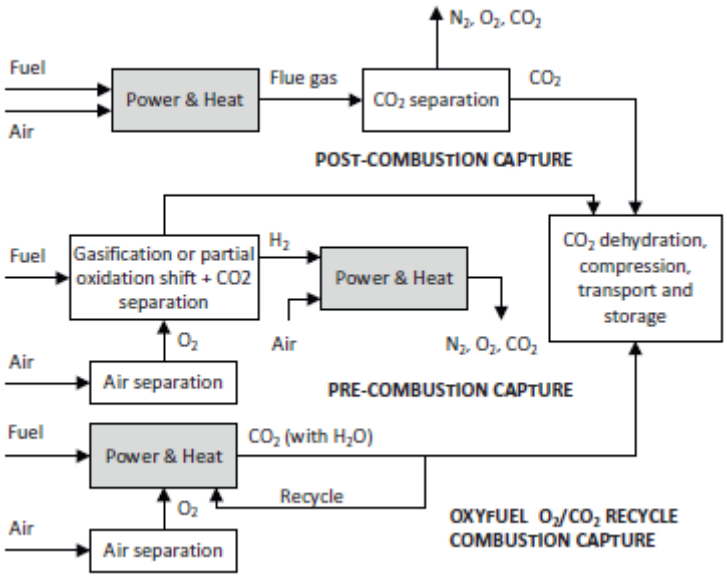

Figure 4. Technology concepts for CO_2 capture (Pires et al. 2011).

Of the three general categories, liquid absorption is the most developed. Post-combustion CO_2 capture using absorption technologies based on alkanolamines, such as monoethanolamine (MEA), have been employed industrially for over 50 years (D'Alessandro, Smit, and Long 2010). In contrast with most CO_2 capture technologies, which have yet to leave the research and development phase, MEA "wet-scrubbing" of CO_2 has been commercially demonstrated (Zhao, Minett, and Harris 2013). Due to its maturity, amine-based CO_2 scrubbing dominates the current carbon capture market and commonly serves as the benchmark against which other capture technologies are compared. However, even though they dominate the CCS literature, amine-based systems are by no means perfect. These systems have several drawbacks (Pires et al. 2011): (i) the applied solvents have limited cyclic CO_2 loading capacity; (ii) they promote corrosion of equipment; (iii) solvent regeneration requires high energy consumption; (iv) a

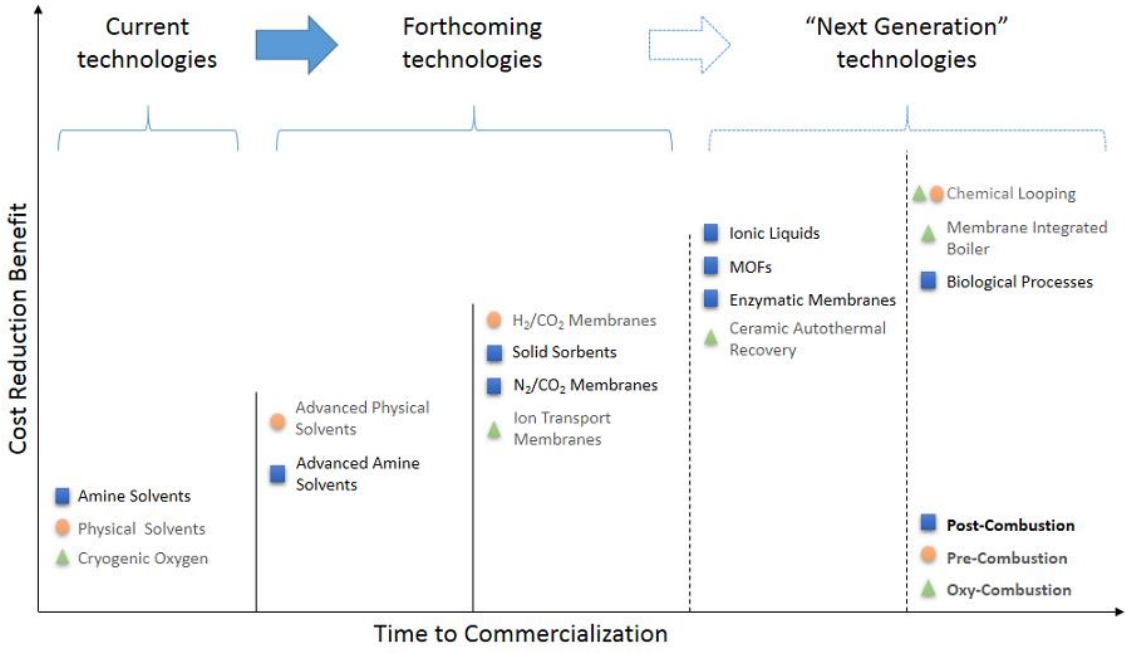

Figure 5. Current and future CCS technologies. Post-combustion technologies are bolded. Modified from (Zhao, Minett, and Harris 2013).

significant amount of solvent is lost by evaporation; and (v) the solvent degrades in an oxygen rich atmosphere. Hence, alternatives to amine absorption are sought.

A number of forthcoming CO_2 separation processes attempt to improve upon the MEA based post-combustion capture systems and are nearing commercial deployment (Zhao, Minett, and Harris 2013): (i) chilled ammonia, (ii) alkali metal carbonates, (iii) membranes, and (iv) calcium looping. Of the four technologies, calcium looping shows the greatest promise for lowering the efficiency penalties and cost of CCS retrofit. However, none of these forthcoming technologies meet the goals set by the U.S. Department of Energy for greater than 90% CO_2 capture with no more than a 20% increase in the levelized cost of electricity (Zhao, Minett, and Harris 2013). The future viability of CCS technologies will therefore depend on the development and deployment of "next generation" materials such as ionic liquids, enzymatic membranes, and metal-organic frameworks (MOFs) to further reduce the energy penalties and cost of CSS systems (Figure 5). Of the potential "next generation" carbon capture materials, MOFs are especially promising for reasons that will be elaborated upon in the next section.

1.3 MOFs for Next Generation CCS

Metal-organic frameworks (MOFs), also known as porous coordination polymers (PCPs) (Kitagawa, Kitaura, and Noro 2004), are a relatively novel class of hybrid materials built from metal ions with well-defined coordination geometry and organic bridging ligands. This coordination geometry means that MOFs have well-defined framework structures and in most cases these structures are robust enough to allow the removal of included guest species which results in permanent porosity (J.-R. Li et al. 2011). Through careful choice of metal and organic building blocks, MOFs can be conceptually designed and synthesized based on how building

blocks come together to form a net (Figure 6), allowing fine tuning of pore size and crystal structure.

Over 20,000 different MOFs have been reported and studied within the past decade (Furukawa et al. 2013). The structural and chemical diversity of MOFs has resulted in an enormous growth of research into their potential applications in gas storage, ion exchange, molecular separation, and heterogeneous catalysis (D'Alessandro, Smit, and Long 2010). The exceptional tunability of these materials has allowed MOFs to break several records in porous material properties such as specific surface areas, hydrogen (H_2) uptake by physical adsorption, and CH_4 and CO_2 storage capacity (J.-R. Li et al. 2011). Their large surface areas, adjustable pore sizes, and controllable pore surface properties make MOFs especially appealing next generation porous adsorbents for CO_2 capture. However, before they can be put into active use, MOFs must first be tuned for efficient CO_2 separation.

There are a number of suggested strategies for improving the potential for CO_2 capture of any particular class of MOFs (J.-R. Li et al. 2011): (i) optimizing pore size and shape, (ii) functionalization of the pore surface, and (iii) optimizing the framework's flexibility and dynamic response (Figure 7).

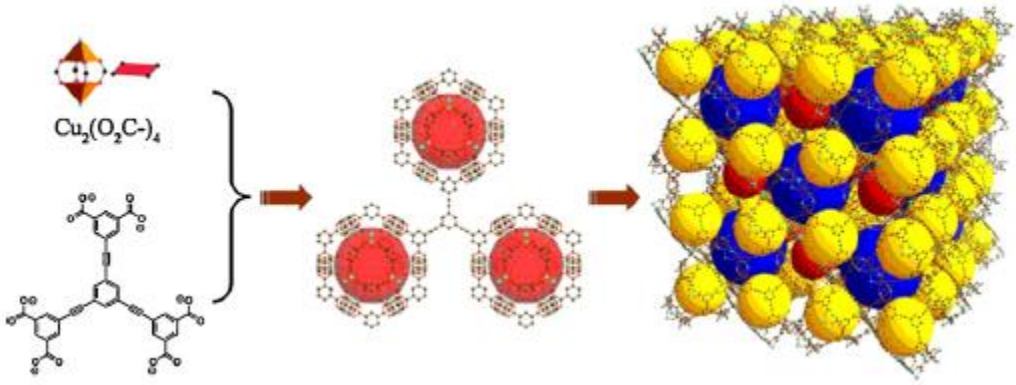

Figure 6. Construction of a designed MOF, from metal-containing node and bridging organic ligand to supramolecular building unit and then to three-dimensional framework with pores. Modified from (J.-R. Li et al. 2011).

Optimizing the pore size and geometry of a porous material is often the first step in tailoring a material for CO_2 separation. When the pore size is located between the kinetic diameters of two gas molecules (e.g., CO_2: 3.3 Å; N_2: 3.64 Å), the two gases can be separated by taking advantage of the molecular sieving effect (also called the steric effect) (Bae and Snurr 2011). Even if the pore size is not located exactly between the kinematic diameters of the two molecules, differences in diffusion in the material between the two molecules can be used to perform kinetic separation. Due to their building block nature, MOFs show great potential for controlling pore size and shape for specific separation applications.

In cases where the pore size is large enough to permit both molecules to readily diffuse into the material, separation is instead achieved based on differences in equilibrium adsorption. Under these conditions, modification of the pore surface is another strategy that can be used to increase the selective adsorption of CO_2 (Bae and Snurr 2011). In comparison to N_2, CH_4, and H_2, which are non-polar or weakly polar, CO_2 is highly quadrupolar. Inclusion of open metal

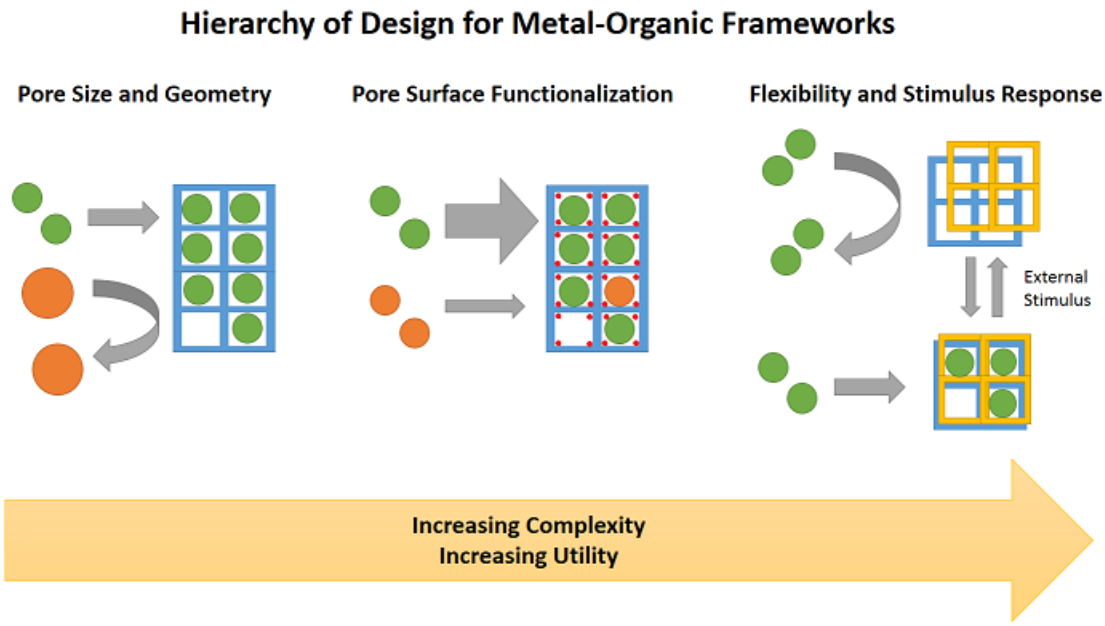

Figure 7. Hierarchy of design for selective adsorbate capture in MOFs.

sites, addition of polar functional groups, or addition of charged species on the pore surface of a MOF can therefore greatly enhance the selective adsorption of CO_2 due to increased CO_2/pore surface interaction. Although it is possible to synthesize some MOFs with already incorporated functional groups, surface functionalization is often accomplished through post-synthesis modification (Bae and Snurr 2011). For surface functional groups, this is because many functional groups may display instability under the conditions for MOF synthesis or competitively react with intended framework components. For open metal sites, post-synthesis modification is required to remove guest solvent molecules that partially coordinate framework metal atoms. Considering the two-step preparation that is often required, surface functionalization is considerably more difficult to achieve than simple pore size optimization in MOFs, but offers a great deal of potential for improving the uptake of CO_2 by MOFs and therefore their suitability for CO_2 capture. However, it should be noted that the significant increase in interaction between MOF frameworks and adsorbate molecules that can be obtained through pore surface functionalization may not benefit cyclic capture and storage processes, as increased interaction can increase the energy required to drive off the adsorbate and regenerate the adsorbent. Rana et al. (2014) investigated the usable methane storage capacity of 18 metal-substituted variants of the M/dobdc (dobdc = 2,5-oxidobenzene-1,4-dicarboxylate) series of MOFs as compared with other prominent MOFs such as MOF-5, PCN-11, PCN-14, and HKUST-1. They found that enhanced binding sites such as unsaturated metal sites, can be detrimental for pressure swing operation at higher pressures due to the tendency to retain adsorbed methane at low (desorption) pressures.

The final level of MOF design for CO_2 capture is the advantageous use of framework flexibility and stimulus-response. Flexible MOFs, also known as soft porous crystals (SPCs) (Horike et

al. 2012), are porous solids that possess both a highly ordered network and structural transformability. In contrast with rigid MOFs, which retain their structure and porosity irrespective of environmental factors, SPCs can undergo structural transformations depending on external stimuli such as temperature, mechanical pressure, or guest adsorption due to their bi-stable or multi-stable natures (Bousquet et al. 2013). This multi-stable nature of SPCs has led to the observation of previously unanticipated gas adsorption phenomena. A subset of SPCs that are representative of the class's exotic adsorption behaviors are the so-called elastic layer-structured metal-organic frameworks (ELMs) (Kajiro et al. 2010; Kanoh et al. 2009). ELMs are two-dimensional grid sheets composed of metal vertex ions, connecting ligands, and charge-balancing counter ions arranged in three-dimensional stacked structures. These materials show a latent porosity (Noguchi et al. 2005), and adsorption of gas molecules above a specific pressure, termed the "gate pressure", results in expansion of the layer planes and a vertical jump in the adsorption profile which cannot be classified into any of the adsorption isotherm categories identified by the International Union of Pure and Applied Chemistry (IUPAC) (Sing 1985).

A striking example of this class of adsorbents is the copper-based $Cu(bpy)_2(BF_4)_2$ (bpy = 4,4'-bipyridine), termed ELM-11, which shows negligible uptake of CO_2 up to a pressure of 30 kPa at a temperature of 273 K, at which point a gating transition occurs whereby the layer structure expands to accommodate significant adsorption by CO_2 molecules (Kanoh et al. 2009). The exotic adsorption characteristic of SPCs, which are not observed in traditional porous materials or in rigid MOFs, offer SPCs a number of possible advantages for CO_2 capture such as high selectivity for CO_2 and energy efficient adsorbent regeneration. For example, consider a temperature swing adsorption (TSA) process applied to the CO_2 adsorption isotherms shown

in Figure 8. Figure 8(a) shows ELM-11 isotherms at 273 K and 298 K, while Figure 8(b) shows isotherms for activated carbon fiber (ACF), a more traditional adsorbent, at 273 K and 298 K. If CO_2 at a gas-phase partial pressure of 40 kPa is adsorbed onto ELM-11 at 273 K and later recovered by heating to 298 K, nearly all of the adsorbed CO_2 is released when equilibrium is established at 298 K. If the same process is carried out using the ACF, only 40% of the captured CO_2 is desorbed. Full recovery of the CO_2 adsorbed onto ACF requires heating to a much higher temperature and thus a more costly expenditure of energy. A similar result would be obtained if pressure swing adsorption (PSA) is used instead. Depressurization from 40 kPa to 20 kPa releases nearly all of the CO_2 from ELM-11 but desorbs only a third of the CO_2 bound to the ACF.

Although the above scenario compared the specific isotherms of ELM-11 and ACF, the general conclusion can be applied to any comparison of a "gating" adsorbent with a rigid porous materials displaying a conventional IUPAC type 1 Freundlich or Langmuir class isotherm, similar to that shown for ACF in Figure 8. Tuning of stimuli induced gating or breathing effects

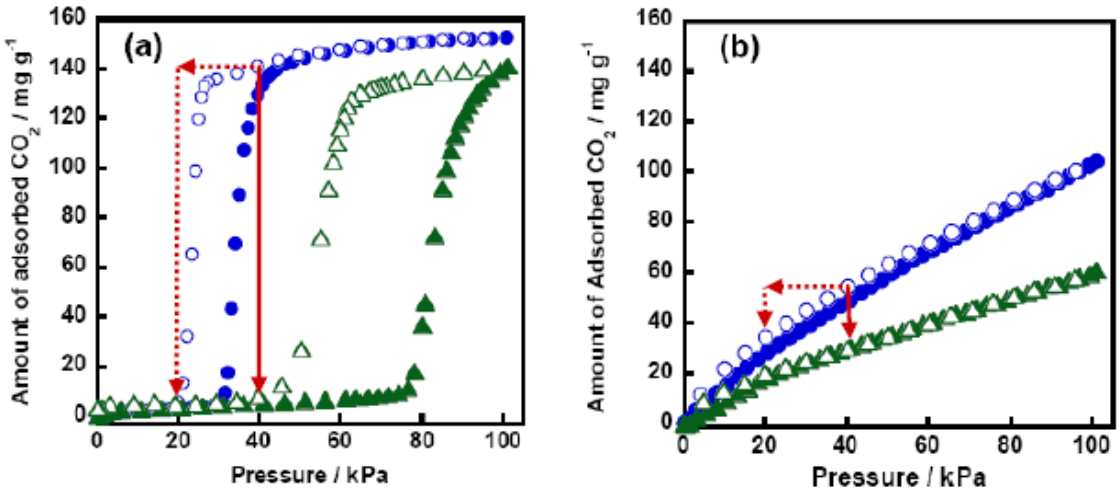

Figure 8. CO_2 isotherms on (a) ELM-11 and (b) activated carbon fiber at 273 K (circles) and 298 K (triangles). Solid and open symbols denote adsorption and desorption isotherms respectively. Solid and dashed arrows represent TSA and PSA process paths respectively. Modified from (Kanoh et al. 2009)..

in MOFs therefore shows considerable potential to lower the energy penalty of adsorbent regeneration and thus the cost of CO_2 capture. However, unlike pore surface functionalization, which is relatively well understood, framework properties which affect flexibility and stimulus response are still the matter of intensive investigation, and the impact of gated or breathing adsorption on gas separations under working conditions is still poorly understood. Given their extreme, although somewhat speculative, potential to lower CO_2 separation energy requirements and cost of the CCS process, SPCs deserve special attention above and beyond general MOFs. In order to better understand the current state of knowledge in SPC development, a review of the literature related to flexible MOFs and ELMs, as a representative class of SPCs, is carried out in the next section.

1.4 Flexible MOFs and the "Gating" or "Breathing" Phenomenon

Before the discovery of flexible MOFs and their exotic gas adsorption characteristics, adsorption isotherms could be generally classified into one of six representative types put forward by the International Union of Pure and Applied Chemistry (IUPAC) (Sing 1985). These adsorption isotherms are characteristic of adsorbents that are microporous (type I), nonporous/macroporous (types II, III, VI), and mesoporous (types IV and V) (Kitagawa, Kitaura, and Noro 2004). The IUPAC classifications are shown in Figure 9(a). ELM-11, which was first reported by Blake et al. (1997) and later characterized by Li and Kaneko (2001), was the first material to show a unique "gating" adsorption profile, shown in Figure 9(b), now considered characteristic of some flexible MOFs. This "gated" adsorption cannot be categorized under conventional IUPAC classifications. Due to the unprecedented nature of this phenomenon, research efforts of the past decade have focused on trying to understand the "gating" or "breathing" transitions of ELM-11 and other flexible frameworks.

The general chemical interactions that dictate flexibility in SPCs have been described in detail by Kitagawa and co-workers in a number of review articles (Kitagawa, Kitaura, and Noro 2004; Horike, Shimomura, and Kitagawa 2009; Kitagawa and Matsuda 2007). In general, MOFs exhibit flexibility under cases where stiff structural motifs formed from coordination bonds are connected together through weaker bonds, such as hydrogen bonds or π-π interactions. Under external stress, these weaker bonds can be disrupted, leading to displacement of the crystal structure. One representative class of SPCs are the elastic layer-structured metal-organic frameworks (ELMs), of which ELM-11 is the prime example. ELMs are made up of stiff two-dimensional layer planes, which are stacked on top of one another, and held together through hydrogen bonding between layer planes. Studies have revealed that after CO_2 adsorption, the interlayer distance in ELM-11 increases 1.20 Å (26%) from 4.58 Å to 5.78 Å. The unique "gating" adsorption isotherm of ELM-11 can therefore be ascribed to expansion/shrinkage of the layer structure, due to the apparent formation of clathrates between the lattice layers (Kajiro et al. 2010). This was further validated by later investigations of ELM framework dimensionality, where investigations of two MOFs of identical composition

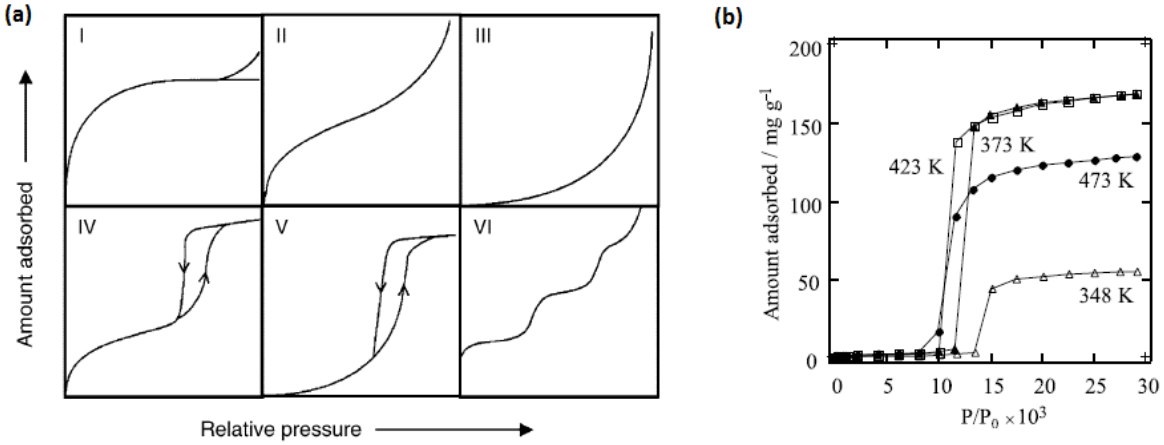

Figure 9. (a) IUPAC classification of adsorption isotherms. Image from (Kitagawa, Kitaura, and Noro 2004) (b) The unprecedented step adsorption of CO_2 on ELM-11 pretreated at different temperatures as reported in (D. Li and Kaneko 2001).

showed that the two-dimensional layered structure is necessary for gating adsorption (Kondo et al. 2011). The deviation of "gating" isotherms from traditional IUPAC classifications can now be understood to be the result of this crystal-to-crystal structural transformation as the adsorption of gas molecules shifts from surface adsorption (Type II or III) to micropore filling (Type I). This isotherm transition is shown in Figure 10.

Further investigation into the chemistry of ELMs has elucidated some of the effects of counter-ion (Kondo et al. 2007), metal ion (Kondo et al. 2009), and organic linker substitution (Fukuhara et al. 2013) on the shape of the adsorption isotherm. For example, substitution of the tetrafluoroborate ion (BF_4) in ELM-11 with the trifluoromethanesulfonate ion (CF_3SO_3 or OTf) yields $Cu(bpy)_2(OTf)_2$, or ELM-12. Since the two-dimensional grid sheet is formed by the $Cu(bpy)_2$ unit, both ELMs have a similar 2D structure. However, OTf is a bulkier counter-ion than BF_4, and cannot be accommodated as easily between the layers. Consequently, ELM-12 has a wider layer spacing than that found in ELM-11. This results in micropore filling at

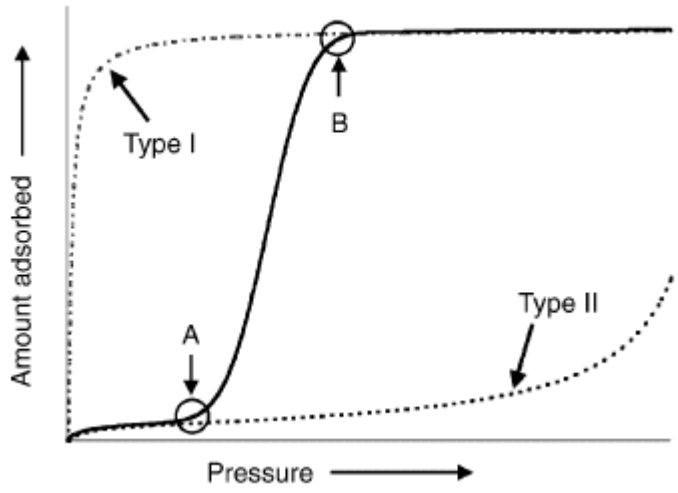

Figure 10. Isotherm transition from surface adsorption (Type II) to micropore filling (Type I) that accompanies structural transformation of a "gating" ELM. Dashed and solid lines indicate conventional IUPAC isotherms and the observed isotherm respectively. Points A and B indicate the gate-opening and gate-closing pressures which accompany the start and end of the structural transformation. Taken from (Kitagawa, Kitaura, and Noro 2004).

low pressures, which is then followed by the distinctive gating transition at higher pressures once these initial micropores are saturated. ELM-12 therefore exhibits a two-step gated isotherm for CO_2 that is distinct from the single-step gated adsorption observed in ELM-11. Replacement of the bpy organic linker in ELM-12 with the longer and more flexible bpp (where bpp = 1,3-bis(4-pyridyl)propane) results in $Cu(bpp)_2(OTf)_2$, which can once again accommodate the OTf counter-ion between its layers, resulting in a reversion to a single-step isotherm for CO_2. Therefore, the interaction between counter-ions and organic linkers is important for determining the nature of the gated transition, specifically whether it is a single-step or two-step isotherm.

Replacement of the metal ion in ELM materials does not impact the shape of the gated transition, but does impact the gating pressure. For example, replacement of the copper atom in ELM-11 with nickel results in $Ni(bpy)_2(BF_4)_2$, termed ELM-31. ELM-31 has a single step adsorption isotherm for CO_2 which is similar to that in ELM-11. However, the pressure necessary to induce the gating transition in ELM-31 is higher than that required for ELM-11. These isotherms are shown in Figure 11.

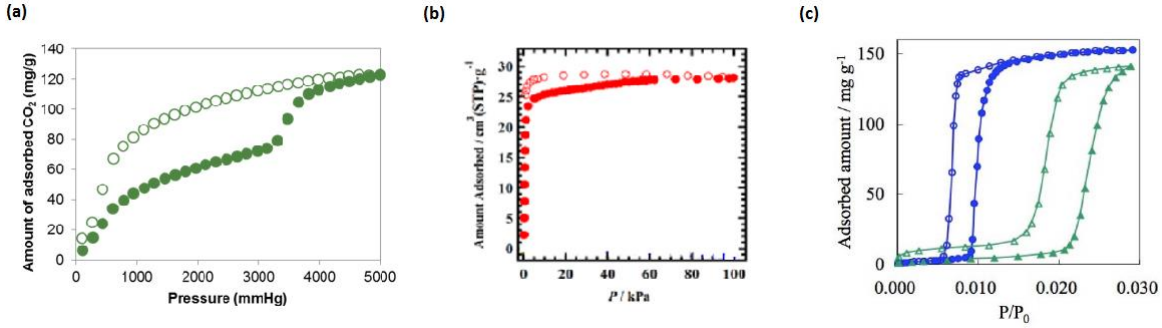

Figure 11. CO_2 isotherms on (a) ELM-12 at 298 K (green circles), (b) $Cu(bpp)_2(OTf)_2$ at 195 K (red circles); modified from (Fukuhara et al. 2013), and (c) ELM-11 (blue circles) and ELM-31 (Green Triangles) at 273 K (Kajiro et al. 2010).

Layer expansion type gated adsorption of the ELM class of materials has only been reported to date in structures containing the following building blocks (Kajiro et al. 2010; Fukuhara et al. 2013; Noro et al. 2013): (i) the metal ions Cu, Co, and Ni; (ii) the counter ions BF_4, OTf, CF_3BF_3, and PF_6; (iii) the organic ligands bpy and bpp. A closer inspection of the counter-ions show that all contain multiple fluorine atoms. The large electronegativity of fluorine atoms, and their ability to form hydrogen bonds when connected to inorganic elements, is expected to be important to the gating transition of ELMs (Kajiro et al. 2010). However, the actual role of fluorine atoms in modulating the gating transition has not been systematically explored.

In addition to the effect of building blocks, ways to modify the gating transition after synthesis have also begun to be explored. Cheng et al. (2011) explored tuning of the gate opening of ELM-11 through the post-synthesis treatment of the framework. They found that an ethanol treatment induces easier dehydration and a significant decrease in the CO_2 gate pressure.

Outside of the ELM class of materials, other authors have also looked to understand gating or breathing transitions in other SPCs. Examples include the MIL-53 series and interpenetrated frameworks. The breathing phenomenon consists of two successive adsorption-induced crystal-to-crystal transformations, from a large pore structure to a narrow pore structure and then back again to the large pore structure (Serre et al. 2002; Férey and Serre 2009). Although "gating" and "breathing" effects are not exactly equivalent, studies on the "breathing" effect do offer insight into the general thermodynamics of guest induced transitions in SPCs and offer insights for "gating" adsorbents like ELMs. In a series of articles Coudert and co-workers investigated the equilibrium thermodynamics of the adsorption induced "breathing" phenomenon of SPCs like the MIL-53 series using an analytical approach based on the osmotic statistical ensemble (Ortiz et al. 2012; Boutin et al. 2010; Coudert et al. 2008; Triguero et al.

2011; Bousquet et al. 2013; Coudert et al. 2009; Neimark et al. 2010; Coudert et al. 2011; Coudert 2010). Using this approach, they were able to predict the occurrence or absence of guest-induced breathing for a given guest-host system, the temperature-gas pressure phase diagram for several gases in MIL-53 systems, as well as breathing phase diagrams for binary mixtures of CH_4 and CO_2 in MIL-53 systems. In another approach, Miyahara and co-workers investigated the gate adsorption phenomenon of porous coordination polymers which consist of two mutually interpenetrating frameworks through an analysis of free energy profiles (Sugiyama et al. 2012; Watanabe et al. 2009). Using this approach they were able to determine stable states of the host/guest system and predict steps in the adsorption isotherm that are linked to the structural transition of the host system. The general takeaway from these investigations is that structural transitions in SPCs occur when adsorption-induced stress exerted on the material reaches a certain threshold value. This threshold value is dependent on the energy barrier for adsorption and desorption and the height of this energy barrier determines the appearance and width of hysteretic loops in the adsorption isotherms.

It is clear that a general understanding of gating transitions in flexible MOFs has been obtained. However, in terms of specific knowledge required to optimize the design of ELMs for CO_2 specific gas capture, there remain gaps. For one, an exploration of how ELMs identify and physically react to adsorbed molecules has not been fully explored. This is surprising since such studies have been undertaken to understand selective adsorption in other classes of flexible frameworks. For example, Nijem et al. (2011) used Raman/IR spectroscopy and density functional theory calculations (DFT) to explored the preferential adsorption of CO_2 over N_2 in the flexible framework $Zn_2(bpdc)_2(bpee)$, where bpdc = 4,4'-biphenyl dicarboxylate and bpee = 1,2-bis(4-pyridyl)ethylene. They were able to determine that close interaction of

CO_2 with the C-C bond in bpdc weakens the bond and allows the ligand to twist. The flexibility of the bpee pillars allows the structure to respond to the twisting, fostering the adsorption of more CO_2. In another example, Serre et al. (2007) explored the physical reasons behind CO_2 adsorption-induced breathing in the MIL-53 series using a combination of experiments and DFT calculations. They were able to determine that the weak dipolar or quadrupolar interaction of CO_2 with the hydroxyl groups in MIL-53 (Cr) on opposite sides of the pore channel, combined with strong CO_2-CO_2, interactions causes the pore structure to contract during adsorption. Understanding how the ELM framework reacts to different gas molecules and the gas molecule features that are likely to influence layer expansion will be important for designing ELMs that can selectively adsorb CO_2, while still being able to withstand decomposition due to reactive trace gases found in flue gas, such as SO_x and NO_x.

1.5 Carbon Capture Schemes for Non-Stationary Sources

Thus far, this introduction has focused on technologies that are intended for current and near-future post-combustion capture from fossil fuel based power plants. However, looking farther into the future, it is unlikely that CSS technologies will be limited to usage in the electricity generation sector. Additional carbon mitigation may require the incorporation of CCS technologies into all sectors with significant carbon dioxide emissions. The main sector of interest in this regard would be the transportation sector, which has emissions nearly comparable to the electric power sector (EPA 2016), 27% versus 31% of total emissions respectively (Figure 12).

Technologies that lower the carbon intensity of transportation have been the subject of research and government regulation for decades. In general, carbon emissions from transportation can

be factored into three relevant quantities (DeCicco 2013): travel demand activity (e.g., total vehicle miles traveled), vehicle energy intensity (e.g., fuel or energy consumption per distance traveled), and carbon intensity of the fuel consumed. Managing each of these factors requires unique strategies.

Travel demand is the result of a complex combination of factors including income and settlement patterns as well as the prices of vehicles, fuels, roads, parking, and other automobile-supporting infrastructure or services (DeCicco 2013). Vehicle energy intensity depends on the vehicle's engineering design and the driver's road behavior, which are themselves functions of technological progress, consumer tastes and incomes, fuel prices, and operational factors (DeCicco 2013). Strategies for managing travel demand and vehicle energy intensity are outside of the scope of this dissertation but include government regulations, taxes/credits and other economic incentives, and urban planning.

If travel demand and vehicle energy efficiency is held constant, reducing CO_2 emissions from transportation sources depends on reducing the carbon intensity of the fuel. Strategies for reducing carbon intensity falls into two main categories (DeCicco 2015): (1) fuel switching to

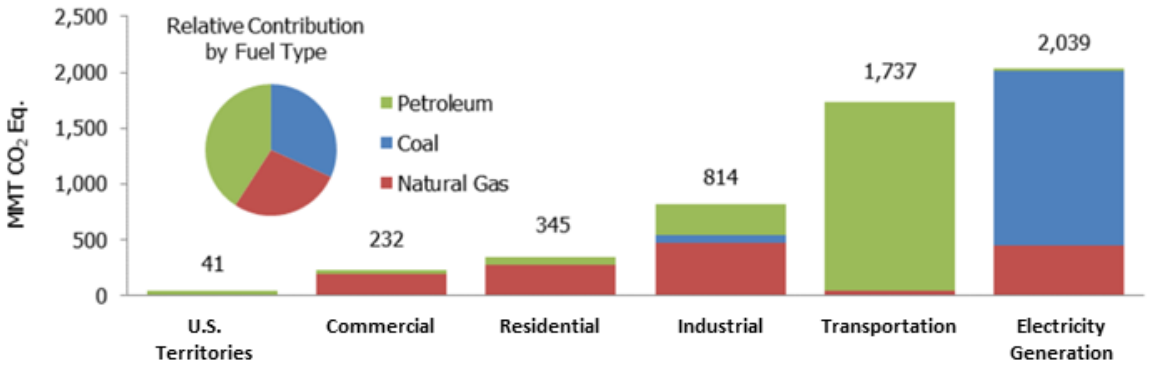

Figure 12. CO_2 emissions by sector and fuel type in 2014 (million metric tons of CO_2-eq.). Modified from (EPA 2016)

non-carbon based fuels, or (2) capturing the resulting emissions. Fuel switching includes strategies like electric cars and fuel cell vehicles. As this dissertation is focused on CCS, significant discussion of these technologies will not be included. Because of the benefits of using liquid hydrocarbon fuels, which include high energy density and an extant infrastructure, fuel switching strategies have not had a significant impact on carbon emissions from the transportation sector.

Technologies that could capture carbon emissions resulting from mobile sources have only recently been the subject of intense discussion. Carbon capture strategies for mobile sources can be separated into two categories (DeCicco 2015): atmospheric removal strategies, and on-board mobile carbon capture (MCC). Atmospheric removal strategies refer to any number of techniques, using either chemical, physical or biological means, that capture CO_2 from ambient air, where the concentration is on the order of 400 ppm (0.04%) by volume. The interested

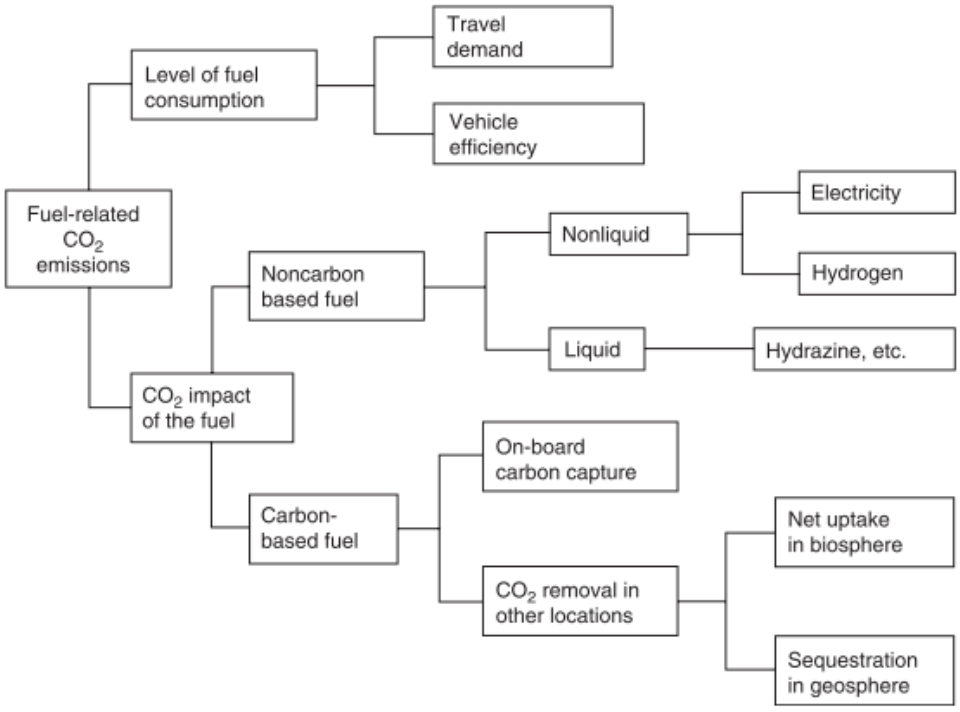

Figure 13. Logic tree for addressing CO_2 emissions from fossil fuel consumption in the transportation sector. (DeCicco 2015)

reader is encouraged to read a recent report by The Royal Society, where various atmospheric removal strategies were described in great detail in the context of geoengineering of the climate (The Royal Society 2009). Of greatest interest here is the use of physical techniques which rely on air scrubbers to perform direct air capture (DAC) as this method is grounded in the theory and practice behind CCS technologies. DAC has recently been the subject of intense debate, with a number of published articles tackling its feasibility and likely cost (Socolow et al. 2011; Keith, Ha-Duong, and Stolaroff 2005; Lackner 2009; Heidel et al. 2011; Zeman 2007; Zeman 2014; House et al. 2011; Baciocchi, Storti, and Mazzotti 2006; Holmes and Keith 2012; Goeppert et al. 2012; Brandani 2012; Pritchard et al. 2015; Pielke 2009; Lackner et al. 2012; Jones 2011; Ruthven 2014). Although referred to here and elsewhere as an emission reduction strategy, DAC is actually more of a climate engineering strategy, with the ability to affect global atmospheric concentrations of CO_2.

MCC refers to the on-board capture of CO_2 from vehicle exhaust, where concentrations are on the order of 13.5% by volume (Taylor 1993), with periodic offloading of the captured CO_2 or CO_2-laden capture sorbent. In contrast with DAC, MCC has received almost no attention from carbon capture researchers. The majority of mentions of mobile carbon capture in the literature come from DAC studies, where MCC is assumed either infeasible or impractical. This assumption of infeasibility is then used as evidence to support the research and implementation of DAC to manage mobile emissions. For example, a recent review on carbon capture by Boot-Handford et al. (2014) reduced mobile capture to a single uncited sentence in support of DAC:

> *"Air capture could also offer an option for addressing CO_2 emissions from mobile and distributed sources, such as vehicles, fuel use in buildings and geographically isolated industry, where direct capture and integration into a centralised CCS network would be either impractical and/or uneconomical."*

Outside of mentions in the DAC literature, actual studies on MCC are limited. Examples include a small study on a modified internal combustion Rankine engine by Bilger and Wu (2009) and a review of potential consumer support by Sullivan and Sivak (2012). Given that CO_2 concentrations in vehicle exhaust are over 300 times greater than the concentrations in ambient air, it seems unlikely that DAC would represent a significant energy and cost savings over MCC, as has been suggested by the DAC literature. A study into the actual expected costs and design trade-offs of a MCC system is needed in order to ground comparisons between the two systems.

1.6 Scope and Outline of the Dissertation

This dissertation nominally consists of five chapters: one introductory chapters, three results-based chapters and a summary chapter. The overarching goal of the dissertation can be broken down into two main objectives. The first objective, to which chapters 2 and 3 are devoted, is a thorough study of flexible capture materials, using ELMs as a representative class, in order to better assess their suitability for carbon dioxide capture applications. Chapter 2 uses static adsorption isotherm measurements and density functional theory (DFT) to evaluate the threat posed by trace species present in flue gas streams, such as NO_x, SO_x, and water vapor, to the CO_2 capture performance of ELMs and identify design strategies that could improve the CO_2 capture performance of ELM based capture technologies. Chapter 3 evaluates the "real world" impact crystal flexibility and "gate-opening" transitions have on carbon dioxide separation from various gas mixtures by comparing breakthrough experiments performed on ELM-11 with the predictions of the "gate-opening" pressure obtained from the osmotic framework adsorbed solution theory (OFAST).

The second objective of this dissertation, as embodied in chapter 4, is to look into one possible carbon capture future by evaluating the feasibility of mobile carbon capture (MCC) as a follow-on strategy to current and near-future carbon dioxide capture at stationary sources. In this chapter, a combination of techniques from the recycling, life cycle assessment, and direct air capture (DAC) literature are used to map out the potential costs associated with implementing a MCC scheme and identify potential trade-offs in MCC system design. The fifth and final chapter presents a summary of findings and recommends future research paths for further improvement of carbon capture technologies.

CHAPTER 2

Performance of Elastic Layered Metal Organic Frameworks After Water Vapor and Trace Gas Contaminant Exposure: An Experimental and Computational Study

In this chapter, the CO_2 capture performance of elastic layered metal-organic frameworks (ELMs), as a representative class of flexible MOFs, during and after exposure to water vapor and other trace gas contaminants is explored. Two ELM variants, ELM-11 and ELM-12, were cyclically exposed to pure water vapor isotherms and the impact on the CO_2 capacity of the frameworks was observed. ELM-11 was found to lose CO_2 capacity with each cycle of water vapor exposure. In contrast, ELM-12 retained CO_2 capacity through at least 4 exposure cycles. In addition, the binding energies and binding sites of trace gas contaminants on six different ELM analogs were explored using density functional theory. Molecules with strong dipoles, like H_2O, SO_2, and H_2S, show stronger binding energies on ELM frameworks than quadrupolar molecules like CO_2 and N_2. However, the impact of these strongly binding molecules can be reduced through creative choice of framework components. Binding energies were largest for copper based frameworks, while cobalt and nickel based frameworks showed reduced binding energies. Changing the counter ion from the simple tetrafluoroborate (BF_4^-) to the larger and more complex trifluoromethanesulfonate ($CF_3SO_3^-$) expands the number of potential binding sites for adsorbate molecules. While CO_2 directly competes with other adsorbates for binding sites in ELM-11, CO_2 does not directly compete with other adsorbates in ELM-12 due to its unique preference for direct interaction with both fluorine and oxygen atoms in $CF_3SO_3^-$.

2.1 Introduction

Metal-organic frameworks (MOFs), also known as porous coordination polymers (PCPs) (Kitagawa, Kitaura, and Noro 2004), are a relatively novel class of hybrid materials built from metal ions with well-defined coordination geometry and organic bridging ligands. Through careful choice of metal and organic building blocks, MOFs can be conceptually designed and synthesized based on how building blocks come together to form a net, allowing fine tuning of pore size and crystal structure. Over 20,000 different MOFs have been reported and studied within the past decade (Furukawa et al. 2013). The enormous structural and chemical diversity of MOFs has resulted in an enormous growth of research into their potential application for gas storage, ion exchange, molecular separation, and heterogeneous catalysis (D'Alessandro, Smit, and Long 2010). The exceptional tunability of these materials has allowed MOFs to break several records in porous material properties such as highest surface areas, hydrogen (H_2) uptake based on physical adsorption, and CH_4 and CO_2 storage (J.-R. Li et al. 2011). Their large surface areas, adjustable pore sizes, and controllable pore surface properties, make MOFs especially appealing next generation porous adsorbents for CO_2 capture.

Flexible MOFs, also known as soft porous crystals (SPCs) (Horike et al. 2012), are a subset of MOFs that possess both a highly ordered network and structural transformability. In contrast with rigid MOFs, which retain their structure and porosity irrespective of environmental factors, SPCs can undergo structural transformations depending on external stimuli such as temperature, mechanical pressure, or guest adsorption due to their bi-stable or multi-stable natures (Bousquet et al. 2013). This multi-stable nature of SPCs has led to the observation of previously unpredicted gas adsorption phenomena. A subset of SPCs that are representative of the class' exotic adsorption behaviors are the so called elastic layered metal-organic

Table 1. Typical Post-combustion Composition of Traces Gases in the Flue Gas Stream of a Coal-Fired Power Plant (Sumida et al. 2012)

Molecule	Concentration (by volume)
H2O	5-7 %
O2	3-4 %
SO2	800 ppm
SO3	10 ppm
NOx	500 ppm
HCl	100 ppm
CO	20 ppm
hydrocarbons	10 ppm
Hg	1 ppb

frameworks (ELMs) (Kajiro et al. 2010; Kanoh et al. 2009). ELMs are composed of metal vertex ions, connecting ligands, and charge balancing counter ions arranged in two dimensional grid sheets organized in three dimensional stacked structures. These materials show a latent porosity (Noguchi et al. 2005) and adsorption of gas molecules above a specific pressure, termed the "gate pressure", results in expansion of the layer planes and a vertical jump in the adsorption profile which cannot be classified under conventional IUPAC classifications. The exotic adsorption characteristic of ELMs, which are not observed in traditional porous materials or in rigid MOFs, offer ELMs potential advantages for CO_2 capture such as high selectivity for CO_2 combined with low energy requirement for adsorbent regeneration and CO_2 recovery (Kanoh et al. 2009).

However, in order to be suitable for post-combustion carbon capture (PCC), carbon capture materials need to selectively adsorb low concentrations of CO_2 (4-15%) in the presence of unwanted flue gas components. A typical coal combustion flue gas has significant concentrations of water vapor, SO_x, NO_x, and CO (Sumida et al. 2012) (Table 1), which may significantly impact the CO_2 capture performance and stability of MOFs (Yu, Ma, and Balbuena 2012). In addition, because PCC systems often assume regeneration of the adsorbent

and recovery of the captured CO_2, prospective CO_2 capture materials will need to perform consistently through many adsorption/regeneration cycles.

Regeneration of a solid adsorbent is typically accomplished by temperature swing adsorption (TSA), pressure swing adsorption (PSA), vacuum swing adsorption (VSA), or some combination of these processes (Sumida et al. 2012). Due to the availability of low grade waste heat from the power plant as a source of energy for regeneration, TSA is often considered particularly promising for many CCS applications. In order to be considered for use in TSA, ELMs must show consistent CO_2 capture performance even after repeated exposure to unwanted gas components, water vapor and thermal stress.

Many rigid MOFs have relatively good thermal stability. For example, CO_2 adsorption of $Zn_4O(bdc)_3$ (bdc = 1,4-benzenedicarboxylate), termed MOF-5, remains near 3.6 wt% when cycled between 30 and 300°C at atmospheric pressure. It is only above 400°C that MOF-5 undergoes thermal decomposition and is no longer able to adsorb CO_2 (J.-R. Li et al. 2011). However, flexible MOFs, by definition, have crystal structures that are more susceptible to flexing and distortion during exposure to external stimuli or stress. The question for flexible MOFs like ELMs is whether the increased framework flexibility, which is accomplished through incorporation of weaker inter-framework interactions, reduces their thermal stability. In terms of a simple cyclic process, an experiment exploring repetitive adsorption-desorption cycle of CH_4 on ELM-11 at 303 K showed no degradation of the gating transition even after 50 cycles (Kanoh et al. 2009). A thermogravimetric analysis performed by Cheng et al (Cheng et al. 2009) showed that the ELM-11 structure begins to lose bpy and BF_4 molecules at around 500 K. The combination of these two experiments suggests that ELM-11 can be safely cycled up to approximately 170 - 200°C with no expected loss in structure. It is therefore expected

that the ELM class of materials will have a thermal cyclic stability nearly comparable to that of rigid MOFs.

What is of greater concern then is stability of ELM materials when exposed to trace gas components, such as water vapor, SO_x, and NO_x. Several MOFs are not stable when in contact with water (Liu et al. 2012). For example, the MOF $Cu_3(btc)_2$ (btc = 1,3,5-benzene tricarboxylate), termed HKURST-1, was observed to be stable in O_2 at room temperature, but its crystallinity was progressively reduced upon cyclic exposure to water vapor at 30% relative humidity, but leveled out at 75% of its original value after several water adsorption/desorption cycles. The MOF Ni/dobdc was reported to be prone to lose CO_2 capacity after repeated H_2O/CO_2 mixture isotherm measurements. It was also reported that $Zn_2(bdc)_2(dabco)$ and $Ni_2(bdc)_2(dabco)$ (dabco = 1,4-diazabicyclo[2.2.2]octane) are stable after O_2 and 30% relative humidity water vapor sorption at 25°C, but collapsed after 60% relative humidity water vapor sorption at the same temperature. More recently, Kizzie, Wong-Foy, and Matzger (2011) explored the effect of humidity on CO_2 capture in the M/dobdc series (where M = Zn, Ni, Co, or Mg; dobdc = 2,5-dioxidobenzene-1,4-dicarboxylate). They found that although Mg/dobdc had the highest initial CO_2 capacity at the conditions used in the study, exposure to a relative humidity of 70% followed by thermal regeneration resulted in recovery of only 16% of the initial CO_2 capacity. In contrast, 85% of the CO_2 capacity in Co/dobdc could be recovered under the same conditions. It is evident then that water vapor can both damage MOF structures and hinder adsorption of CO_2. Studies of the effect of other flue gas components like SO_x and NO_x on the CO_2 capture performance of MOFs are limited, but a study by Yu, Ma, and Balbuena (2012) found that the presence of SO_2 lowered the CO_2 selectivity of HKUST-1, especially at high pressures due to its strong binding with the HKUST-1 framework.

In the ELM class of materials, Cheng et al. (2009) studied the evolution of the structure of ELM-11 upon a single cycle of dehydration and rehydration under exposure to water vapor. They concluded that the processes was mostly reversible and that the slight differences seen in the adsorption profile were probably due to stacking faults and/or different interaction phases. However, this experiment represents only a single water vapor exposure cycle and the stability of other ELM analogs to water vapor has not been explored in great detail.

Considering that other MOFs show significant performance loss under cyclic exposure to water and that exposure to trace gases like SO_x and NO_x can lower a MOF's selectivity for CO_2, it is important to understand how ELMs will perform under similar conditions. In addition, given that substitution of different structural components can have a significant effect on the CO_2 capacity after water vapor exposure, it is important to explore a number of ELM variants. In order to fill these knowledge gaps and understand the expected CO_2 capture performance of ELMs after water vapor and trace gas contaminant exposure, this work uses a combination of cyclic water vapor exposure experiments and density functional theory calculations performed on a number of ELM variants.

2.2 Methods

2.2.1 Material Preparation and Characterization

Two isostructural ELM variants were experimentally tested in this chapter: $Cu(bpy)_2(BF_4)_2$, termed ELM-11, and $Cu(bpy)_2(OTf)_2$, termed ELM-12, (where bpy = 4,4'-bipyridine and OTf = $CF_3SO_3^-$). See section 2.4.1 for additional guidance on the naming conventions of ELMs used in this chapter. Two methods were used to obtain samples of ELM-11. The first method was the purchase of the un-activated precursor to ELM-11, $[Cu(bpy)(BF_4)_2(H_2O)_2]bpy$, termed

pre-ELM-11, which is sold commercially by Tokyo Chemical Industry Co., Ltd. (CAS Number: 854623-98-6, Product Number: C2409) at >98% purity. The second method was the synthesis of Pre-ELM-11 following procedures previously reported by Tran (2012):

> *"4,4'-bipyridine (0.312 g; 2 mmol) in 2 mL of ethanol was slowly added to an 8-mL aqueous solution of Cu(BF4)2•H2O (0.309 g; 1 mmol) at room temperature… A blue precipitate formed gradually using this procedure. The mixture was stirred for four hours at room temperature, after which the solid was allowed to sit for two days and then filtered off, washed with water and ethanol, and dried in air at room temperature."*

Once the Pre-ELM-11 material is obtained it can be easily converted to ELM-11 by degassing the material under vacuum (<10 μmHg) at 403 K for two hours.

ELM-12 was synthesized using a modified version of the procedures reported by Kondo et al. (2011). 0.2 g of $Cu(OTf)_2$ was dissolved in 10 mL deionized water. 0.2 g of 4,4'-bipyridine (bpy) was dissolved in 10 mL ethanol. To the copper solution, 2 mL methanol was added dropwise close to the surface to slow the diffusion-precipitation process. Then the bpy solution was added dropwise in the same manner. The solution was then sealed from the atmosphere and allowed to sit undisturbed for two weeks. The resulting blue microcrystals were rinsed with ethanol, drained, and allowed to air dry. The powder was then degassed under vacuum (<10 μmHg) at 403 K for two hours.

Characterization of the materials was done collecting X-ray powdered diffraction (XRD) patterns, infrared (IR) spectra, and adsorption isotherms for comparison to previous studies. A Rigaku MiniFlex600 was used to collect X-ray powdered diffractions for both ELM-11 and ELM-12. A PerkinElmer Spectrum BX FT-IR spectrometer was used to collect IR spectra. Adsorption isotherms were measured using a Micromeritics ASAP 2050 extended pressure

volumetric adsorption analyzer. Ultra-high purity (99.99% or higher) N_2, He, and CO_2 gases were used. The analysis temperature in the sample tube was controlled by an external bath.

2.2.2 Water Vapor Cycling Experiments

In order to assess the impact of water vapor on the CO_2 capture performance of ELMs, cyclic exposure experiments were performed. The experimental procedure for cyclically exposing ELM materials to water vapor was carried out as summarized in Figure 14. The ELM material, either ELM-11 or ELM-12, was first activated (i.e., degassed under vacuum (<10 μmHg) at 403 K for at least two hours) and then a CO_2 adsorption isotherm measurement was performed on this freshly activated ELM material to determine baseline CO_2 adsorption capacity. For ELM-11, CO_2 isotherms were performed at 273 K to more than 1 bar, in keeping with study by Cheng et al. (2009). For ELM-12, CO_2 isotherms were performed at 298 K to more than 3 bar. All CO_2 adsorption isotherms were performed in keeping with the description in section 2.2.1. The ELM material was then transferred to a Quantachrome Autosorb-1 where it was regenerated (i.e., degassed again under vacuum (<10 μmHg) at 403 K for at least two hours) before undergoing a pure water vapor adsorption isotherm measurement at 298 K up to a

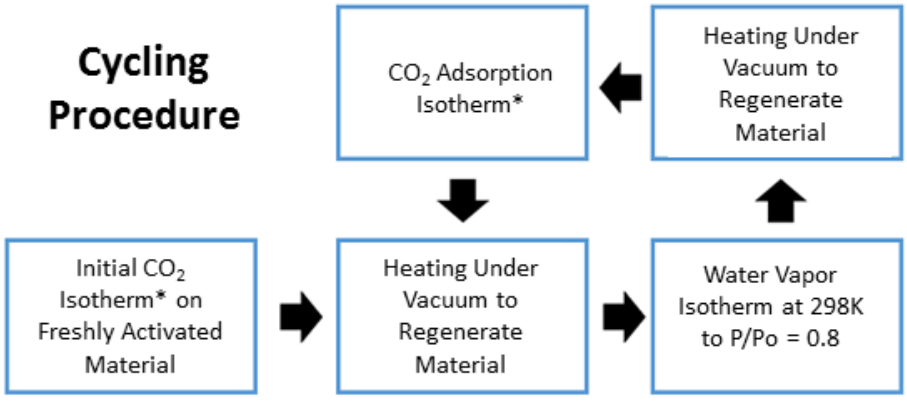

Figure 14. Flow diagram for cycling procedure. *For ELM-11, CO_2 isotherms were performed at 273 K to more than 1 bar, in keeping with study by (Cheng et al. 2009). For ELM-12, CO_2 isotherms were performed at 298 K to more than 3 bar.

relative vapor pressure (P/Po) of 0.8. After water vapor exposure the material was transferred back to the ASAP 2050 where it was again regenerated before undergoing a second CO_2 adsorption isotherm. This experiment was repeated at least 3 times for each ELM material for at least 4 cycles to assure that experimental results were consistent.

2.2.3 Density Functional Theory Calculations

In order to investigate the impact of water and other trace gas species have on the adsorption of CO_2 in ELMs, density functional theory (DFT) calculations were performed. DFT is a quantum mechanical modeling method used to investigate the electronic structure of many-body systems. This method has seen increased use in recent years in the study of gas adsorption onto MOFs. Recent studies have used DFT calculations to investigate the impact of ligands on CO_2 adsorption (Torrisi, Mellot-Draznieks, and Bell 2009; Torrisi, Mellot-Draznieks, and Bell 2010), favorable adsorption sites of various gas molecules on different MOFs (Dangi et al. 2010; Grajciar et al. 2011; Ramsahye et al. 2008), as well as adsorption induced transformations of a flexible MOF (Nijem et al. 2011). In this chapter, DFT is employed to calculate the optimum geometries and binding energies of adsorbate molecules to adsorbent clusters representing 6 ELM variants: ELM-11, ELM-12, ELM-21 [$Co(bpy)_2(BF_4)_2$], ELM-22 [$Co(bpy)_2(OTf)_2$], ELM-31 [$Ni(bpy)_2(BF_4)_2$], and ELM-32 [$Ni(bpy)_2(OTf)_2$]. Other than CO_2, and H_2O, the adsorbate molecules tested include those common in post combustion carbon capture (N_2, NO_2, SO_2, and CO) and natural gas purification (CH_4 and H_2S). The electronic and structure properties of these molecules is summarize in Table 2. The following sections go into more detail about cluster development, choice of functional and basis set, and simulation procedures. All DFT calculations presented in this chapter were done using the Gaussian 09 software package (Gaussian 09 2010).

Table 2. Properties of Molecules Commonly Found in Post-combustion Flue Gas and Raw Natural Gas.

Molecule Grouping	Molecule	Dipole (Debye)	Quadrupole (Debye Å)	Polarizability (Å^3)
Bent/Dipole	H_2O	1.85	*	1.501
	SO_2	1.63	*	3.219
	H_2S	0.97	*	3.6
	NO_2	0.32	*	2.91
Linear/Quadrupole	CO_2	0	-4.28	2.51
	N_2	0	-1.39	1.71
Other	CO	0.11	-2.84	1.95
	CH_4	0	0	2.45

*Cannot be reduced to single component

2.2.3.1 Choice of Basis Set and Functional

The 6-31G(d) basis set was used for all atoms except the transition metals (Cu(II), Co(II) and Ni(II)). For the transition metal atoms, the "LANL2DZ" basis set was chosen. It is one of the most commonly used basis sets for structures involving transition metal elements (Yang, Weaver, and Merz 2009). The B3LYP hybrid functional was chosen for use after comparison with the M06 and M06-2X functionals and with experimental data collected here and reported elsewhere by various authors (Kajiro et al. 2010; D. Li and Kaneko 2001; Kondo et al. 2006; Noguchi et al. 2007; Kondo et al. 2007). See section 2.4.6 for additional details, results, and discussion of these functional comparisons.

2.2.3.2 Model Cluster Development

The ELM-11 unit cluster was constructed from X-ray powder diffraction data as reported by Kondo et al. (2006) and obtained from the Cambridge crystallographic data center. The representative cluster for ELM-11 is made up of a single copper atom and its associated ligands, with the 4,4'-bipyridine (bpy) linkers replaced by more compact pyridine rings to limit

end effects. Atomic positions and bond lengths were optimized using the geometric optimization option with default convergence criteria.

The ELM-12 unit cluster was similarly constructed from X-ray powder diffraction data as reported by Kondo et al. (2009) and obtained from the Cambridge crystallographic data center. Subsequent clusters developed for ELM-21, ELM-22, ELM-31, and ELM-32 replaced the copper atom with the appropriate metal atom and re-optimized the initial geometry. Final DFT optimized geometries for ELM-11 and ELM-12 are shown in Figure 15. Additional optimized geometries for other ELM variants used in this chapter are included in the supplemental information in section 2.4.7.

2.2.3.3 Calculation of Binding Energies

To determine binding energies of adsorbate molecules on the ELM clusters, atomic positions before and during gas molecule adsorption were first optimized using the geometric optimization option in the Gaussian 09 software with default convergence criteria. The coordinates of the ELM cluster and the adsorbing gas molecules were not held fixed during the geometric optimizations. For ELM variants with BF_4 as the counter ion, at least two

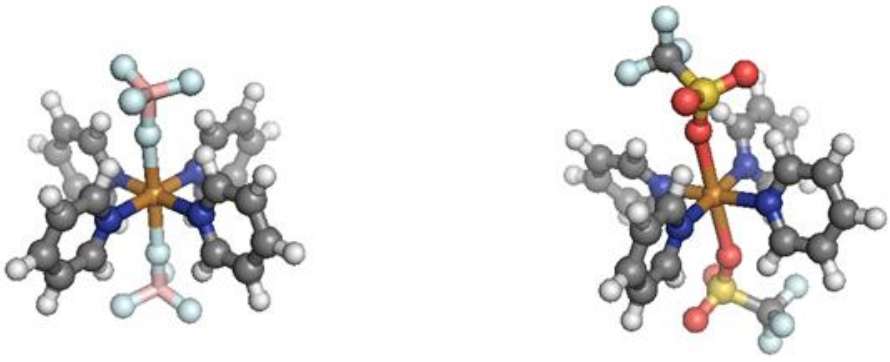

Figure 15. Final DFT optimized geometries for ELM-11 (left) and ELM-12 (right) Color scheme is: copper (copper), fluorine (light blue), boron (pink), nitrogen (dark blue), carbon (grey), oxygen (red), hydrogen (white), Sulfur (yellow).

different starting positions were used for every gas molecule in order to assure that final optimized positions represent global, not local, lowest energy geometries. For ELM variants with OTf as the counter ion, at least three different starting positions for each gas molecule were used.

The total binding energies of adsorbate molecules are calculated from the following equation:

$$Binding\ Energy = E_{gas/cluster} - E_{gas} - E_{cluster} \quad (1)$$

where E_{gas} and $E_{cluster}$ are the total electronic energies of the geometrically optimized gas molecule and the geometrically optimized ELM unit cluster model, respectively; $E_{gas/cluster}$ is the total electronic energy of the geometrically optimized adsorbent/adsorbate system when a gas molecule is adsorbed onto the ELM unit cluster.

2.3 Results and Discussion

2.3.1 Water Vapor Cycling Experiments

Figure 16 shows the results of cyclic water vapor exposure on the CO_2 isotherms of ELM-11 (A-1) and ELM-12 (A-2). Although ELM-11 retains capacity during normal adsorption/regeneration cycles (see section 2.4.4). When exposed to water vapor between measured CO_2 adsorption isotherms, ELM-11 shows decreased capacity and a decay of the gating transition with each water vapor exposure, with complete loss of CO_2 capacity by the 5^{th} cycle. In contrast, ELM-12 shows resiliency in terms of capacity and shape of its CO_2 and water vapor isotherms with minimal deviation in the adsorption branch even after 4 water vapor exposure cycles.

2.3.1.1 The Degradation of ELM-11

The observed degradation of ELM-11 is unexpected based on the report by Cheng et al. (2009) which concluded that the ELM-11 structure could be mostly recovered after water vapor adsorption. However, full comparison of the results requires looking not only at the CO_2 isotherms but also at the water vapor isotherms. In the Cheng et al. study the authors reported a water vapor isotherm where the maximum capacity for water vapor approached 65 mg/g at 303 K. This is significant in that 65 mg/g is equivalent to 1 water molecule per BF_4 counter

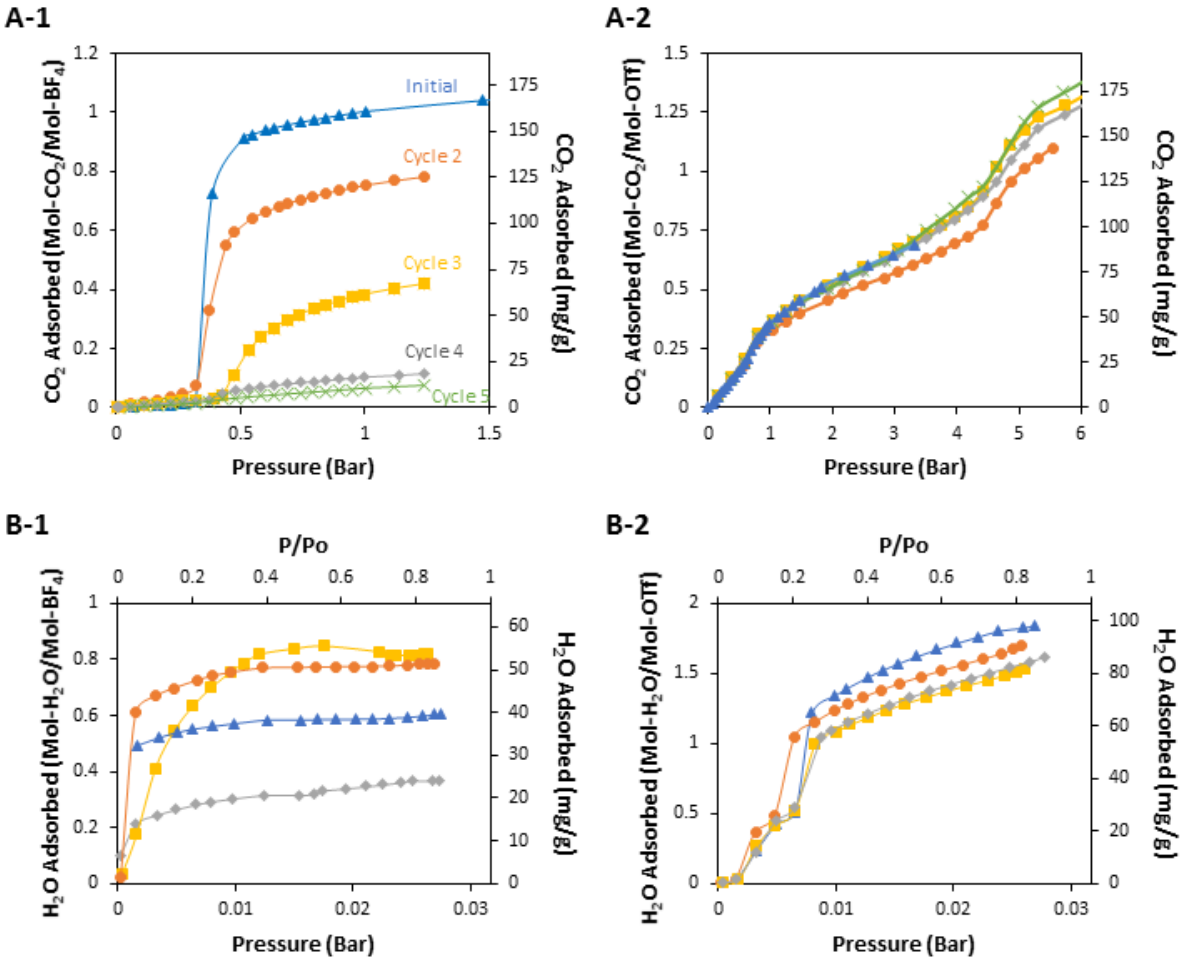

Figure 16. CO_2 isotherms before (initial: blue triangles) and after (2nd cycle: orange circles, 3rd cycle: yellow squares, 4th cycle: grey diamonds, and 5th cycle: green cross) undergoing water vapor isotherms on (A-1) ELM-11 at 273 K and (A-2) ELM-12 at 298 K. Associated water vapor isotherms (inital: blue triangles, 2nd cycle: orange circles, 3rd cycle: yellow squares, 4th cycle: grey diamonds) at 298 K on (B-1) ELM-11 and (B-2) ELM-12. Desorption branches for all isotherms have been removed for clarity.

ion (or 2 water molecules per Copper ion), exactly the same ratio as is present in the pre-ELM-11 structure, suggesting that the recorded "adsorption" is actually incorporation of H_2O into the crystal structure as ELM-11 reverts to pre-ELM-11. In the experiment by Cheng et al., *in situ* XRD studies indicated that the ELM-11 structure returned to pre-ELM-11 during water vapor exposure, which supports this interpretation. Although *in situ* XRD patterns were not collected in the study performed here, the water vapor adsorption isotherm measurement for ELM-11 (shown in Figure 16(B-1)) was initially only 40 mg/g and never approached more than 55 mg/g water vapor adsorbed. This suggests that the ELM-11 structure in this study was only partially hydrated to the pre-ELM-11 structure. This could be due to slight differences in experimental temperature for water vapor isotherm measurement (298 K vs 303 K), more aggressive loading of water on the structure (Cheng et al. had 10 sampling points below P/Po = 0.1 whereas this study had only 2 sampling points below P/Po = 0.1), or differences in particle size of the synthesized ELM-11. The mostly likely scenario is that differences in water vapor adsorption between the two experiments can be attributed to a combination of differences in particle sizes and aggressive loading of water. If ELM-11 is suddenly exposed to a high vapor pressure of water, the water will be incorporated into the surface of the ELM-11 particle, transforming the surface into the hydrated form: pre-ELM-11. Pre-ELM-11 is non porous and a surface layer would prevent further diffusion into the ELM-11 particle, thereby limiting the observed H_2O capacity.

Cheng et al. (2009) suggested that the slight differences seen in the adsorption profile before and after water exposure were probably due to stacking faults and/or different interaction phases. Scanning electron microscope images presented by Cheng et al. showed a change in morphology, with the as-synthesized pre-ELM-11 having a distinctly anisotropic plate-like

particle shape while the rehydrated form after water exposure did not exhibit this kind of highly preferred orientation.

The presence of different crystal phases would cause additional stress and/or faults in the crystal structure. This is because the bpy linkers in the partially hydrated form (Figure 17) have different preferred orientations than the bpy linkers in the anhydrous form (Figure 15). Eventually, given enough exposure cycles, the buildup of faults leads to a breakdown of the crystal structure. The difference between this study and the Cheng et al. study can therefore be attributed simply to an increased number of faults collected between hydration/regeneration cycles, due to more unfavorable hydration conditions. Had Cheng et al. continued their experiment for more cycles, they would have seen eventual loss of CO_2 capacity.

2.3.1.2 The Resilience of ELM-12

Both ELM-11 and ELM-12 are synthesized in water solutions. However, while the use of copper/tetrafluoroborate solution leads to the hydrate pre-ELM-11, which can later be activated to form ELM-11, the use of copper/OTf solution leads directly to ELM-12 with no

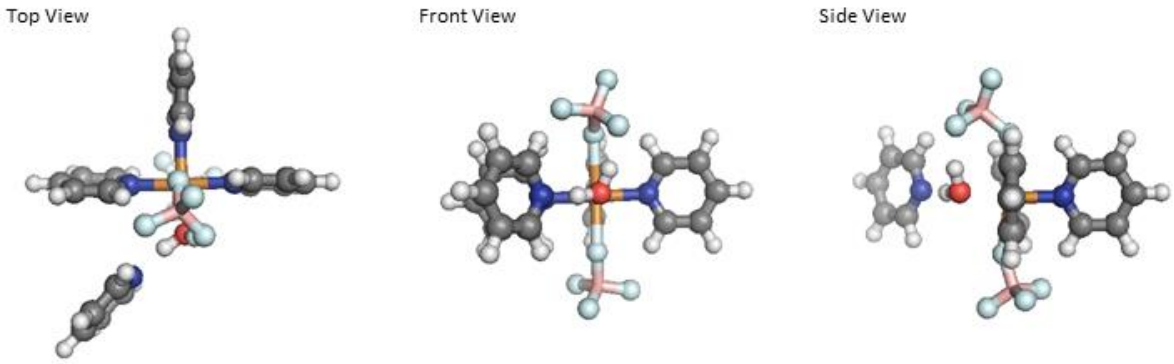

Figure 17. Top view (left), front view (middle), and side view (right) of a DFT optimized geometry for a partially hydrated ELM-11 cluster. Color scheme is: copper (copper), fluorine (light blue), boron (pink), nitrogen (blue), carbon (grey), oxygen (red), hydrogen (white).

intermediate hydrate structure. Activation of the ELM-12 structure is only done to remove solvent molecules that remain in the pore spaces after synthesis. If the degradation of ELM-11 is the result of uncontrolled return to its as-synthesized hydrated structure, then the stability of ELM-12 can be explained by its lack of hydrated form. This lack of a hydrated form is likely the result of the stronger OTf/copper coordination bond. Previous work by Tran (2012) found that the metal-anion force constant between copper and oxygen in ELM-12 was twice as high as the metal-anion force constant between copper and fluorine in ELM-11. This, combined with the fact that OTf is a bulkier counter ion than BF_4, likely prevents water from coordinating with the copper vertex and incorporating itself into the crystal structure.

The resilience of ELM-12 is supported by XRD patterns of ELM-12 taken before and after water vapor exposure which show a return to the original crystal structure (Figure 18). For additional XRD patterns before and after water vapor see section 2.4.2. ELM variants which are anhydrous when synthesized are therefore expected to be more resistant to degradation from water vapor exposure than ELM variants that require activation to remove water molecules from the crystal structure.

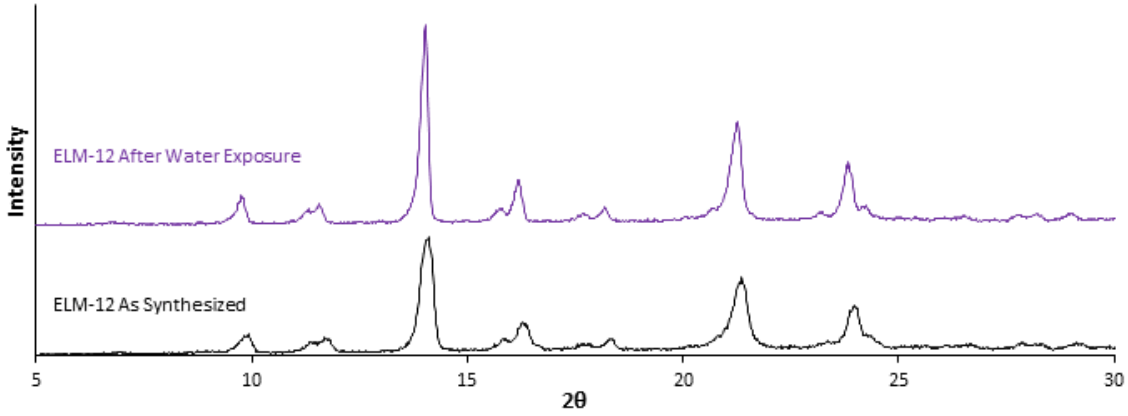

Figure 18. XRD patterns of ELM-12 as synthesized (black) and after water vapor exposure (purple). XRD patterns were collected under normal atmospheric conditions.

2.3.2 Density Functional Theory Calculations

2.3.2.1 Impact of Counter Ion Substitution on Gas Molecule Adsorption

The previous section described how the CO_2 capture performance of ELM-11 degrades after water vapor exposure. The current section looks more generally at competitive adsorption of gas molecules on ELM frameworks when both are present in the gas stream in order to elucidate the impact that counter ion substitution has on preferred binding sites and geometries.

Figure 19 shows the preferred binding sites of CO_2 and H_2O on ELM-11. Both molecules prefer to interact with the fluorine atoms in the BF_4 counter ion, however H_2O has a significantly stronger binding energy for this binding site (-60.4 kJ/mol for H_2O compared with -25.8 kJ/mol for CO_2). This large difference in binding energy is of concern because it means ELM-11 will selectively adsorb the strongly binding H_2O over CO_2 when both are present in the gas stream. In addition, both cause slight extension in the copper-fluorine coordinate bond (from 2.24 Å to 2.27 Å and 2.34 Å for CO_2 and H_2O respectively). This is interesting because the presence of fluorine atoms in the counter ion is expected to play a role in modulating

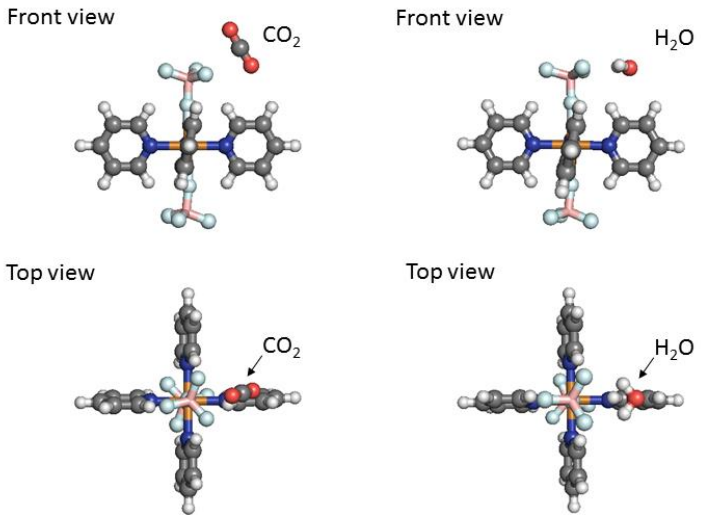

Figure 19. Highest energy binding sites for CO_2 (left) and H_2O (right) on ELM-11. Binding energies are -25.8 kJ/mol and -60.4 kJ/mol for CO_2 and H_2O respectively.

interlayer expansion in ELM frameworks (Kajiro et al. 2010). Although this bond extension is small compared with the total layer expansion visible during CO_2 adsorption by the framework (interlayer spacing increases 2.2Å from 4.6Å to 6.8Å during CO_2 adsorption (Kondo et al. 2006)), the adsorption induced bond distortion within the layer may be important in molecule identification at the surface of ELM-11 where gas molecules are mostly interacting with one or two surface layers. The adsorption induced weakening of the Cu-F bond and the resulting intra-layer distortion may allow for increased interaction between the framework and adsorbate molecules and may initiate the clathrate formation which is typical of the ELM-11 framework. Adsorbate induced intra-layer expansion of the surface layers may be responsible for the slight increase in volume that occurs just below the gate pressure which was observed by Kondo et al. (2006) during the adsorption of CO_2 onto ELM-11.

Another study by Jiang et al. (2009) explored adsorption-desorption induced structural changes of ELM-11 using probe molecules of CH_3OH and CH_3CN. The study indicated that adsorption of molecules with a strong dipole moments like CH_3CN can weaken Cu-F coordinate bonds

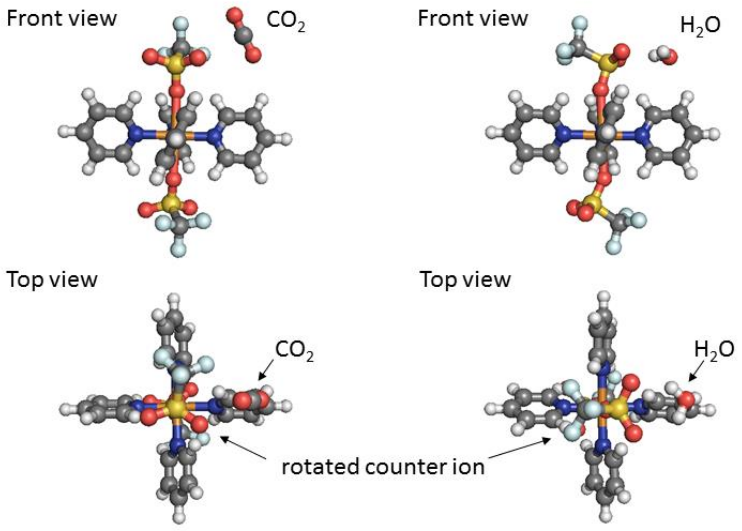

Figure 20. Highest energy binding sites for CO_2 (left) and H_2O (right) on ELM-11. Binding energies are -18.0 kJ/mol and -51.4 kJ/mol for CO_2 and H_2O respectively.

between copper vertices and BF_4 counter ions in the framework and increased framework flexibility. Weakened Cu-F coordinate bonds between the copper vertices and BF_4 counter ions in ELM-11 caused by the strong dipole moment of H_2O is likely why ELM-11 can be returned to pre-ELM-11 when exposed to water vapor.

While ELM-11 has the small and relatively spherical BF_4 as a counter ion, ELM-12 has the larger, linear, and more complex OTf as its counter ion. This larger counter ion offers more potential binding sites for molecule adsorption. Figure 20 shows the preferred binding sites of CO_2 and H_2O on ELM-12. Although H_2O still has a stronger calculated binding energy than CO_2 (-51.4 kJ/mol for H_2O compared with -18.0 kJ/mol for CO_2), this is not as important in ELM-12 because H_2O and CO_2 prefer different binding sites on the OTf group (Table 3). While H_2O prefers direct interaction with both available oxygens of the OTf group, CO_2 prefers a more complex interaction with both an oxygen and a fluorine. This suggests that the two molecules might co-adsorb onto the ELM-12 rather than compete directly for binding sites. This preference for interaction with both the fluorine and the oxygen was unique to the strongly quadrupolar CO_2, suggesting that CO_2 adsorption in ELM-12 may not be strongly impacted by other components present in flue gas streams. Of the molecules tested, only molecules with strong dipoles (H_2S, SO_2, and H_2O) have higher binding energies than CO_2. Weakly quadrupolar, weakly dipolar, and non-polar molecules do not appear to be of concern in terms of competitive adsorption with CO_2 on ELM-12.

Interestingly, as noted in Figure 20, molecules adsorbing onto the ELM-12 framework have the ability to rotate or otherwise affect the orientation of the OTf group. Such orientation differences would be less meaningful for the spherical BF_4 in ELM-11 but may be important

for determining when gating occurs in ELM-12, since, as discussed previously, interlayer interactions are believed to be modulated by the counter ions.

Table 3. Preferred Binding Sites of Gas Molecules Adsorbing onto ELM-12

Adsorbate Molecule**	Binding Site*
N_2	O
CH_4	F,F
CO	O
NO_2	O
CO_2	O,F
H_2S	O
SO_2	O
H_2O	O,O

*Chemical symbol of OTf atoms within 3 Å of adsorbing molecule.
**Listed in order of increasing binding energy on ELM-12 Framework (I.e., N_2 has lowest binding energy and H_2O has highest binding energy)

2.3.2.2 Impact of Metal Substitution on Gas Molecule Adsorption

Also explored in this section is the impact that metal vertex substitution has on gas molecule adsorption. Although changing the metal ion does not impact the preferred binding sites of molecules on the counter ion. It does have an impact on the total binding energies of adsorbed molecules. Copper based frameworks like ELM-11 and ELM-12 tend to have the highest binding energies, while cobalt and nickel based frameworks tend to have reduced binding energies. This trend in binding energies for adsorbates on various ELM variants is summarized in Table 4.

The results of this work parallels previous work by Tran (2012) which found that the higher metal-anion force constants were correlated with higher expected gate pressures of ELM frameworks. Tran predicted that gate pressures in ELMs would follow the trend $Fe^{2+} < Cu^{2+} <$

$Co^{2+} < Ni^{2+} < Mn^{2+}$. These predictions agree with earlier work by Kondo et al. (2009) which showed that changing the metal vertex from copper in ELM-11 or ELM-12 to Nickel in ELM-31 or cobalt in ELM-22 led to lower capacities and a higher gate pressures for CO_2 adsorption.

Table 4. Binding Energies (kJ/mol) of Adsorbates on ELMs with Different Metal Vertices.

Adsorbate Molecule	ELM-11 (Cu_BF_4)	ELM-21 (Co_BF_4)	ELM-31 (Ni_BF_4)	ELM-12 (Cu_OTf)	ELM-22 (Co_OTf)	ELM-32 (Ni_OTf)
N_2	-9.6	-9.8	-8.9	-6.0	-5.9	-5.9
CH_4	-11.1	-11.0	-10.2	-6.2	-6.2	-6.3
CO	-16.6	-16.3	-14.6	-11.4	-11.3	-10.2
NO_2	-17.9	-17.8	-16.7	-13.5	-13.3	-14.3
CO_2	-25.8	-25.2	-23.0	-18.0	-17.8	-17.1
H_2S	-27.5	-26.6	-23.8	-22.9	-21.3	-20.9
SO_2	-39.1	-37.9	-34.4	-37.3	-36.6	-32.0
H_2O	-60.4	-58.3	-53.2	-51.4	-51.0	-43.6

If the choice of metal cation can have such a strong impact on the expected gating pressure, it is not unreasonable to expect an impact on the binding energies of adsorbing molecules. In this case, metals which strongly bind the counter ion are correlated with lower binding energies of adsorbate molecules. This suggests that stiffer frameworks (i.e., frameworks with higher metal-counter ion force constants) would be more resistant to the negative impacts of strongly binding molecules like H_2S, SO_2, and H_2O, although the design trade-off would be increased gate pressures for CO_2 adsorption.

2.4 Supporting Information

2.4.1 Nomenclature of ELMs

A naming convention for elastic layered metal-organic frameworks (ELMs) was suggested by Kajiro et al. (2010). Because of the essential role that metal and counter ion play in determining the structure and properties of ELMs, isostructural ELMs are numbered based on their metal

and counter ion composition. The first number represents the specific metal ion and the second number represents the counter ion as shown in Table 5. All ELM variants used in this work use 4,4'-bipyridine (bpy) as the connecting ligand. For example, the notation ELM-11 designates a metal-organic framework composed of bpy linkers, copper ions (1), and tetrafluoroborate ions (1) (i.e., ELM-11 = $[Cu(bpy)_2(BF_4)_2]$).

Table 5. ELM Variants used in this Chapter (Naming Convention)

	BF_4^- (1)	$CF_3SO_3^-$ (2)
Cu_2^+ (1)	ELM-11	ELM-12
Co_2^+ (2)	ELM-21	ELM-22
Ni_2^+ (3)	ELM-31	ELM-32

2.4.2 Comparisons of XRD Data

X-ray powder diffraction patterns were collected for synthesized pre-ELM-11 and ELM-12. The collected patterns are shown in Figure 21. Patterns for in-lab synthesized pre-ELM-11 compare well with patterns collected for pre-ELM-11 powder purchased from Tokyo Chemical Industry Co., Ltd. All ELM-12 XRD patterns compare well with the XRD pattern reported by Kondo et al. (2007). Patterns for ELM-12 were collected after synthesis, after activation (i.e., degassed under vacuum (<10 μmHg) at 403 K for at least two hours), after storage at atmospheric conditions, and after water vapor exposure. Although there is a slight shift in the XRD peaks after activation, the pattern quickly shifts back to the as-synthesized pattern after a few minutes (~15 minutes) of air exposure.

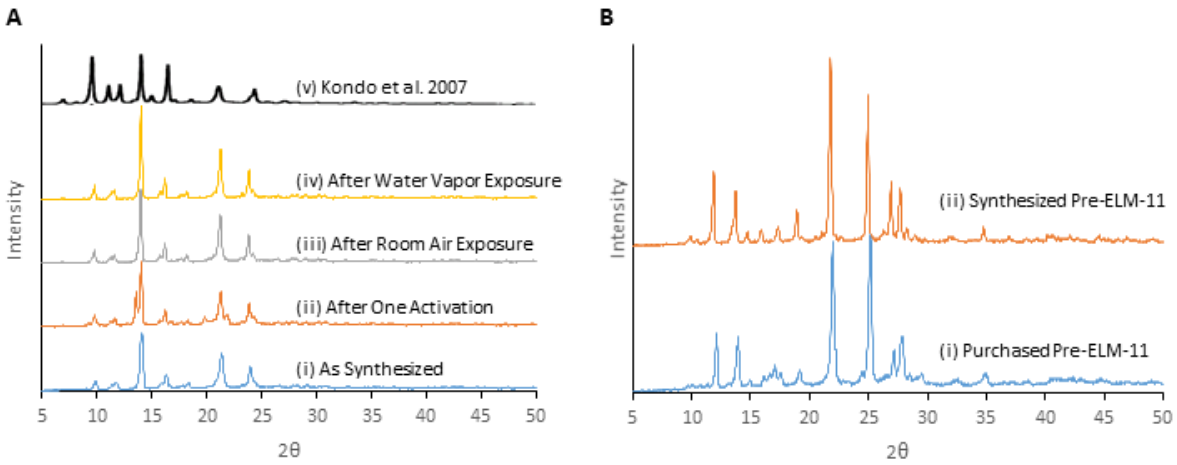

Figure 21. X-ray powder diffraction patterns collected for (A) ELM-12 and (B) pre-ELM-11. For ELM-12, XRD patterns were collected (i) after synthesis, (ii) after one activation, (iii) after storage at normal atmospheric conditions, and (iv) after water vapor exposures for comparison with (v) XRD pattern reported by (Kondo et al. 2007). For pre-ELM-11, XRD patterns were collected to compare (i) pre-ELM-11 powder purchased from Tokyo Chemical Industry Co., Ltd. with (ii) in-lab synthesized pre-ELM-11.

2.4.3 Comparisons of IR Spectra

Figure 22 shows the IR spectra of the as-synthesized pre-ELM-11 and ELM-12. A PerkinElmer Spectrum BX FT-IR spectrometer was used to collect IR spectra.

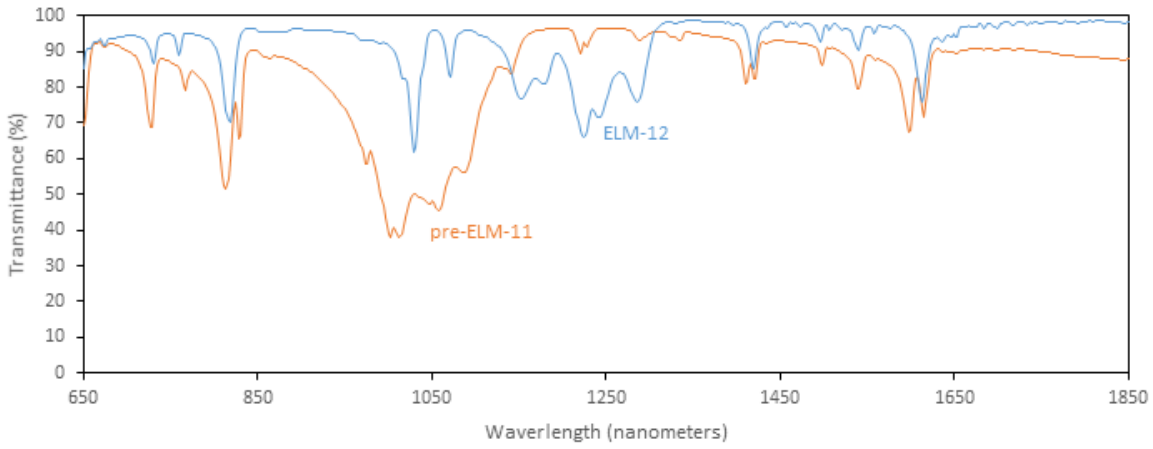

Figure 22. IR spectra of as-synthesized pre-ELM-11 and ELM-12.

2.4.4 Cyclic Adsorption on ELM-11 without the Presence of Water Vapor.

Figure 23 shows the impact of performing 8 CO_2 adsorption isotherms on ELM-11 (with intermediate regeneration). Adsorption isotherms ranged in temperature from 273 K to 348 K. Even with the higher temperature adsorption isotherms, there is minimal change between the initial and final CO_2 isotherms at 273 K. This agrees with the reporting of Kanoh et al. (2009) which showed no degradation of the gating transition in ELM-11 even after 50 cycles of methane adsorption at 303 K.

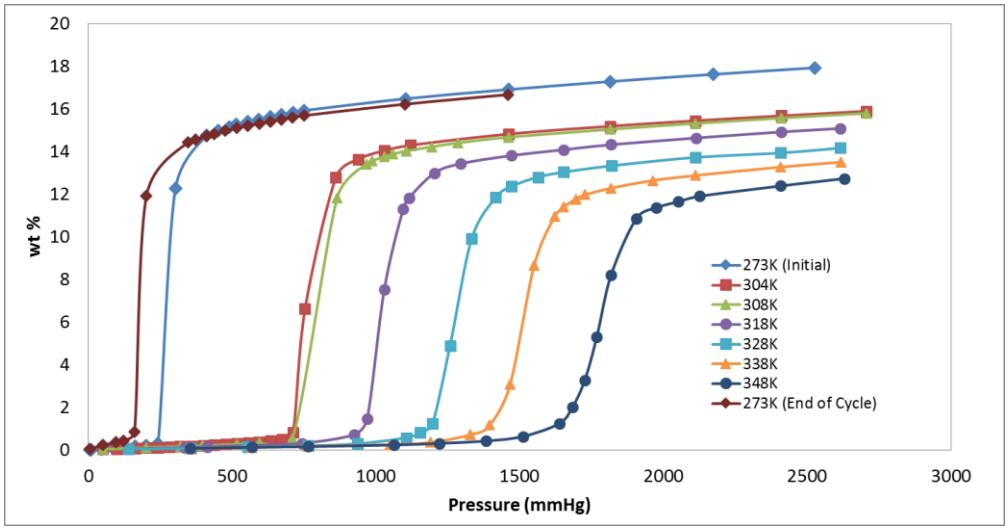

Figure 23. Cycle of CO_2 adsorption isotherms performed on ELM-11. The isotherms were performed in the following order: 273 K → 304 K → 308 K → 318 K → 328 K → 338 K →348 K → 273 K. Desorption branches have been removed for clarity.

2.4.5 Methane Isotherms on ELM-12 and Measured Isosteric Heat of Adsorption

Isosteric heat of adsorption (Q_{st}) can be obtained from experimental isotherms collected at different but closely-spaced temperatures using the Clausius-Clapeyron equation at a constant level of adsorbate loading:

$$Q_{st} = R\left[\frac{T_1 T_2}{T_2 - T_1}\right] \ln\left(\frac{P_2(w)}{P_1(w)}\right) \quad \text{(S1)}$$

where R is the ideal gas constant (8.314 J/mol K), T_i is the absolute temperature of the experimental isotherm *i*, and $P_i(w)$ is the pressure at which the experimental isotherm *i* has an equilibrium loading of *w*. Experimental methane isotherms taken at 273, 288, 298, 308, and 318 K, as well as the results of applying the Clausius-Clapeyron equation to determine the isosteric heat of adsorption are shown in Figure 24. The isosteric heat of adsorption for methane on ELM-12 ranges from 19.3 kJ/mol to 22.7 kJ/mol with an average value around 21 kJ/mol.

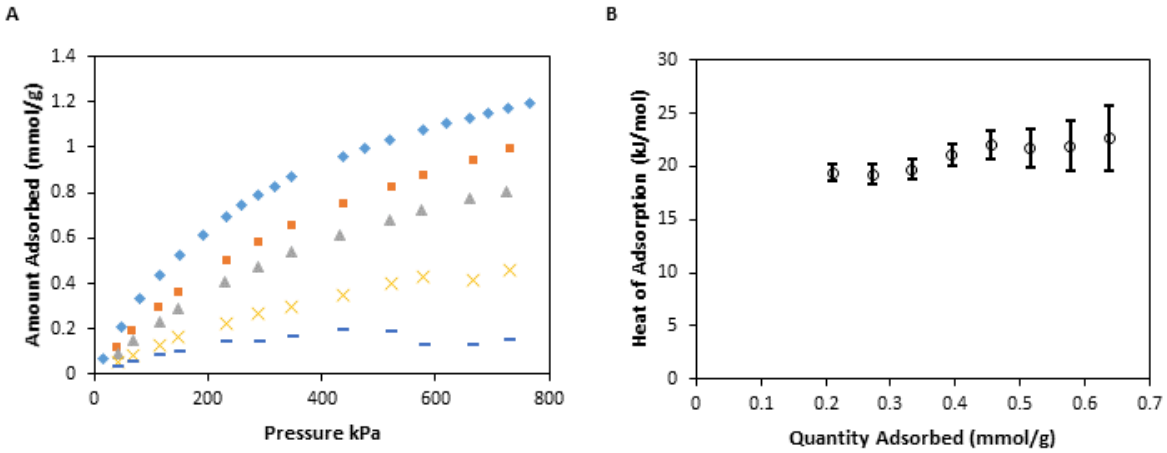

Figure 24. (A) Experimental adsorption isotherms for methane on ELM-12 at 273 K (blue diamonds), 288 K (orange squares), 298 K (grey diamonds), 308 K (yellow cross), and 318 K (blue dash). (B) Isosteric heat of CH_4 adsorption for different methane loadings.

2.4.6 Comparison of B3LYP, M06, and M06-2X Functionals with Experiment

Table 6 compares the results of DFT geometry optimizations using the B3LYP, M06 and M06-2x functionals with experimental values obtained from literature and from experiment. The copper-fluorine (Cu-F) and copper-nitrogen (Cu-N) bond lengths are used for geometry comparisons in ELM-11 while the copper-oxygen (Cu-O) and copper-nitrogen (Cu-N) bond lengths are used for comparison in ELM-12. Binding energies for N_2, CO_2, and CH_4 on both the ELM-11 and ELM-12 structures are compared with reported experimental heats of adsorption to determine how well binding dynamics are captured.

Table 6. Comparison of Functional Performance with Experiment Bond Lengths and Binding Energies

Framework	Parameter [Unit]	DFT Calculated Value			Experimental Value (Reference)
		B3LYP	M06	M062X	
ELM-11	Cu-F bond length [Å]	2.21	2.23	2.17	2.24 (Kondo et al. 2006)
	Cu-N bond Length [Å]	2.1	2.06	2.08	1.8-2.1 (Kondo et al. 2006)
	N2 Binding Energy [kJ/mol]	-9.6	-16.7	-19.0	7.8-9* (D. Li and Kaneko 2001)
	CO2 Binding Energy [kJ/mol]	-25.8	-31.0	-36.0	26* (Kajiro et al. 2010)
	CH4 Binding Energy [kJ/mol]	-11.1	-19.9	-21.0	11* (Noguchi et al. 2007)
ELM-12	Cu-O Bond Length [Å]	2.38	2.28	2.22	2.37, 2.39 (Kondo et al. 2007)
	Cu-N Bond Length [Å]	2.1	2.06	2.09	2.01-2.04 (Kondo et al. 2007)
	N2 Binding Energy [kJ/mol]	-6.0	-10.8	**	12.2[9.9]* (Kondo et al. 2007)
	CO2 Binding Energy [kJ/mol]	-18.0	-28.8	**	26[21]* (Tran 2012)
	CH4 Binding Energy [kJ/mol]	-6.2	-16.8	**	21*†

* Reported as Isosteric Heats of Adsorption. Although equivalent measurements of binding strength, by convention Isosteric Heats of Adsorption are reported as positive values, while Binding Energies are reported as negative values. Values in brackets represent Isosteric Heat of Adsorption measured after the adsorption step in the ELM-12 isotherm.

** Not Calculated

† Experimentally determined in this dissertation. See section 2.4.5 for details.

M06 and M06-2X functionals compare relatively well experimental bond lengths but compare poorly with experimental heats of adsorption in ELM-11. In contrast, DFT results using the B3LYP functional shows good agreement with experimentally determined bond lengths in the framework geometry and binding energies of gas molecules in ELM-11. All functionals compare poorly with experimental heats of adsorption in ELM-12. This is attributed to the effects of simplifying the crystal structure to a single cluster.

Both clusters are simplifications of overall crystal structure, but the difference in results between the two structures suggests that gas adsorption onto the ELM-11 framework can be adequately modeled as the interaction between a single gas molecule, a BF_4 group, and the immediate surroundings of that BF_4 group. Lateral interactions between gas molecules and long range interactions do not appear to play an important role in the adsorption characteristics of ELM-11. Interestingly, maximum adsorption of CO_2 onto the ELM-11 framework after the

gating transition at 273 K is ~150 mg/g which is approximately equal to 1.9 CO_2 molecules per Cu atom or 0.95 CO_2 molecules per BF_4 group. This suggests that each CO_2 is paired with its own BF_4 adsorption site in the expanded ELM-11 structure.

In contrast, the poor results for heats of adsorption in ELM-12 suggest that gas adsorption onto the ELM-12 framework cannot be adequately modeled as the interaction between a single gas molecule, an OTf group, and the immediate surroundings of that OTf group. Lateral interactions between gas molecules and long range interactions appear to play an important role in the adsorption characteristics of ELM-12. Interestingly, initial adsorption of CO_2 onto the ELM-12 framework before the gating transition at 298 K is ~75 mg/g which is approximately equal to 1.2 CO_2 molecules per Cu atom or 0.6 CO_2 molecules per OTf group. This suggests that each CO_2 is shared between OTf counter ions in the collapsed ELM-12 structure.

2.4.7 DFT Optimized Geometries for ELM-21, ELM-31, ELM-22, and ELM-32

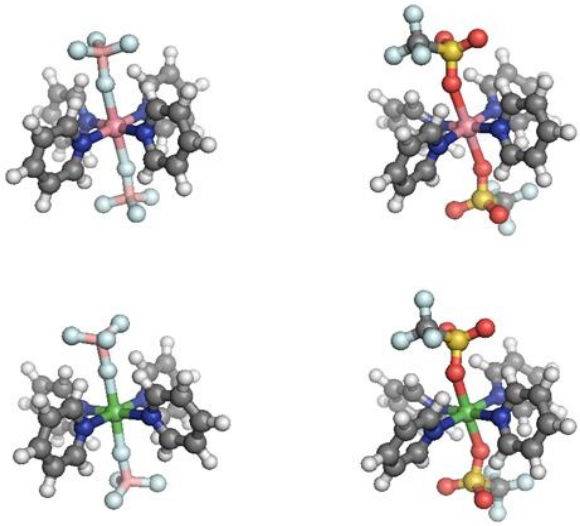

Figure 25. Final DFT optimized geometries for ELM-21 (top-left), ELM-22 (top-right), ELM-31 (bottom-left), and ELM-32 (bottom-right). Color scheme is: cobalt (dark pink), nickel (green), fluorine (light blue), boron (pale pink), nitrogen (dark blue), carbon (grey), oxygen (red), hydrogen (white), sulfur (yellow).

CHAPTER 3

Predicting the Breakthrough Performance of "Gating" Frameworks: Study of ELM-11 using the Osmotic Framework Adsorbed Solution Theory

In this chapter, the breakthrough performance of the elastic layered metal-organic framework $Cu(bpy)_2(BF_4)_2$ (bpy = 4,4'-bipyridine), termed ELM-11, as a representative example of "gating" frameworks, is explored. ELM-11 shows a "stepped" breakthrough curve not seen in rigid adsorbents. The step level observed during breakthrough experiments is a function of temperature, pressure, and mixture composition. The osmotic framework adsorbed solution theory (OFAST) method, which has previously been shown to correctly predict the gating transition in flexible frameworks, is used to predict the expected breakthrough step level in ELM-11. Three types of OFAST models are developed and compared with experimental breakthrough curves. Based on these comparisons, the OFAST method can be used to predict the expected step level from single component isotherms, although the predictions are conservative. Using ideal adsorbed solution theory (IAST) to include additional gas isotherms in OFAST model fits does not result in improved model accuracy unless the estimate for the free energy difference between the open and closed structures (ΔF^{host}) is also modified. The step level observed when CO_2 is mixed with gas species with small kinetic diameters like helium show greater deviation from model predictions than observations where CO_2 is mixed with gas species with large kinetic diameters like methane. This unexpected phenomenon is termed the "door-stop" effect.

3.1 Introduction

Metal-organic frameworks (MOFs), also known as porous coordination polymers (PCPs) (Kitagawa, Kitaura, and Noro 2004), are a relatively novel class of hybrid materials built from metal ions with well-defined coordination geometry and organic bridging ligands. Through careful choice of metal and organic building blocks, MOFs can be conceptually designed and synthesized based on how building blocks come together to form a net, allowing fine tuning of pore size and crystal structure. Over 20,000 different MOFs have been reported and studied within the past decade (Furukawa et al. 2013). The enormous structural and chemical diversity of MOFs has resulted in an enormous growth of research into their potential application for gas storage, ion exchange, molecular separation, and heterogeneous catalysis (D'Alessandro, Smit, and Long 2010). The exceptional tunability of these materials has allowed MOFs to break several records in porous material properties such as highest surface areas, hydrogen (H_2) uptake based on physical adsorption, and CH_4 and CO_2 storage (J.-R. Li et al. 2011). Their large surface areas, adjustable pore sizes, and controllable pore surface properties, make MOFs especially appealing next generation porous adsorbents for CO_2 capture.

Flexible MOFs, also known as soft porous crystals (SPCs) (Horike et al. 2012), are a subset of MOFs that possess both a highly ordered network and structural transformability. In contrast with rigid MOFs, which retain their structure and porosity irrespective of environmental factors, SPCs can undergo structural transformations depending on external stimuli such as temperature, mechanical pressure, or guest adsorption due to their bi-stable or multi-stable natures (Bousquet et al. 2013). This multi-stable nature of SPCs has led to the observation of previously unpredicted gas adsorption phenomena. A subset of SPCs that are representative of the class' exotic adsorption behaviors are the so called elastic layered metal-organic

frameworks (ELMs) (Kajiro et al. 2010; Kanoh et al. 2009). ELMs are two dimensional grid sheets composed of metal vertex ions, connecting ligands, and charge balancing counter ions arranged in three dimensional stacked structures. These materials show a latent porosity (Noguchi et al. 2005) and adsorption of gas molecules above a specific pressure, termed the "gate pressure", results in expansion of the layer planes and a vertical jump in the adsorption profile which cannot be classified under conventional IUPAC classifications. The exotic adsorption characteristic of ELMs, which are not observed in traditional porous materials or in rigid MOFs, offer ELMs potential advantages for CO_2 capture such as high selectivity for CO_2 combined with low energy requirement for adsorbent regeneration and CO_2 recovery (Kanoh et al. 2009).

However, in order to be suitable for post-combustion carbon capture (PCC), carbon capture materials need to show suitable CO_2 capture performance under working conditions. Short of operating a full temperature swing adsorption, pressure swing adsorption, or vacuum swing

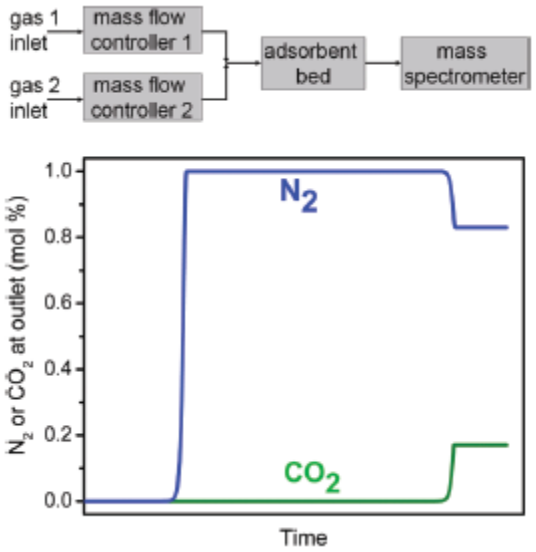

Figure 26. (top) A schematic of the typical configuration of an experimental breakthrough setup and (bottom) an example of an idealized breakthrough curve for a mixed gas consisting of 20% CO_2 and 80% N_2. Taken from (Sumida et al. 2012).

adsorption process, it is impossible to perfectly predict how well a material will capture CO_2 under working conditions. However, it is possible to evaluate the CO_2 capture performance of adsorbent materials in flow through systems by performing breakthrough experiments. In these experiments, a gas mixture is typically flowed through a bed of the adsorbent and the composition of the outgoing gas stream is monitored, usually by gas chromatography or mass spectrometry (Sumida et al. 2012). A simplified schematic of this process is shown in Figure 26.

Very few breakthrough experiments using flexible frameworks have been reported in the literature. Examples include: separation of CO_2/CH_4 in MIL-53(Cr) (Hamon et al. 2009), MIL-53(Al) (Finsy, Ma, et al. 2009), $[Zn(5NO_2\text{-ip})(bpy)]_n$ ($5NO_2$-ip = 5-nitroisophthalate), termed CID-5 (Horike et al. 2012), and $[Zn(5MeO\text{-ip})(bpy)]_n$ (5MeO-ip = 5-methoxyisophthalate), termed CID-6 (Horike et al. 2012); separation of ethane/ethene on $Zn(PhIM)_2\cdot(H_2O)_3$, termed ZIF-7, (Gücüyener et al. 2010); and separation of xylene isomers on MIL-53(Al) (Finsy,

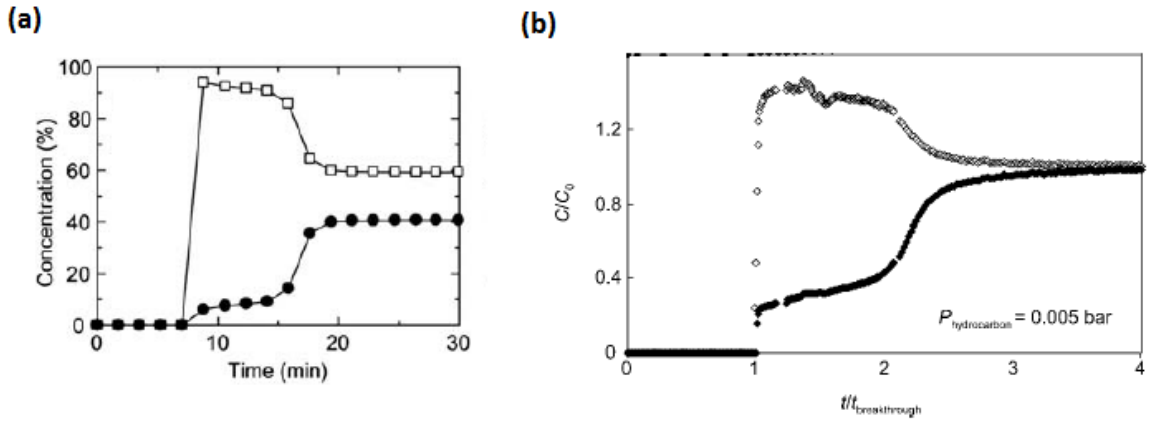

Figure 27. (a) Breakthrough Curves of 60:40 CH_4/CO_2 mixture (by volume) for CID-5 measured at 273 K. The total pressure was 0.80 MPa and the space velocity was 6 min^{-1}. The open square is CH4 and the closed circle is CO_2. Modified from (Horike et al. 2012). (b) Breakthrough curves for the separation of ethylbenzene mixture at partial hydrocarbon vapor pressure of 0.005 bar and a temperature of 110°C. The open diamond is ethylbenzene and the closed diamond is *o*-xylene. Modified from (Finsy, Kirschhock, et al. 2009).

Kirschhock, et al. 2009). Even within this limited number of studies, novel and previously unpredicted breakthrough behaviors can be found. For example, the breakthrough of CO_2 on MIL-53(Cr) shows a distinct change in slope which the authors concluded was most likely related to the breathing of the structure. An even more peculiar "stepped" breakthrough is observed in the separation of xylene isomers with MIL-53(Al) and the separation of CH_4/CO_2 in CID-5. These peculiar "stepped" breakthrough curves are shown in Figure 27. Horike et al. (2012) postulated that the stepped breakthrough could be plausibly attributed to the following mechanism:

> *"... as the CH_4/CO_2 gas mixture reaches the powder of CID-5 at the first point of adsorption, it starts to selectively adsorb CO_2 with a gate-opening phenomenon. Then, the relative pressure of CO_2 in the column of CID-5 decreases quickly, with the result that the relative pressure is now below the gate-opening pressure. The gas mixture of CH_4/CO_2 in which the relative pressure of CO_2 detected at the outlet is below the gate-opening pressure caused the detection of ca. 10% of CO_2 before the breakpoint was reached."*

Finsy, Kirschock, et al. (2009) postulated that the unconventional breakthrough profile was most likely rationalized in terms of a transition from non-selective adsorption in the single-file adsorption mode in the closed form of the pores to selective adsorption in the double-file adsorption mode in the open form of the pores.

If the unusual breakthrough step is a result of the transition between the open and closed structures, then it stands to reason that methods that predict the "gating" or "breathing" transitions in flexible frameworks can also be used to predict the step level in the breakthrough profile. The appropriate thermodynamic method to describe the adsorption of fluids in flexible frameworks is the osmotic framework adsorbed solution theory (OFAST) method proposed by Coudert and coworkers (Ortiz et al. 2012; Boutin et al. 2010; Coudert et al. 2008; Triguero et al. 2011; Bousquet et al. 2013; Coudert et al. 2009; Neimark et al. 2010; Coudert et al. 2011;

Coudert 2010). The OFAST method has been successfully used to study the "breathing" effect and the "gate opening" effect in flexible frameworks. Tanaka et al. (2015) recently used a combination of grand-canonical ensemble Monte Carlo (GCMC) simulations and OFAST to successfully predict the gate transition in ELM-11. In order to better understand the novel and previously unpredicted breakthrough behaviors of flexible frameworks and evaluate their suitability for gas separation applications like carbon capture, this work seeks to collect additional examples of the stepped breakthrough of CO_2 for a representative flexible framework, ELM-11, and predict the breakthrough step level by applying the OFAST method to mixed gas adsorption in ELM-11.

3.2 Methods

3.2.1 Material Preparation and Characterization

To obtain $Cu(bpy)_2(BF_4)_2$ (bpy = 4,4'-bipyridine), termed ELM-11, the un-activated precursor to ELM-11, $[Cu(bpy)(BF_4)_2(H_2O)_2]bpy$, termed pre-ELM-11, was purchased from the Tokyo Chemical Industry Co., Ltd. (CAS Number: 854623-98-6, Product Number: C2409) at >98% purity. Pre-ELM-11 can be easily converted to ELM-11 by degassing the material under vacuum (<10 μmHg) at 403 K for two hours.

Characterization of the materials was done collecting X-ray powdered diffraction (XRD) patterns, infrared (IR) spectra, and adsorption isotherms for comparison to previous studies. See Chapter 2 for additional details.

3.2.2 CO_2 Adsorption Isotherms

Experimental CO_2 adsorption isotherms were measured at 258, 273, 304, 308, 318, 328, 338, and 348 Kelvin using a Micromeritics ASAP 2050 extended pressure volumetric adsorption

analyzer. The analysis temperature in the sample tube was controlled by an external recirculating bath. The measured CO_2 adsorption isotherms used for model fitting are show in section 3.4.2.

3.2.3 He, N_2, and CH_4 Isotherms

Isotherms for He, N_2, and CH_4 on the expanded ELM-11 structure were generated using grand-canonical Monte Carlo (GCMC) simulations performed in the MCCCS Towhee software package (Martin 2013). The rigid expanded ELM-11 structure used for the GCMC simulations was the expanded structure reported by Kondo et al. (2006) with an additional 5% expansion of the interlayer distance for better agreement with methane isotherms reported by Kanoh et al. (2009). See section 3.4.5 for comparison of simulated and experimental methane isotherms. The simulation cell used triclinic periodic boundary conditions with constant system temperature, volume, and adsorbent/adsorbate chemical potentials. Simulation moves for all adsorbate molecules included translation, insertion, and deletion. Simulations for the linear N_2 also included molecule rotation. Each non-orthogonal simulation cell contained ten 4x8 layers, corresponding to a total of 320 Cu atoms. Figure 28 shows the top view of two 4x8 layers of

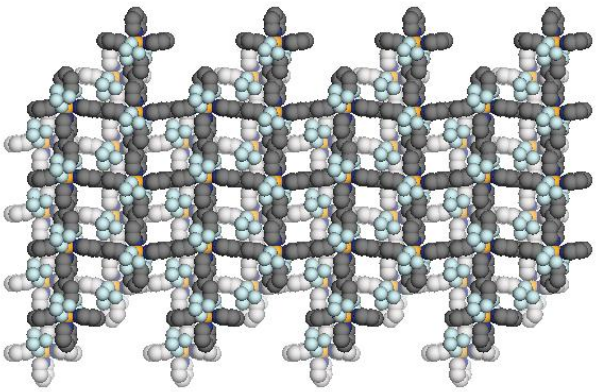

Figure 28. Top view of two 4x8 layers of ELM-11 $[Cu(BF_4)_2(bpy)_2]$ used in simulation cell. Bipyridine linkers are shown in black (top layer) and grey (bottom layer), copper is shown in orange, and tetrafluoroborate is shown in light blue.

the expanded ELM-11 structure used in the simulation. Simulations were run for 10 million moves with the first 2.5 million removed from the analysis as pre-equilibration.

The three-site TraPPE-EH force field (Potoff and Siepmann 2001) was used for N_2 and the single site TraPPE-UA force field (Martin and Siepmann 1998) was used for He and CH_4. The DREIDING force field (Mayo, Olafson, and Goddard 1990) was used for the ELM-11 structure. The parameters for Fe^{2+} were used for Cu^{2+} in the ELM-11 model, because the DREIDING force field employed in towhee does not include an entry for Cu^{2+} and that information is not available in molecular simulation force fields. DREIDING does, however, include Fe^{2+} and Zn^{2+}, which bracket Cu on the periodic table, and uses the same Lennard-Jones parameters for both F^{e2}+ and Zn^{2+}. The charge assignments for atoms in the ELM-11 structure was determined using Density Functional Theory calculations on the ELM-11 cluster described in Chapter 2. After geometric optimization of the unit cluster, atomic partial charges on atoms were derived from calculated mulliken charges. To remove ambiguity about the simulation system, a sample MCCCS Towhee input file has been provided in section 3.4.6.

3.2.4 Application of Osmotic Framework Adsorbed Solution Theory

To predict the step level in the breakthrough profile, the osmotic framework adsorbed solution theory (OFAST) method was used. The governing equation for the OFAST method is the osmotic potential difference between two phases equation developed by Coudert (2010):

$$\Delta\Omega^{os}(T,P,y) = \Delta F^{host}(T) + P\Delta V - RT\int_0^P \frac{\Delta N_{tot}(T,P,y)}{p}\,dp \qquad (1)$$

where $\Delta\Omega^{os}$ is the difference in osmotic potential between the collapsed and open structure, ΔF^{host} is the free energy difference between the collapsed and open structure, P is the total pressure, ΔV is the change in unit cell volume between the collapsed and open structure. R is

the universal gas constant, T is the temperature and ΔN_{tot} is the difference in total quantity of fluid adsorbed inside the pores of the material between the collapsed and open structure.

To apply OFAST to the ELM-11 system, a simplification of equation 1 was used. Under the assumption that molecule adsorption follows a Langmuir isotherm the integral in equation 1 can be solved analytically to give equation 2:

$$\Delta\Omega^{os} = \Delta F^{host}(T) + P\Delta V - RT\left[N_{max}^{(2)} \ln\left(1 + \frac{K_2 P}{N_{max}^{(2)}}\right) - N_{max}^{(1)} \ln\left(1 + \frac{K_1 P}{N_{max}^{(1)}}\right)\right] \quad (2)$$

where $N_{max}^{(2)}$ and $N_{max}^{(1)}$ are the maximum adsorbed quantity (i.e., the number of adsorbed molecules at the plateau of the isotherm) on the open and collapsed structures respectively. While K_2 and K_1 are the Henry constants for adsorption on the open and collapsed structures respectively. By assuming that the change in osmotic potential due to volume change of the unit structure is negligible, and by assuming that the number of adsorbed molecules on the collapsed structure is also negligible, equation 2 further simplifies to:

$$\Delta\Omega^{os} = \Delta F^{host}(T) - RT\left[N_{max}^{(2)} \ln\left(1 + \frac{K_2 P}{N_{max}^{(2)}}\right)\right] \quad (3)$$

At the gate pressure, the osmotic potential difference between the two structures ($\Delta\Omega^{os}$) is zero and the free energy difference between the collapsed and open structure (ΔF^{host}) can be reduced to a three parameter model:

$$\Delta F^{host}(T) = RT\left[N_{max}^{(2)} \ln\left(1 + \frac{K_2 P_{gate}}{N_{max}^{(2)}}\right)\right] \quad (4)$$

where ΔF^{host} as a function of temperature is dependent on the estimate of $N_{max}^{(2)}$, K_2 and P_{gate}, Estimates of $N_{max}^{(2)}$, K_2 and P_{gate} can be obtained in a number of ways, which leads to variations

in the expected value of ΔF^{host}. In the case of single component experimental isotherms, designated Model 1, P_{gate} can be determined directly from the isotherm while $N_{max}^{(2)}$ and K_2 can be obtained from a Langmuir fit of the expanded section of the adsorption or desorption branches (see sections 3.4.1 and 3.4.2 for Langmuir fits of pure gas component isotherms). $N_{max}^{(2)}$ and K_2 can also be estimated using mixed gas adsorption modeling techniques like the ideal adsorbed solution theory (IAST) (Myers and Prausnitz 1965), designated Model 2. IAST is a classic approximation method used to predict the expected co-adsorption of adsorbates on an adsorbent material using pure component isotherms of the gas mixture components taken at the same temperature (Sumida et al. 2012). For additional details on how IAST is implemented in conjunction with OFAST the interested reader is encouraged to see the original work by Coudert (Coudert 2010). If one assumes that the step level in the breakthrough curves are the result of the gating transition, P_{gate} can also be estimated using the observed step level in the breakthrough experiments, designated Model 3. All three fitting approaches were used in this chapter in order to investigate the impact of the fitting process on the success of a given OFAST model. See Table 7 in section 3.4.1 for a summary of model types.

3.2.5 Column Experiments

In order to perform column experiments, a gas flow apparatus was setup as shown in Figure 29. Samples of ELM-11 (~0.3 grams per experiment) were loaded into an adsorption column and activated *in situ*. The initial *in situ* inactivation was performed by flowing pure helium gas at temperatures exceeding 403 K through the adsorbent bed. Once the initial activation was completed, post-experiment regeneration was accomplished through flow of non-adsorbing gases (He, CH_4, and N_2) at room temperature through the adsorbent bed. During experimental measurements, the adsorption column was immersed into a temperature control bath, with

temperatures ranging from 258 to 317 K. Flow rates of CO_2, CH_4, N_2, and He were controlled using needle valves and the overall flow speed was tracked using a rotameter. Gas pressure for the experiment was held at slightly above atmospheric pressure (~108 kPa) to prevent infiltration of room air into the experimental system. The flow speed of gas through the column was between 0.5 and 2 ml/min.

Gas outflow from the column was sampled with a mass spectrometer. Tracking of ions with molecular weights of 44 and 28 were used to determine CO_2 breakthrough/release curves. Ions with molecular weights 4, 13, 14, and 15 were used to corroborate/supplement the determined CO_2 breakthrough/release curves when appropriate. Ion 18 was used to determine if any water vapor from the temperature control bath or room air had infiltrated the column.

There are two types of column experiments that can be performed on flexible frameworks. The first type is termed a "breakthrough" curve in this dissertation. These experiments were performed by flowing pure CO_2 or CO_2/CH_4, CO_2/N_2, CO_2/He binary gas mixtures over an activated ELM-11 bed initially in equilibrium with a pure helium atmosphere. The term

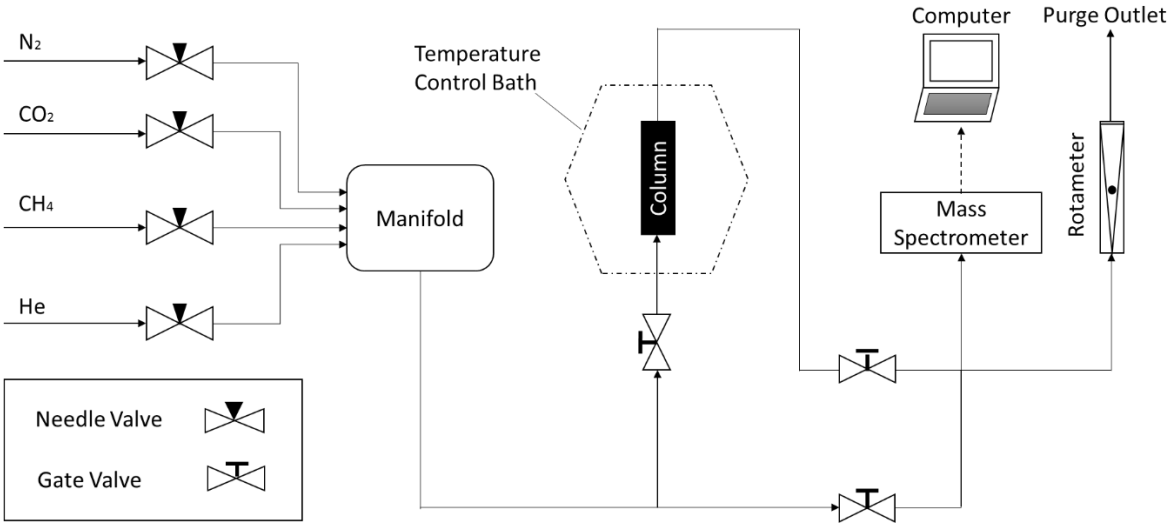

Figure 29. Schematic of laboratory experimental setup for breakthrough experiments.

breakthrough curve is used because the gas flow sampled by the mass spectrometer is initially devoid of CO_2 until the pure CO_2 or binary gas mixture containing CO_2 can "breakthrough" the ELM-11 adsorbent bed. These experiments are designated here as **X→He** (e.g., **CO_2→He** symbolizes an experiment where helium pre-loaded into the column was displaced by a flow of pure CO_2). These experiments should follow the gate opening of the framework or the adsorption branch of the isotherm.

The second type of column experiment is the reverse of the breakthrough curve and is termed a "release" curve in this dissertation. Although theoretically equivalent to breakthrough curves, release curves are, in practice, easier to measure for reasons that will be elaborated upon in the results and discussion section. As such, the majority of column experiment data presented in this dissertation will be release curves. In these experiments, the adsorbent bed is first brought into equilibrium with a pure flow of CO_2 in order to preload the ELM-11 with adsorbed CO_2 molecules. At temperatures where the column pressure was below the gate opening pressure (i.e., >300 K), the ELM-11 material was initially equilibrated with CO_2 at 273 K before being brought up to the temperature of the experiment. Once the CO_2 flow has stabilized, the gas feed is switched from pure CO_2 to either pure CH_4, pure N_2, or pure He depending on the experiment. The results from these experiments are termed "release curves" because the gas flow sampled by the mass spectrometer is initially 100% CO_2, but approaches 0% CO_2 as CO_2 desorbs (is released) from the ELM-11 adsorbent bed and the column becomes filled with CH_4, N_2, or He. These experiments are designated as **X → CO_2** (e.g., **He → CO_2** symbolizes an experiment where CO_2 gas that had been pre-loaded into the column was displaced by a flow of pure helium). These experiments should follow the gate closing of the framework or the desorption branch of the isotherm.

3.3 Results and Discussion

3.3.1 The Stepped Breakthrough Curves of ELM-11

Figure 30 shows the breakthrough of CO_2 on ELM-11 for a 60/40 CH_4/CO_2 gas mixture at 258 K and a pure CO_2 stream at 273 K. Immediately apparent in both graphs is a step in the breakthrough curve that is not seen in rigid frameworks, although it has been observed in other flexible frameworks as discussed in the introduction. Horike et al. (2012) postulated that the stepped breakthrough could be plausibly attributed to the gating transition. If we examine the graphs closely we find that the steps occur at ~20% CO_2 at 258 K and ~30% CO_2 at 273 K. This translates to CO_2 partial pressures of ~22 kPa at 258 K and ~33 kPa at 273 K which are reasonably close to the gate opening pressures observed in the pure CO_2 adsorption isotherms (~21 kPa at 258 K and ~35 kPa at 273 K). This lends credence to the interpretation that the step level in the breakthrough curve is related to the gate opening phenomenon.

Another aspect of the experimental breakthrough curves that lends credence to the proposed explanation is a sharp slowdown in the speed of gas flow through the column that occurs when the CO_2 containing gas mixture reaches the adsorbent bed. This is due to a sharp drop in the

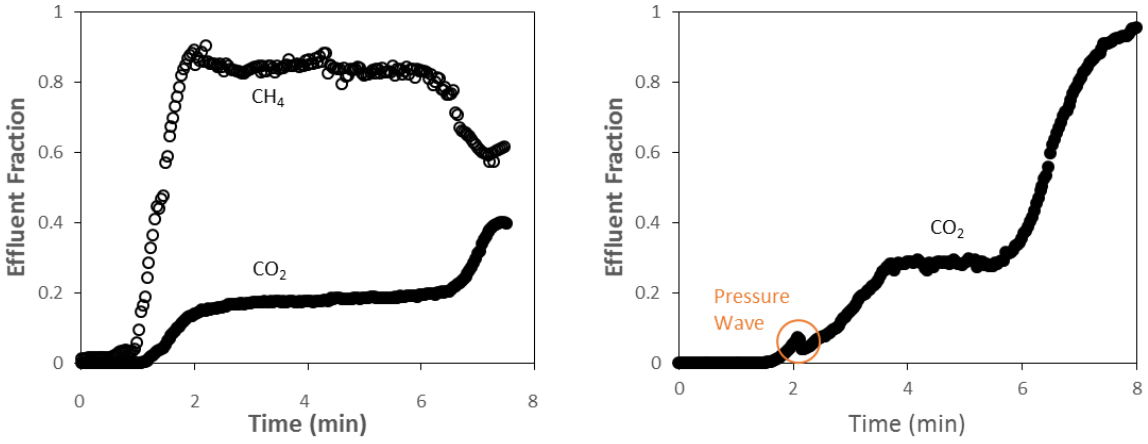

Figure 30. Breakthrough curves for a 60/40 CH_4/CO_2 mixture → He at 258 K (left) and pure CO_2 → He at 273 K (right). CO_2 and CH_4 are represented by closed and open symbols respectively.

column pressure as CO_2 is rapidly adsorbed by the ELM-11 during the gate opening process, in keeping with the explanation by Horike et al. (2012). This is can be observed in many of the breakthrough curves as a sharp drop in the measured CO_2 concentration just as the CO_2 concentration measured in the effluent outflow begins to rise. This pressure wave induced drop in the measured CO_2 concentration due to rapid adsorption on the gating ELM-11 is highlighted in Figure 30. Because the amount of gas flow influent to the column is kept constant with time, the measurement of breakthrough curves becomes difficult when the rapid adsorption of CO_2 exceeds the rate at which gas is supplied to the column. In these cases the effluent flow rate will drop to zero. Without a continuous gas flow to continue the measurement of effluent concentration it is not possible to collect accurate data on the breakthrough step level. An effluent flow rate of zero occurred most often when attempting to flow pure CO_2 through an activated column.

In order to get around this experimental shortcoming, the rest of this section relies on release curves. Because release curves involve flowing a non-adsorbing gas over an adsorbent bed that has been pre-loaded with CO_2, a carrier gas is always present in the effluent. This carrier gas prevents the sudden pressure changes observed in the breakthrough curves and also prevents the effluent flow rate from dropping to zero. Instead of a pressure wave due to rapid adsorption of CO_2, the flow rate of gas through the column increases slightly as CO_2 is desorbed from the ELM-11 adsorbent bed and joins the gas stream.

Figure 31 shows a small sample of release curves obtained by passing a flow of pure helium, nitrogen, or methane gas at various temperatures over an ELM-11 adsorbent bed preloaded with CO_2. Based on these experiments, the observed step level appears to be a function of both

temperature and mixture composition (as one would expect if the step level were a function of the gating transition).

In terms of gas properties expected to be of importance in determining the gating transition, CH_4 is nonpolar, spherical, larger than CO_2, and has been found to cause gating at high pressure (~20-40 Bar at 303 K) (Kanoh et al. 2009), N_2 is quadrupolar, linear, similar in size to CO_2, and has been found to cause gating at low temperatures (P/Po ~0.1 at 77 K) (Kajiro et al. 2010), while He is an inert, nonpolar, and spherical molecule that is considerably smaller than CO_2 (gating adsorption of helium has not been reported in the literature for ELM-11). All three gases are non-adsorbing (i.e., they do not cause a gating transition) at the temperatures and pressures explored in this work. It is interesting to note that of the three gases, release curves obtained with the smallest molecule, He, appear to have significantly lower step levels than those obtained with the largest molecule, CH_4. If CH_4 or N_2, as gases that are known to have gating adsorption, assist CO_2 with the gating process, it would be expected that they would have lower observed step levels than the inert gas, He, which should not assist significantly with the gating process.

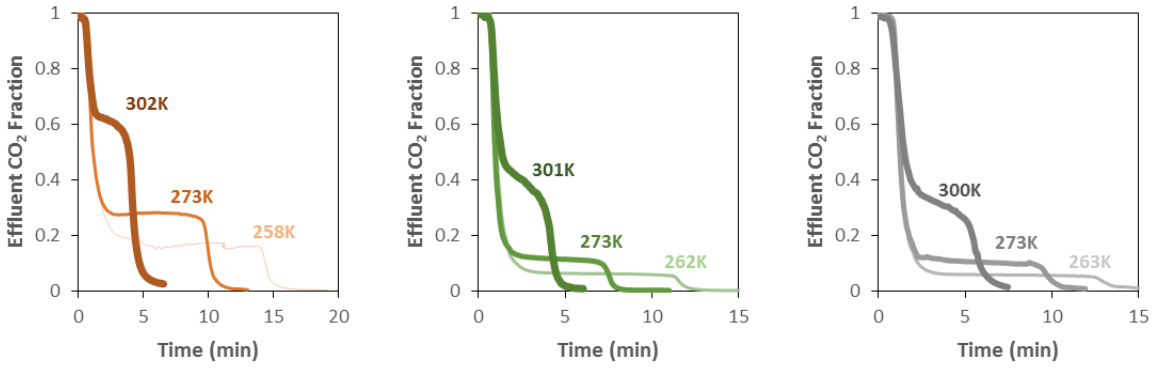

Figure 31. Release curves at various temperatures. CH4 → CO2 at 302, 273, and 258 K is shown on the left (Orange). N2 → CO2 at 301, 273, and 262 K is shown in the middle (Green). He → CO2 at 300, 273, and 263 K is shown on the right (Grey).

3.3.2 Predicting Gating and Step Transitions Using OFAST

As discussed previously, it is possible to apply the OFAST method using single component isotherms (Model 1), co-adsorption isotherms determined using IAST (Model 2), and a combination of co-adsorption isotherms determined using IAST and breakthrough experiments (Model 3) (for additional discussion of model development see sections 3.4.1 through 3.4.4). The results of each of these development routes is discusses in detail in the following sections.

3.3.2.1 Model 1

As can be seen in Figure 32, which compares the predictions of OFAST Model 1 with the desorption branches of experimental CO_2 adsorption isotherms, Model 1 can reasonably replicate both the expected CO_2 capacity and gate pressure for ELM-11 for a range of temperatures. This good model fit to the pure component isotherms is expected as pure component isotherms at various temperatures were used to fit the model. The question of interest however is whether a single component fit is useful for determining the breakthrough step level in mixed gas breakthrough curves.

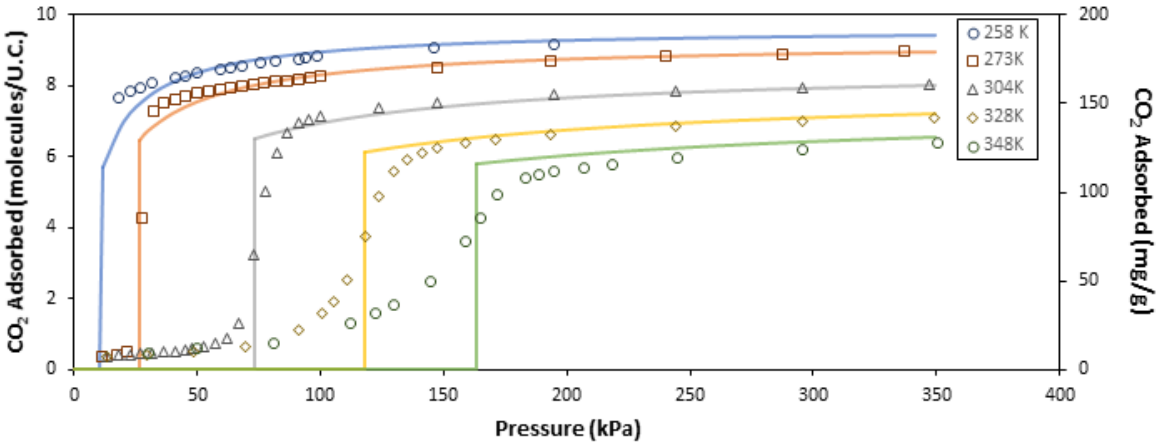

Figure 32. Comparison of OFAST Model 1 (lines) with the desorption branch of the experimental CO_2 isotherms (points) at 258 (blue circle), 273 (red square), 304 (grey triangle), 328 (yellow diamond) and 348 K (green circle). The adsorption branch was removed for clarity.

Figure 33 shows the correlation between expected values of P_{gate} obtained from OFAST Model 1 predictions and the partial pressure of CO_2 at the step levels observed in breakthrough/release curves for a range of temperatures (ranging from 255 to 315 K). The diagonal line represents a 1:1 match of expected and observed values. Points above the line indicate that the Model overestimated the partial pressure of CO_2 required to cause the step level (gating transition) at the given temperature, while points below the line indicate underestimation. Two points are included, black and red for ion 44 and ion 28 respectively, at every experimental temperature except for those experiments which include nitrogen, as nitrogen and carbon monoxide share molecular weights. In general tracking of ion 44 gives a lower observed step level than tracking of ion 28.

In general, Model 1 appears to give conservative estimates of the CO_2 partial pressure required to cause gating in ELM-11, with the majority of points indicating overestimation by the model. Of the 4 experiment types ($CH_4 \rightarrow CO_2$, $N_2 \rightarrow CO_2$, $He \rightarrow CO_2$, and $CO_2 \rightarrow He$), Model 1 best correlates with the step level observed in release curves where methane is the flush gas ($CH_4 \rightarrow CO_2$). Because Model 1 assumes that only CO_2 is important in determining the gating transition, this suggests that CH_4 does not impact the gating transition. The worst correlations

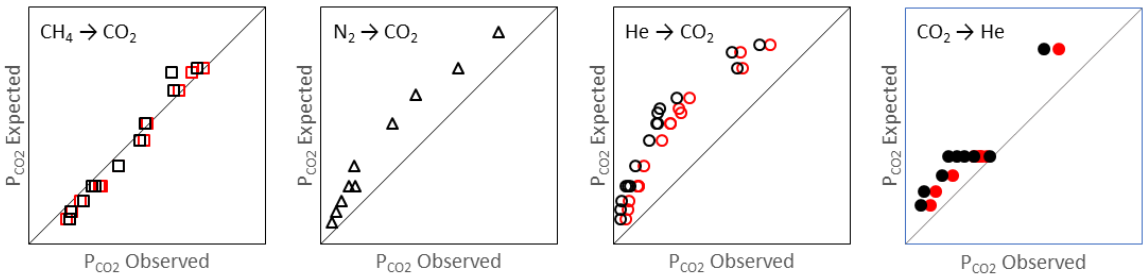

Figure 33. Correlation of OFAST Model 1 predictions of P_{CO2} required to cause the gating transition with step levels observed in experimentally obtained release curves (black outline) and breakthrough curves (blue outline). Points were determined by tracking ion 44 (black) or ion 28 (red).

are for release curves where helium is the flush gas (He→CO_2), which suggests that He does impact the gating transition in some way.

3.3.2.2 Model 2

Model 2 uses IAST to determine mixture co-adsorption before applying the OFAST method. In this case the predicted amount of CO_2 that causes gating is not reported as a partial pressure but rather as a mole fraction of the adsorbing gas mixture (Y_{CO2}) at a specified total pressure (which in this case is slightly above atmospheric: ~108 kPa). Figure 34 shows the correlation between expected values of Y_{CO2} obtained from OFAST Model 2 predictions and the mole fraction of CO_2 at the step levels observed in breakthrough/release curves at various temperatures. Note that the observed values used for comparison are the same as those used in the previous section.

Using IAST does not significantly improve the predictions for the step level in release curves where helium or nitrogen is the flush gas (N_2→CO_2 and He→CO_2) but does make the predictions where methane is the flush gas noticeably worse. Model 2 underestimates the amount of CO_2 required to initiate the step level in methane/CO_2 mixtures at lower experimental temperatures. Based on experimental/simulated single component isotherms and IAST, CH_4 should co-adsorb on ELM-11 more readily with CO_2 than N_2 or He. The combined

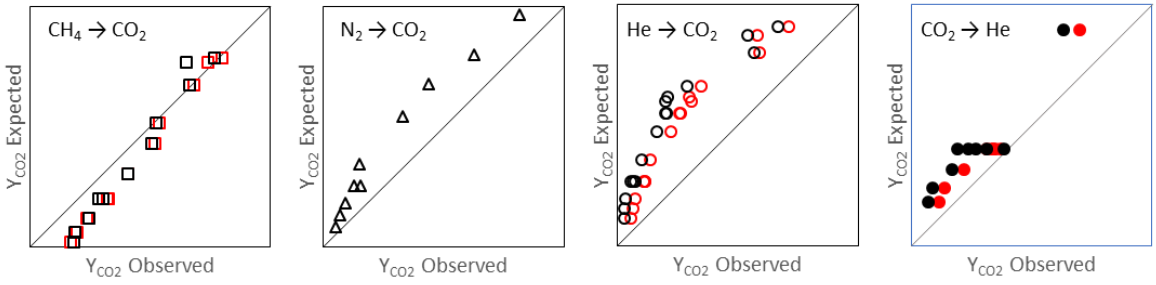

Figure 34. Correlation of OFAST Model 2 predictions of Y_{CO2} required to cause the gating transition with step levels observed in experimentally obtained release curves (black outline) and breakthrough curves (blue outline). Points were determined by tracking ion 44 (black) or ion 28 (red).

adsorption of both CO_2 and CH_4 should stabilize the ELM-11 structure and prevent gate closure until the partial pressure of CO_2 is significantly below the gate pressure expected for pure CO_2 gas adsorption. For He and N_2, single component isotherms and IAST suggest that they do not co-adsorb readily with CO_2 and therefore should not impact the expected step level by a significant amount. The experimental breakthrough curves suggest the exact opposite trend as what is predicted by using IAST.

3.3.2.3 Model 3

Model 3 also uses IAST to determine mixture co-adsorption before applying the OFAST method, but in this case the estimate of P_{gate} is taken from the observed step level. This should lead to a better fit of the expected step levels than the previous models which are derived from the gate pressure in the pure component CO_2 isotherms. This alternative route for estimating P_{gate} results in a modified estimate of the free energy difference (ΔF^{host}) between closed and open structures for different gas mixtures. The predicted amount of CO_2 that causes gating is again reported as the mole fraction of the adsorbing gas mixture (Y_{CO2}) at a specified total pressure (108 kPa). Figure 35 shows the correlation between expected values of Y_{CO2} obtained from OFAST Model 3 predictions and the mole fraction of CO_2 at the step levels observed in

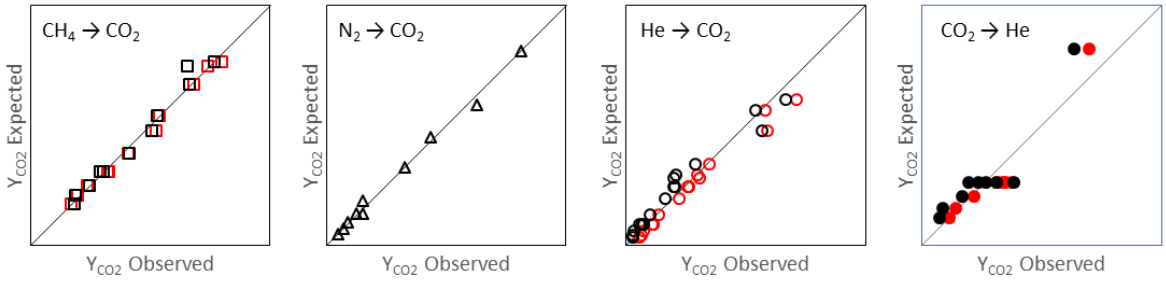

Figure 35. Correlation of OFAST Model 3 predictions of Y_{CO2} required to cause the gating transition with step levels observed in experimentally obtained release curves (black outline) and breakthrough curves (blue outline). Points were determined by tracking ion 44 (black) or ion 28 (red).

breakthrough/release curves at various temperatures. Note again that the observed values used for comparison are the same as those used in the previous two sections.

As expected, using the Y_{CO2} obtained from experiment to fit the OFAST model directly to the breakthrough curves for each gas mixture better aligns expected and observed values for all experiments and removes the curvilinear correlations observed for the $N_2 \rightarrow CO_2$ and $He \rightarrow CO_2$ experiments. This suggests that the previous poor correlations for Model 2 were due to parameter fitting rather than a failure of the underlying OFAST model formulation. The question then is whether the poor correlations for OFAST Model 2 resulted from incorrect estimates of total co-adsorption obtained from IAST or whether the free energy difference (ΔF^{host}) is more dependent on the gas mixture than previously proposed.

3.3.2.4 Size exclusion and the "door-stop" effect in ELM-11

To understand why OFAST Model 2 had poor correlations with expected values, it is necessary to explore both the assumptions underlying IAST and the impact gas molecule properties might have on the gating transition. The two main assumptions of IAST are that the components must both mix and behave as ideal gases and that the surface of the sorbent is homogeneous (Sumida et al. 2012). This assumption of homogeneity is a problem in flexible frameworks where the pore surface can adjust to accommodate gas molecules. The solution proposed by Coudert is to apply IAST separately to rigid approximations of the expanded and closed form (Coudert 2010). However, this rigid approximation may over/underestimate co-adsorption if the layer expansion required to accommodate one molecule between the layer planes is significantly different from the layer expansion required to accommodate a different molecule between the layer planes. If we compare the quantum mechanical diameters of CH_4 (4.046 Å), N_2 (3.578 Å), CO_2 (3.469 Å), and He (2.557 Å) (Mehio, Dai, and Jiang 2014), we see that CH_4 is

significantly larger than CO_2 and N_2 while He is significantly smaller. If CO_2 is the species in control of the gating transition, the layer plane expansion caused by adsorption of CO_2 may not necessarily be large enough to accommodate the larger CH_4 gas molecules. This size exclusion of CH_4 from the ELM-11 structure and resulting overestimation of co-adsorption produced by IAST would explain the good correlation of Model 1 and poor correlation of Model 2 with the step levels observed in $CH_4 \rightarrow CO_2$ release curves. This process of size exclusion is visually summarized in Figure 36.

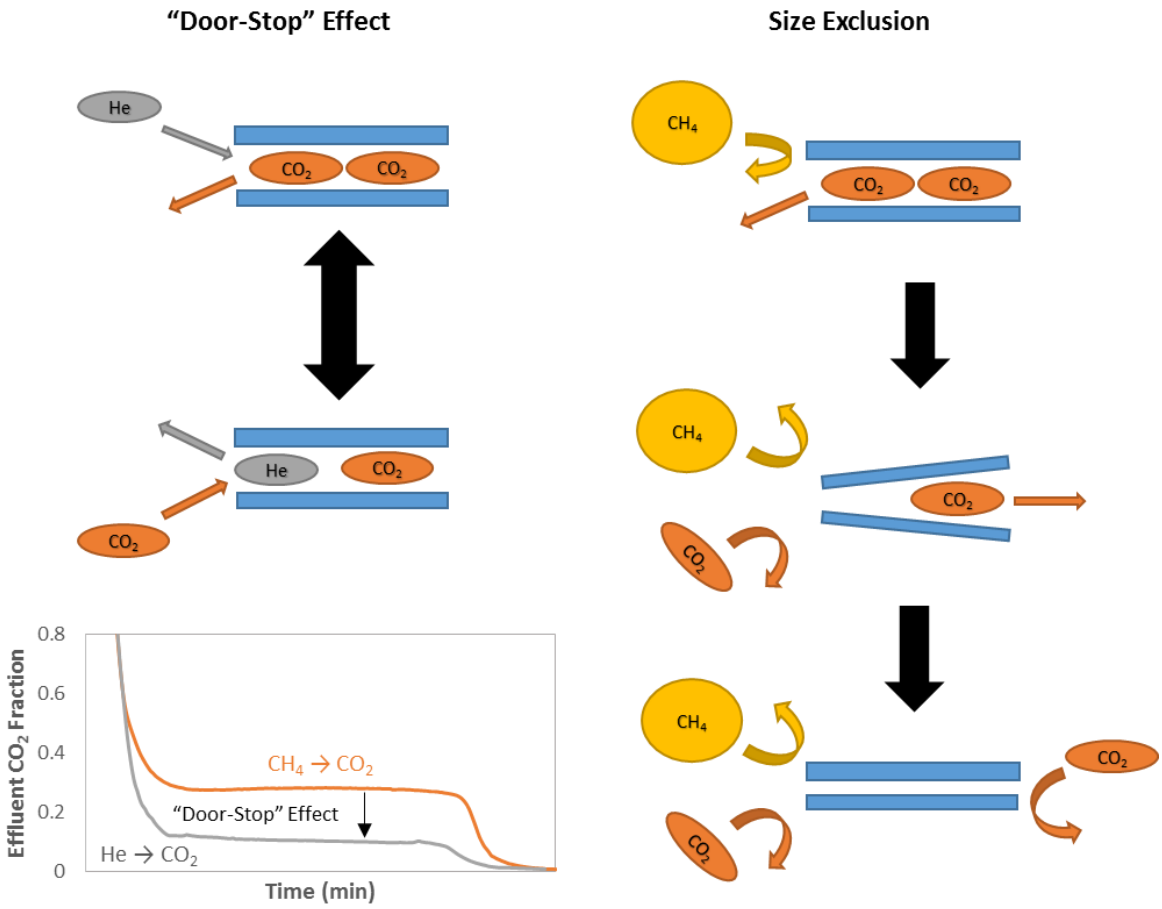

Figure 36. Visual summary of the impact of size exclusion (right) and the "door-stop" effect (left) on the gating transition. The graph (bottom-left) shows the impact of the "door-stop" effect on the breakthrough performance of ELM-11 at 273 K.

Explaining the significant overestimation of step levels obtained from Model 1 and Model 2 for the $N_2 \rightarrow CO_2$ and $He \rightarrow CO_2$ release curves is a bit more complex. The assumption of size exclusion would not apply as N_2 and He are similar in size or smaller than CO_2, but it is possible that they have an impact on the gating transition outside of impacting total molecules adsorbed. Previous work by Cheng et al. (2011) showed that the gate pressure of ELM-11 could be modified through the inclusion of trace amounts of alcohol molecules during the synthesis process. These trace molecules slightly propped open the ELM-11 structure leading to easier dehydration and lower gate pressures. Since N_2 and He are similar in size or smaller than CO_2, it is possible that a trace amount of these molecules can infiltrate the expanded ELM-11 structure while CO_2 is desorbing but before the ELM-11 structure has fully collapsed. The molecules would then serve to prop open the structure and allow CO_2 to remain adsorbed even at pressures below the gate closing pressure expected from pure CO_2 isotherms. This proposed mechanism is termed the "door-stop" effect and is also visualize summarized in Figure 36.

3.3.3 Implications for Carbon Dioxide Capture using Flexible Frameworks

The stepped breakthrough curves of flexible frameworks warn against the assumption that they can simply be switched out with currently used rigid adsorbents in gas separation applications. While the "gating" transition does appear to allow for low energy regeneration of the adsorbent material in flow-through systems, the trade-off is a hard ceiling on the amount of CO_2 that can be removed from the treated gas stream. For example, suppose >90% removal of CO_2 from a flue gas stream with a partial pressure of CO_2 of 10 kPa is desired, this translates to a desired partial pressure of CO_2 in the effluent of the adsorbent bed on the order of <1 kPa. If a gating adsorbent is used, then the gate pressure for CO_2 would also need to be <1 kPa in order to reach this desired threshold. A flexible framework with a gate pressure of 5 kPa would not adsorb

CO_2 below a partial pressure of 5 kPa and thus would only be able to capture 50% of the CO_2 in the flue gas stream. While a rigid adsorbent will adsorb some CO_2 at low partial pressures, gating frameworks will not adsorb any CO_2 below the gate pressure. This result seems obvious in retrospect but the implications have not been discussed with any depth in the literature. In contrast with rigid frameworks, the suitability of a particular flexible framework for carbon capture may depend more on the temperature dependence of its gating transition than on its measured heat of adsorption or CO_2 capacity.

3.4 Supporting Information

3.4.1 Summary of OFAST Models

A summary of the different OFAST model types is shown in Table 7. For additional details of model development and parameter fittings see section 3.4.2 (Model 1), section 3.4.3 (Model 2), and section 3.4.4 (Model 3).

Table 7. Summary of OFAST Models Types

<table>
<tr><th>OFAST Model</th><th>Gas Mixture Assumption</th><th>$P_{gate}(T)$*</th><th>$N_{max}(T)$</th><th>K(T)</th></tr>
<tr><td>Model 1</td><td>Pure CO_2</td><td rowspan="2">CO_2 Isotherm</td><td colspan="2">CO_2 Isotherm Langmuir Fit</td></tr>
<tr><td>Model 2</td><td rowspan="2">CO_2/He
CO_2/N_2
CO_2/CH_4</td><td colspan="2" rowspan="2">IAST</td></tr>
<tr><td>Model 3</td><td>Breakthrough Curves</td></tr>
</table>

*For Model 2, $\Delta F^{host}(T)$ was assumed to match the values obtained for Model 1. $P_{gate}(T)$ was then back calculated using IAST estimates of $N_{max}(T)$ and K(T).

3.4.2 Model 1 Development

As shown in Table 7, OFAST Model 1 relies on the experimental CO_2 isotherms to estimate P_{gate}, N_{max}, and K as a function of temperature. These estimates were obtained as follows. First, Langmuir fits were applied to the experimental CO_2 isotherms at 273, 308, 318, and 338 K. The Langmuir fits are shown in figure 37.

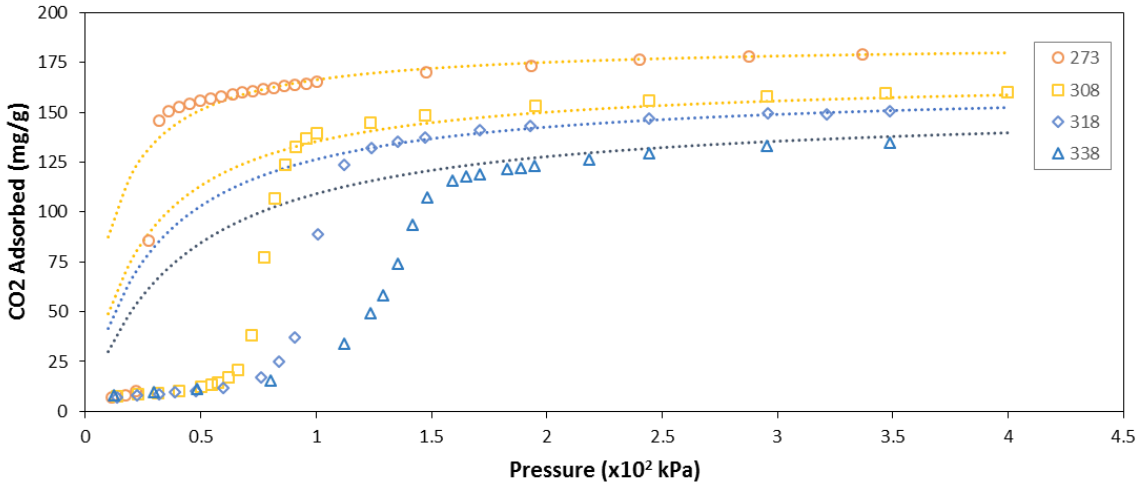

Figure 37. Langmuir Fits of Experimental Isotherms at 273 (circle), 308 (square), 318 (diamond), and 338 K (triangle). Desorption branches only. Sorption branch removed for clarity. Experiment data (points), Langmuir fit (dashed line).

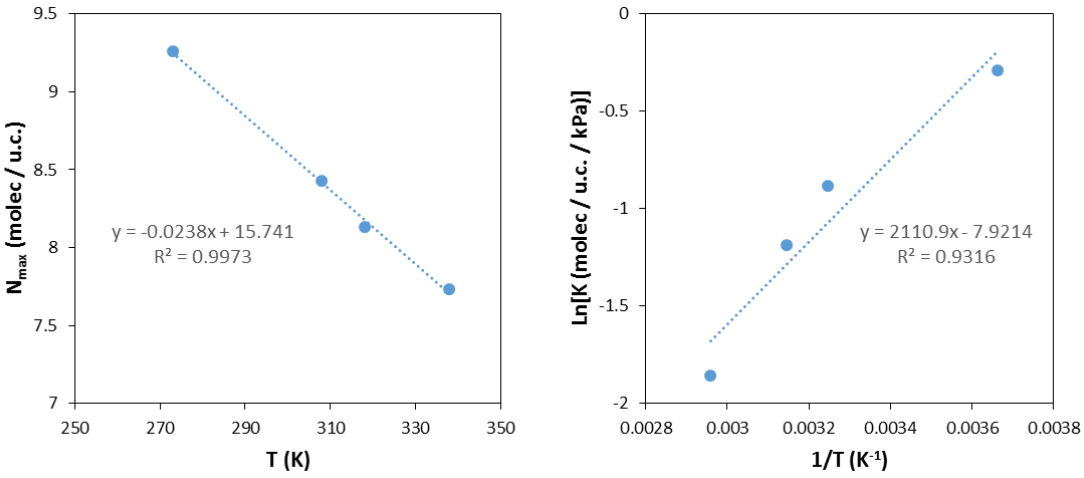

Figure 38. Variation of Langmuir parameters with temperature for CO_2 adsorption. Nmax (molecules/unit cell) vs T (Kelvins) is shown on the left. Ln[K (molecules/Unit Cell/kPa)] vs 1/T (Kelvins^{-1}) is shown on the right.

Once Langmuir fits for a range of temperatures were obtained, N_{max} and K as a function of temperature were determined graphically as show in Figure 38. After determining N_{max} and K as a function of temperature, it is necessary to estimate the gate pressure for each of the experimental isotherms in order to develop an estimate for $\Delta F^{host}(T)$. At low temperatures there is little ambiguity in the gate pressure as the experimental isotherm is nearly a vertical line at the gating transition. However, at high temperatures the gate pressure is not distinct, with significant smoothing of the gate transition. In order to provide non-arbitrary, repeatable measurements of the gate pressure even at high temperatures, the range for the gate pressure is defined here as the pressures between the minimum and maximum of the second derivative of the experimental points. For a single-point gate pressure measurement, the gate pressure is defined as the average of the pressures at the minimum and maximum of the second derivative. For the example shown in Figure 39, the gate pressure would range from 790 to 973 mmHg and the single point measurement of the gate pressure would be 882 mmHg.

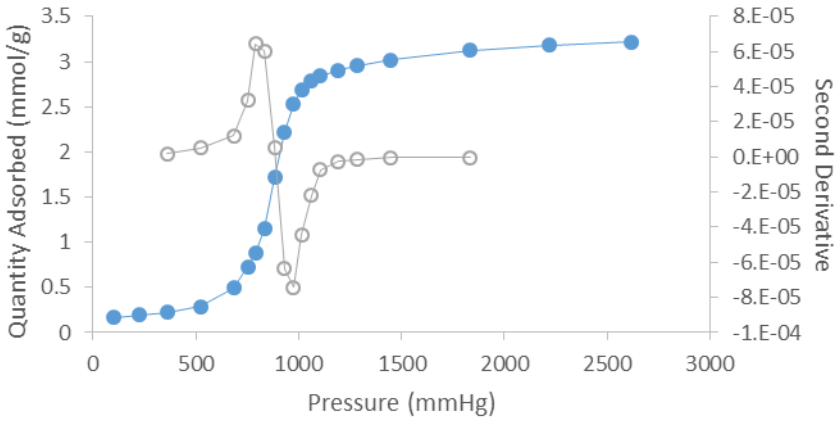

Figure 39. Determination of gate pressure for desorption branch of CO_2 isotherm measured at 328 K. Experimental isotherm (Blue, closed circles). Estimates of the second derivative (grey, open circles).

Once estimates of the gate pressure are determined, ΔF^{host} can be estimated for each measured temperature and an equation for $\Delta F^{host}(T)$ can be generated. It was found that a logistic fit of the ΔF^{host} values best matched the trend in the data for ELM-11 (for temperatures ranging from 250 to 350 K).

For the desorption branch:

$$\Delta F^{host}(T)\left[\frac{J}{mol}\right] = \frac{32173.9}{1+8.989x10^{6}*EXP(-0.06357*T)} \quad (S1)$$

For the adsorption branch:

$$\Delta F^{host}(T)\left[\frac{J}{mol}\right] = \frac{38445.4}{1+5.535x10^{6}*EXP(-0.06272*T)} \quad (S2)$$

Measured Pgate values and the OFAST model fit for both gate opening (adsorption) and gate closing (desorption) are compared in Figure 40.

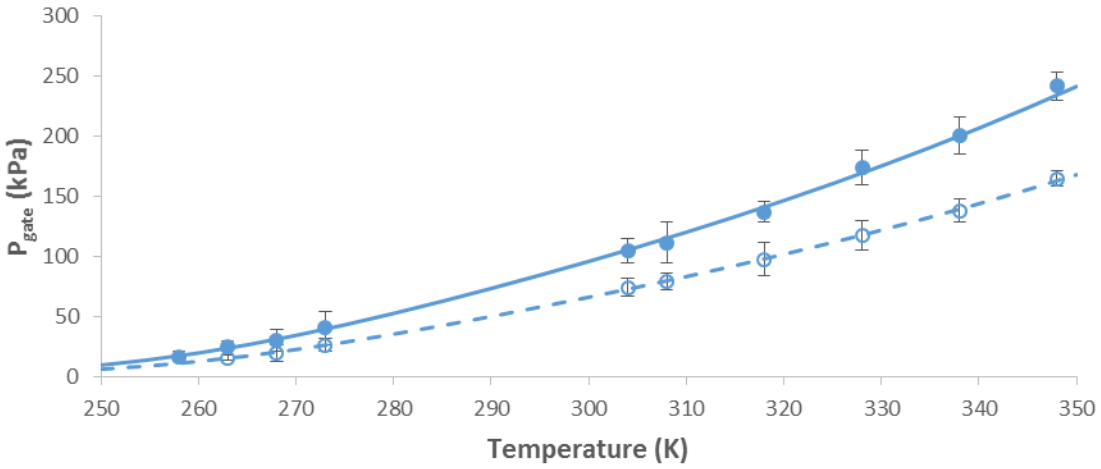

Figure 40. Comparison of experimental gate pressure (points) with OFAST Model 1 (lines). Dashed line and open symbols represent gate closing (desorption branch). Solid line and closed symbols represent gate opening (adsorption). Error bars represent the width of the gate as measured by the maximum and minimum in the second derivative.

3.4.3 Model 2 Development

For Model 2 it is assumed that free energy difference (ΔF^{host}) between the collapsed and open crystal structure estimated for Model 1 has not changed. However, instead of solely using the Langmuir fit of the experimental CO_2 isotherms to determine N_{max} and K, mixed gas adsorption is assumed and the ideal gas adsorbed solution theory (IAST) is used to determine mixture co-adsorption on the expanded ELM-11 structure. To obtain IAST estimates for the gas mixtures, both the experimental CO_2 isotherms in section 3.4.2 and additional pure component isotherms for He, N_2, and CH_4 obtained from GCMC simulations are used. First the Langmuir parameters for the He, N_2, and CH_4 isotherms are obtained from GCMC simulations. The variation with temperature for these Langmuir parameters are shown in Figures 41, 42, and 43.

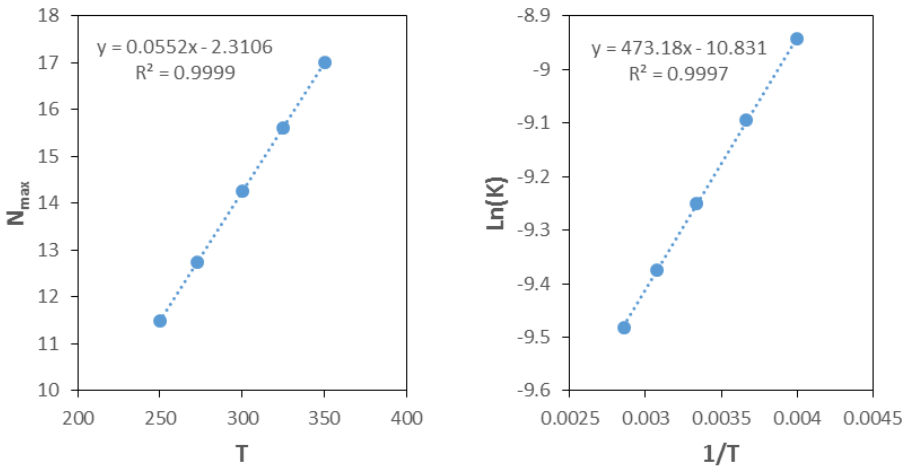

Figure 41. Variation of Langmuir parameter with temperature for He adsorption. Nmax (molecules/unit cell) vs T (Kelvins) is shown on the left. Ln[K (molecules/Unit Cell/kPa)] vs 1/T (Kelvins^{-1}) is shown on the right.

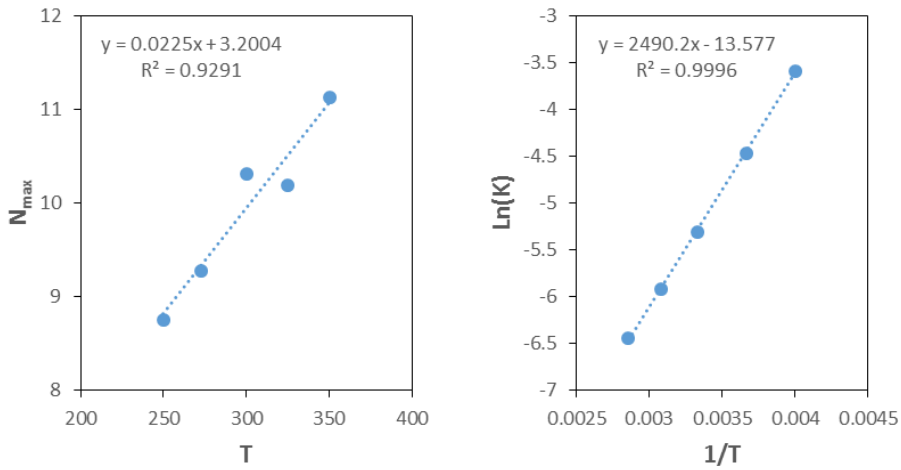

Figure 42. Variation of Langmuir parameter with temperature for N_2 adsorption. Nmax (molecules/unit cell) vs T (Kelvins) is shown on the left. Ln[K (molecules/Unit Cell/kPa)] vs 1/T (Kelvins^{-1}) is shown on the right.

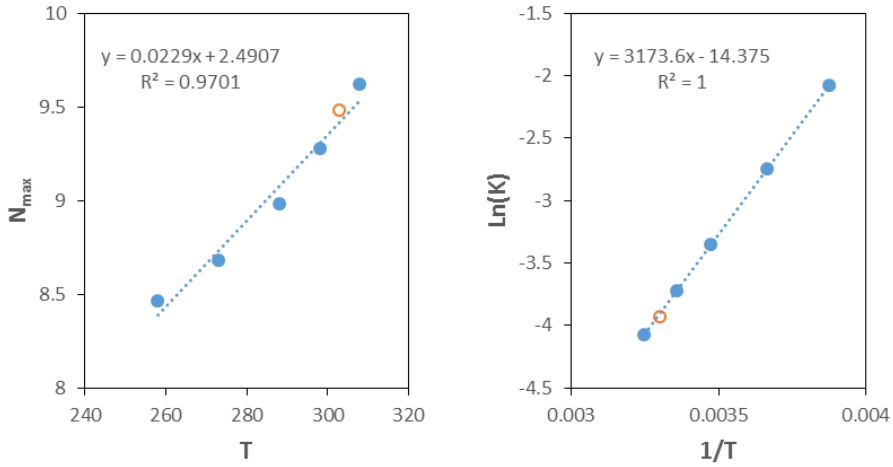

Figure 43. Variation of Langmuir parameters with temperature for CH_4 adsorption. Nmax (molecules/unit cell) vs T (Kelvins) is shown on the left. Ln[K (molecules/Unit Cell/kPa)] vs 1/T (Kelvins^{-1}) is shown on the right. Closed symbols represent points used for trend line fit, open symbol represents a simulated value not included in the trend line fit.

Once the Langmuir parameters for all single component isotherms are known then the total amount of a gas mixture adsorbed at a particular temperature, pressure, and mixture composition can be found numerically by solving the IAST systems of equations as described by Coudert (2010). In the current work, the numerical solution was found using a custom code

in MATLAB (MATLAB and Statistics Toolbox 2015). A sample code which determines Pgate using OFAST and IAST is shown in section 3.4.7.

3.4.4 Model 3 Development

For Model 3, it is assumed that the mixture co-adsorption isotherm parameters (N_{max} and K) obtained from Model 2 are the same, but instead of using single component CO_2 isotherms to estimate P_{gate}, estimates of P_{gate} were obtained directly from the breakthrough experiments for the different gas mixtures. As in the case of the gating transition, the step level is not a distinct point, with significant smoothing of the step, especially at high temperatures. In order to provide non-arbitrary, repeatable measurements of the step level observed in breakthrough experiments, the single point measurement of the step level is defined here as the median value of the experimental points between the two peaks in the first derivative of the breakthrough curve. For the example shown in Figure 44, the time stamps included in the step anomaly would range from 0.731 to 4.072 minutes and the single point measurement of the step level would be a CO_2 fraction of 0.632.

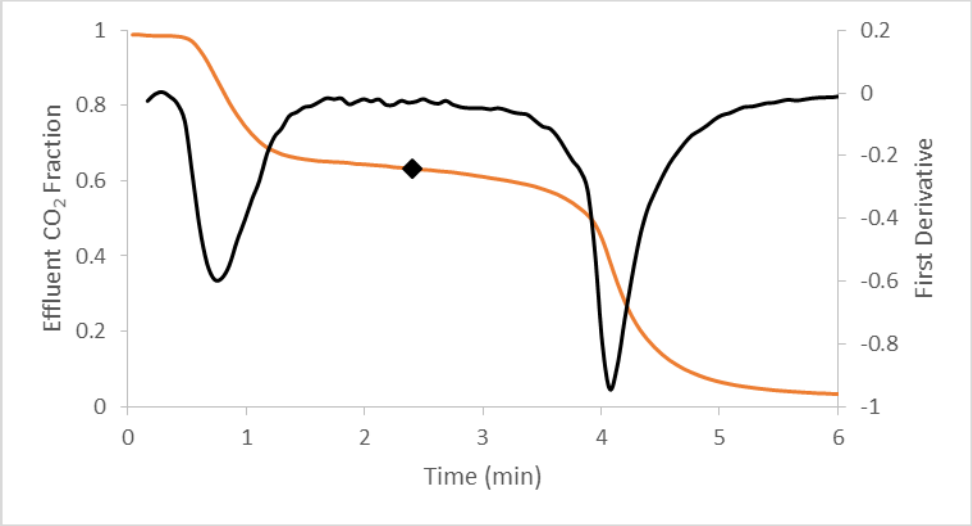

Figure 44. Determination of the step level (black diamond) for a $CH_4 \rightarrow CO_2$ release curve (orange line) measured at 302 K using the first derivative (black line).

Once estimates of the step levels are determined, ΔF^{host} is estimated for each measured temperature and mixture composition and an equation for $\Delta F^{host}(T)$ can be generated for each experiment type. A linear fit was used for each gas mixture to determine the trend in ΔF^{host} values for temperatures ranging from 250 to 320 K. The ΔF^{host} values for release curves are shown in Figure 45 and compared with the ΔF^{host} values obtained from pure CO_2 isotherms.

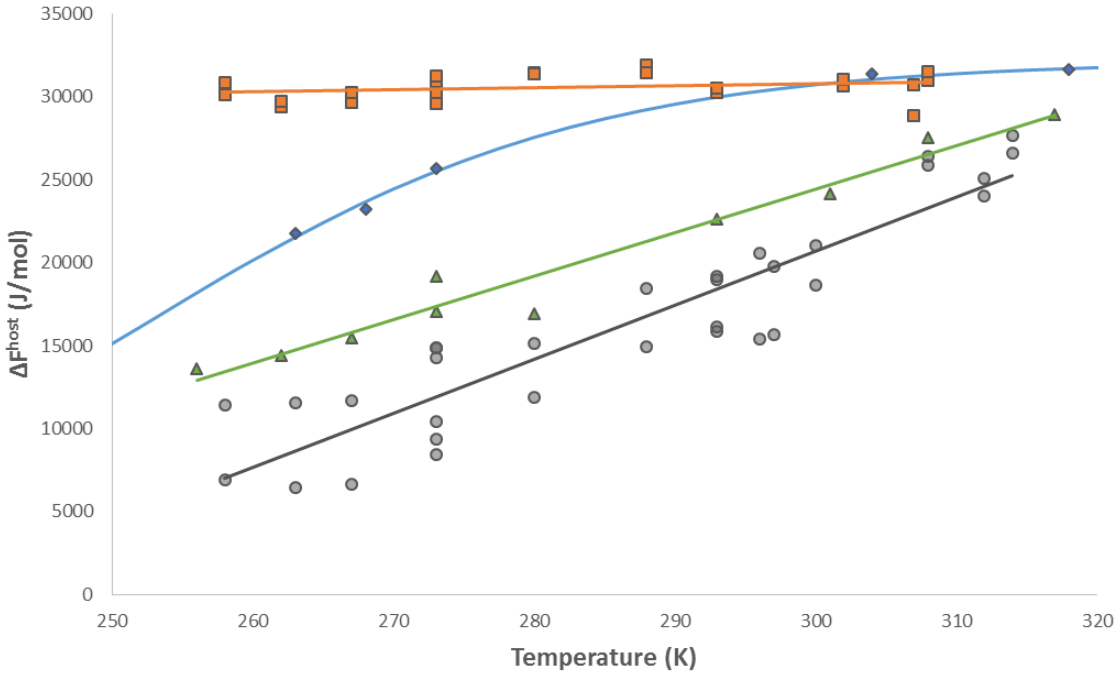

Figure 45. Comparison of ΔF^{host} values obtained using Model 1 (blue diamonds) with those obtained using Model 3: He→CO_2 release curves (grey circles), N_2→CO_2 release curves (green triangles), and CH_4→CO_2 release curves (orange squares).

For the He→CO_2 release curves (r^2 = 0.848):

$$\Delta F^{host}(T)\left[\frac{J}{mol}\right] = 325.58 * T - 76983 \quad \text{(S3)}$$

For the N_2→CO_2 release curves (r^2 = 0.963):

$$\Delta F^{host}(T)\left[\frac{J}{mol}\right] = 261.61 * T - 54058 \quad \text{(S4)}$$

For the $CH_4 \rightarrow CO_2$ release curves ($r^2 = 0.072$):

$$\Delta F^{host}(T)\left[\frac{J}{mol}\right] = 12.139 * T + 27143 \quad \text{(S5)}$$

For the $CO_2 \rightarrow He$ breakthrough curves ($r^2 = 0.549$):

$$\Delta F^{host}(T)\left[\frac{J}{mol}\right] = 409.79 * T - 86409 \quad \text{(S6)}$$

3.4.5 Comparison of CH_4 Simulated Isotherm with Reported Experiment

Figure 46 shows the results of a GCMC simulation for CH_4 adsorption on ELM-11 at 303 K overlaying the reported results of a cyclic CH_4 adsorption experiment at 303 K reported by Kanoh et al. (2009). The GCMC simulation shows good agreement with the previously reported maximum CH_4 capacity.

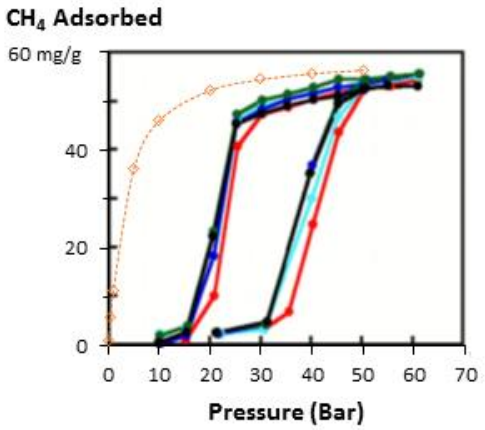

Figure 46. Comparison of simulated CH_4 isotherm (open diamonds) reported here with cyclic CH_4 isotherms (closed circles) at 303 K reported by Kanoh et al. (2009)

3.4.6 Sample Towhee GCMC Input File for N_2 on ELM-11 at 273 K and 25 kPa

inputformat
'Towhee'
randomseed
1302002
random_luxlevel

3
random_allow_restart
T
ensemble
'uvt'
temperature
273.0
nmolty
2
nmolectyp
320 900
chempot
 # 273k 25kpa n2
0.0 -4574.74111
numboxes
1
stepstyle
'moves'
nstep
10000000
printfreq
500000
blocksize
500000
moviefreq
1000000
backupfreq
500000
restartfreq
0
runoutput
'full'
pdb_output_freq
500000
loutdft
F
loutlammps
F
loutdlpoly
F
louthist
T
hist_label
1
hist_suffix
a

hist_nequil
0
histcalcfreq
100000
histdumpfreq
100000
pressurefreq
300000
trmaxdispfreq
100000
volmaxdispfreq
100000
chempotperstep
0 0 0
potentialstyle
'internal'
ffnumber
5
ff_filename
/home/software/rhel5/towhee/6.2.7/ForceFields/towhee_ff_DREIDING
/home/software/rhel5/towhee/6.2.7/ForceFields/towhee_ff_TraPPE-EH
/home/software/rhel5/towhee/6.2.7/ForceFields/towhee_ff_TraPPE-UA
classical_potential
'Lennard-Jones'
classical_mixrule
'Lorentz-Berthelot'
lshift
F
ltailc
F
rmin
1.0
rcut
14.000000000000
rcutin
5.0000000000000
electrostatic_form
'coulomb'
coulombstyle
'ewald_fixed_kmax'
kalp
5.6
kmax
5
dielect
1.0

nfield
0
solvation_style
'none'
linit
T
initboxtype
'dimensions'
initstyle
'coords' 'coords' 'coords'
initlattice
'none' 'none' 'none'
initmol
320 0
inix iniy iniz
8 4 10
hmatrix
#ELM-11 105 expand 2x box
88.42020264 0.00000000 0.00000000
0.00000054 44.28800000 0.00000000
36.81288905 55.36000048 60.66189212
pmuvtcbswap
0.4
pmuvtcbmt
0.0 1.0
pmtracm
0.7
pmtcmt
0.0 1.0
rmtrac
0.5000
tatrac
0.5000
pmrotate
1.0
pmromt
0.0 1.0
rmrot
0.0500
tarot
0.5000
cbmc_style
'coupled-decoupled'
coupled_decoupled_form
'Martin and Siepmann JPCB 1999'
cbmc_setting_style

'default ideal'
#Cu_MOF-2a 2x4x10 DREIDING implicit H no bonds
input_style
'basic connectivity map'
nunit
35
nmaxcbmc
35
lpdbnames
F
forcefield
'DREIDING'
charge_assignment
'manual'
unit ntype qqatom
1 Fe_+2 0.52800
vibration
0
improper torsion
0
unit ntype qqatom
2 B_3 0.84300
vibration
0
improper torsion
0
unit ntype qqatom
3 B_3 0.84300
vibration
0
improper torsion
0
unit ntype qqatom
4 F_   -0.40900
vibration
0
improper torsion
0
unit ntype qqatom
5 F_   -0.36000
vibration
0
improper torsion
0
unit ntype qqatom
6 F_   -0.36000

vibration
0
improper torsion
0
unit ntype qqatom
7 F_ -0.36000
vibration
0
improper torsion
0
unit ntype qqatom
8 F_ -0.40900
vibration
0
improper torsion
0
unit ntype qqatom
9 F_ -0.36000
vibration
0
improper torsion
0
unit ntype qqatom
10 F_ -0.36000
vibration
0
improper torsion
0
unit ntype qqatom
11 F_ -0.36000
vibration
0
improper torsion
0
unit ntype qqatom
12 C_R 0.07400
vibration
0
improper torsion
0
unit ntype qqatom
13 C_R1 0.00100
vibration
0
improper torsion
0

unit ntype qqatom
14 C_R1 0.25900
vibration
0
improper torsion
0
unit ntype qqatom
15 C_R   0.07400
vibration
0
improper torsion
0
unit ntype qqatom
16 C_R1 0.00100
vibration
0
improper torsion
0
unit ntype qqatom
17 C_R1 0.25900
vibration
0
improper torsion
0
unit ntype qqatom
18 C_R1 0.00100
vibration
0
improper torsion
0
unit ntype qqatom
19 C_R1 0.25900
vibration
0
improper torsion
0
unit ntype qqatom
20 C_R   0.07400
vibration
0
improper torsion
0
unit ntype qqatom
21 C_R1 0.25900
vibration
0

improper torsion
0
unit ntype qqatom
22 C_R1 0.00100
vibration
0
improper torsion
0
unit ntype qqatom
23 C_R1 0.00100
vibration
0
improper torsion
0
unit ntype qqatom
24 C_R1 0.25900
vibration
0
improper torsion
0
unit ntype qqatom
25 C_R1 0.00100
vibration
0
improper torsion
0
unit ntype qqatom
26 C_R1 0.25900
vibration
0
improper torsion
0
unit ntype qqatom
27 C_R1 0.00100
vibration
0
improper torsion
0
unit ntype qqatom
28 C_R1 0.25900
vibration
0
improper torsion
0
unit ntype qqatom
29 C_R   0.07400

vibration
0
improper torsion
0
unit ntype qqatom
30 C_R1 0.25900
vibration
0
improper torsion
0
unit ntype qqatom
31 C_R1 0.00100
vibration
0
improper torsion
0
unit ntype qqatom
32 N_R   -0.40300
vibration
0
improper torsion
0
unit ntype qqatom
33 N_R   -0.40300
vibration
0
improper torsion
0
unit ntype qqatom
34 N_R   -0.40300
vibration
0
improper torsion
0
unit ntype qqatom
35 N_R   -0.40300
vibration
0
improper torsion
0
 # TraPPE-EH N2
input_style
'basic connectivity map'
nunit
* 3*
nmaxcbmc

3
lpdbnames
F
forcefield
'TraPPE-EH'
charge_assignment
'manual'
unit ntype qqatom
1 'COM_n2' 0.964
vibration
2
2 3
improper torsion
0
unit ntype qqatom
2 'N_n2' -0.482
vibration
1
1
improper torsion
0
unit ntype qqatom
3 'N_n2' -0.482
vibration
1
1
improper torsion
0

3.4.7 Sample MATLAB Code for using OFAST and IAST

```
%Define other factors
R = 8.314462;

%initial Dummy Matrix
P_out = zeros(399,11);
Pgate_out = zeros(399,3);
CoefOpen = zeros(399,4);
P_all = zeros(100,1);
Ntot_o = zeros(100,1);

% Set up fittype and options.
ft = fittype( 'k*x/(1+k*x/n)', 'independent', 'x', 'dependent', 'y' );
opts = fitoptions( 'Method', 'NonlinearLeastSquares' );
opts.Display = 'Off';
opts.Lower = [0 0];
opts.Robust = 'LAR';
opts.StartPoint = [1 8];
```

```
L = 32173.95434;
A = 8989582.641;
a = 0.063566682;

for t = 1:1:21; %runnning through variable Tempts
    T = 245+5*t
    deltaFhost = L/(1+A*exp(-1*a*T));%Fhost fit to temp (logistic Fit)

    %Open Structure
    %langmuir parameters for CO2 (Fit by Temp)
    Nb = 15.741-0.0238*T;
    Kb = exp(2110.9*1/T-7.9214);
    %then langmuir parameters for He(Fit by temp)
    Nc = 0.0552*T - 2.3106;
    Kc = exp(473.18*1/T - 10.831);

    %Closed Structure: Not Used Here

    for j = 1:1:19;
        %defining the mol fraction y of the mix
        yb = j*0.05; %i.e. mix is (j*0.05)% CO2
        yc = 1-yb;
        %timer = j

        %develop a For loop to calculate all Pbs and  from 5 to 500 kPa
        for n = 1:1:100
            %set the pressure in kpa
            P = n*5;
            %Now I want to solve for Pb* (denoted Pb)
            syms x; %denotes x as a dummy variable
            Pb = vpasolve(P*yc*x/(x-P*yb) == Nc/Kc*((1+Kb*x/Nb)^(Nb/Nc)-
1),x,P*yb*1.001);

            %calculate the rest
            %Open
            xb = P*yb/Pb; %fraction CO2 adsorbed
            xc = 1-xb; %fraction He adsorbed

            Pc = (P - Pb*xb)/(1-xb); %fictitious pressure Pc*
            Nb_fic = Kb*Pb/(1+Kb*Pb/Nb); %fictitious amount of CO2, CO2
sees
            Nc_fic = Kc*Pc/(1+Kc*Pc/Nc); %ficticious amount of He, He sees
            Ntot = 1/(xb/Nb_fic + xc/Nc_fic); %calculation of N total
            alpha = (xb/xc)/(yb/yc); %calculation of selectivity

            %output to matrix
            P_all(n,1)= P;
            Ntot_o(n,1)= Ntot;

            if P==100;
                P_out(j+19*(t-1),1)= P;
                P_out(j+19*(t-1),2)= T;
                P_out(j+19*(t-1),3)= yb;
                P_out(j+19*(t-1),4)= Pb;
```

```
                P_out(j+19*(t-1),5)= Pc;
                P_out(j+19*(t-1),6)= xb;
                P_out(j+19*(t-1),7)= xc;
                P_out(j+19*(t-1),8)= Nb_fic;
                P_out(j+19*(t-1),9)= Nc_fic;
                P_out(j+19*(t-1),10)= Ntot;
                P_out(j+19*(t-1),11)= alpha;
            end
        end

        % Fit model to data.
        [fitresult, gof] = fit( P_all, Ntot_o, ft, opts );
        CoefOpen(j+19*(t-1),1) = yb;
        CoefOpen(j+19*(t-1),2) = fitresult.k;
        CoefOpen(j+19*(t-1),3) = fitresult.n;
        CoefOpen(j+19*(t-1),4) = gof.rsquare;

        K2 = CoefOpen(j+19*(t-1),2);
        N2 = CoefOpen(j+19*(t-1),3);

        Pgate = vpasolve(0==deltaFhost - R*T*(N2*log(1+K2*x/N2)),x,60);
        Pgate_out(j+19*(t-1),1) = T;
        Pgate_out(j+19*(t-1),2) = yb;
        Pgate_out(j+19*(t-1),3) = Pgate;
    end
end

for i = 1:1:399
    if P_out(i,1)<Pgate_out(i,3)
        P_out(i,4)= 0;
        P_out(i,5)= 0;
        P_out(i,6)= 0;
        P_out(i,7)= 0;
        P_out(i,8)= 0;
        P_out(i,9)= 0;
        P_out(i,10)= 0;
        P_out(i,11)= 0;
    end
end
```

CHAPTER 4

Mobile Carbon Capture

In this chapter, mobile carbon capture as a strategy to reduce carbon dioxide emissions from the transportation sector is explored. The thermodynamic minimum work to separate CO_2 from the exhaust stream of vehicles is similar to that of stationary power and significantly less than that of competing direct air capture. A mobile system which captures carbon dioxide from the first 30 miles of a vehicle's daily commute and is regenerated daily could reduce emissions from automobiles in the U.S. by 80%. Completing sorbent regeneration and CO_2 compression off-board the vehicle using CO_2-free electric power could reduce operational power costs by 50% over mobile capture systems that use energy derived from the car engine, while preventing additional CO_2 emissions. Mobile carbon capture is likely to cost on the order of $300 per tonne of CO_2 avoided, significantly cheaper than the $600-$1000 per tonne of CO_2 expected for direct air capture. The majority of the cost premium over stationary capture at power plants can be attributed to the costs of sorbent transport. It is expected that mobile capture will carry a cost 2-5 times that of stationary capture at power plants, significantly less than the 10 times estimated for direct air capture.

4.1 Why Mobile Carbon Capture?

Emissions of greenhouse gases into the atmosphere from anthropogenic sources have been recognized as the largest contributors to positive radiative forcing and global climate change.

The Intergovernmental Panel on Climate Change (IPCC 2013) reports that atmospheric concentrations of carbon dioxide (CO_2), methane, and nitrous oxide have increased to levels unprecedented in at least the last 800,000 years. CO_2 concentrations have increased by 40% since pre-industrial times, primarily from fossil fuel emissions and secondarily from net land use change emissions. Controlling such emissions is a long term sustainability challenge.

The transportation sector is a significant source of these fossil fuel emissions. Use of petroleum for the purpose of transportation is the source of nearly 27% of U.S. CO_2-eq emissions (EPA 2016) (see Chapter 1, Figure 12), with light duty vehicles making up 60% of these greenhouse gas emissions (EPA 2012). Reducing these emissions represents a difficult challenge, with significant social, economic, and technological barriers. Combustion of gasoline fuel in transportation has many advantages over alternative sources of energy for the average consumer. Gasoline has a high energy density compared with alternative fuels (Table 8) and a typical gasoline vehicle can be driven over 300 miles without refueling. For comparison, typical electric vehicles available today for the average consumer have an expected all-electric range of 60-120 miles (high performance electric vehicles can reach nearly 300 miles but are significantly more expensive than the average). In addition, transportation and storage of liquid petroleum is easier relative to gaseous fuels like natural gas or hydrogen and the necessary infrastructure for refueling is already in place. Without significant technological improvement in alternative mobility schemes, widespread use of petroleum for transportation is likely to continue for the foreseeable future. If travel demand and vehicle energy efficiency are held constant, and widespread fuel switching away from petroleum based fuels for transportation is absent, the only obvious alternative for controlling CO_2 emissions from transportation is CO_2 capture.

Table 8. Energy Density of Transportation Fuels (Sullivan and Sivak 2012)

Fuel type	Energy Density (MJ/L)
Gasoline	32-35
Propane	25 (compressed at 12 bar)
Ethanol	21-24
Natural Gas	9 (compressed at 250 bar)
Hydrogen	5.6 (compressed at 700 bar)

Carbon capture strategies for mobile sources can be separated into two categories (DeCicco 2015): atmospheric removal strategies, and on-board mobile carbon capture (MCC). Atmospheric removal strategies refer to any number of techniques which capture CO_2 from air, where the concentration is on the order of 400 ppm or 0.04% by volume, using either chemical, physical or biological means. Of most interest here is the use of physical techniques which rely on air scrubbers to perform direct air capture (DAC) as this method is grounded in the theory and practice behind carbon capture and storage technologies. DAC has recently been the subject of intense debate, with a number of published articles tackling its feasibility and likely cost (Socolow et al. 2011; Keith, Ha-Duong, and Stolaroff 2005; Lackner 2009; Heidel et al. 2011; Zeman 2007; Zeman 2014; House et al. 2011; Baciocchi, Storti, and Mazzotti 2006; Holmes and Keith 2012; Goeppert et al. 2012; Brandani 2012; Pritchard et al. 2015; Pielke 2009; Lackner et al. 2012; Jones 2011; Ruthven 2014). Although referred to here and elsewhere as an emission reduction strategy, DAC is actually more of a climate engineering strategy, with the ability to affect global atmospheric concentrations of CO_2.

The alternative to DAC for controlling transportation emissions is MCC. In contrast to DAC, MCC has received limited attention from carbon capture researchers. MCC refers to the on-board capture of CO_2 from vehicle exhaust, where concentrations are on the order of 13.5% by volume (Taylor 1993), with periodic offloading of the captured CO_2. The majority of mentions

of mobile carbon capture in the literature come from the DAC studies where it's assumed infeasibility or impracticality is used as evidence to support the research and implementation of DAC to manage mobile emissions. For example, a recent review on carbon capture by Boot-Handford et al. (2014) reduced mobile capture to a single uncited sentence in support of DAC:

> *"Air capture could also offer an option for addressing CO_2 emissions from mobile and distributed sources, such as vehicles, fuel use in buildings and geographically isolated industry, where direct capture and integration into a centralised CCS network would be either impractical and/or uneconomical."*

Outside of mentions in the DAC literature, actual studies into the feasibility of MCC are limited. A study by Bilger and Wu (2009) explored the possible benefits of a modified internal combustion rankine engine with oxy-fuel based carbon capture. Damm and Fedorov (2008) explored the possibility of a sustainable carbon economy that incorporated distributed carbon capture. More recently, Sullivan and Sivak (2012) reviewed potential consumer support for mobile carbon capture. Other works on the subject include studies by Kato, Otsuka, and Liu (2005) and Seifritz (1993). Given that CO_2 concentrations in vehicle exhaust are over 300 times greater than the concentrations in ambient air, it seems unlikely that DAC would represent a significant energy and cost savings over MCC as has been suggested by the DAC literature. A study into the theoretical feasibility, design trade-offs, and expected costs of a MCC system is needed in order to understand the actual social, economic, and technical barriers to implementation.

4.2 Theoretical Feasibility and Cost

There is no theoretical basis for why DAC would be implemented at wide scale before MCC. In actuality, implementation of MCC would likely represent a significant savings in energy

and cost over DAC. To see why it is instructive to calculate the minimum work requirements for CO_2 separation for both MCC and DAC systems and then compare these systems with the more developed post-combustion capture (PCC) at coal power plants.

The minimum work required for separating CO_2 from a gas mixture for an isothermal and isobaric process is equal to the difference in Gibbs free energy between the initial and final states (Wilcox 2012). For the simplified case of separating one feed stream, A, into two product streams, B and C, where all streams are composed of ideal gasses, the minimum work reduces to:

$$W_{min} = RT\left[n_B^{CO_2}\ln\left(y_B^{CO_2}\right) + n_B^{B-CO_2}\ln\left(y_B^{B-CO_2}\right)\right]$$
$$+RT\left[n_C^{CO_2}\ln\left(y_C^{CO_2}\right) + n_C^{C-CO_2}\ln\left(y_C^{C-CO_2}\right)\right]$$
$$-RT\left[n_A^{CO_2}\ln\left(y_A^{CO_2}\right) + n_A^{A-CO_2}\ln\left(y_A^{A-CO_2}\right)\right] \quad (1)$$

where R is the ideal gas constant (8.314 J/mol K), T is the absolute temperature, $y_i^{CO_2}$ is the mole fraction of CO_2 in the gas mixture, *i*, such that *i* can represent either stream A, B, or C, and $y_i^{i-CO_2}$ represents the remainder of a given gas stream A, B, or C. For comparison purposes between systems it is easier to use the minimum work per unit mass of CO_2 captured,

$$w_{min} = W_{min}/\left(n_{CO_2} * M_{CO_2}\right) \quad (2)$$

where n_{CO_2} is the moles of CO_2 captured and M_{CO_2} is the molecular weight of CO_2. In the ideal case where 100% capture of pure CO_2 from the feed stream is achieved, the minimum work per unit mass of CO_2 captured reduces to:

$$w_{min,100\%} = -\frac{RT}{yM_{CO_2}}[y\ln(y) + (1-y)\ln(1-y)] \quad (3)$$

where y is the mole fraction of CO_2 in the feed stream. In all cases discussed, the minimum work depends strongly on both the fraction of CO_2 present in the feed stream and the percent capture of CO_2 desired. Typical mole fractions of CO_2 are 0.12 in coal flue gas, 0.0004 in atmospheric air, and 0.135 in automobile exhaust. The reason automobile exhaust typically has a higher mole fraction of CO_2 than coal power plant flue gas is that automobiles tend to run at or near ideal air-fuel ratios for environmental and performance reasons, while power plants tend to operate with excess air. A sample of minimum work required for MCC, PCC, and DAC systems calculated using equations 1, 2, and 3 are shown in Table 9.

Table 9. Minimum Work to Capture CO_2 in MCC, PCC, and DAC at 298 K (kJ/kg CO_2 Captured)

Percent of CO_2 Captured	Purity of Captured CO_2	MCC (0.135 CO_2)	PCC (0.12 CO_2)	DAC (0.0004 CO_2)
100%	100%	165	172	497
90%	98%	145	153	477
75%	98%	135	141	465
50%	98%	123	129	452

Theoretically, due to the high CO_2 fraction present in automobile exhaust, MCC has the lowest minimum work requirements, slightly below those of PCC. In comparison, the minimum work requirements for DAC are significantly higher (3-4 times that of MCC). This large difference in minimum work requirement between MCC and DAC becomes even more of an issue when you consider that "real-world" separation processes typically only achieve second-law efficiencies (η_{2nd}), defined as the ratio of thermodynamic minimum work to actual power consumption, on the order of 5–40% (House et al. 2011). In addition, separation process that deal with low concentrations, like air capture, tend to have low second-law efficiencies as well. On the basis of the energy required to perform the separation, there is no apparent benefit to

allowing the CO_2 in the exhaust gas to dilute through emission to the atmosphere before attempting direct air capture elsewhere.

A similar story can be constructed on the basis of cost through the use of Sherwood plots. Sherwood plots are empirically derived correlations that show an inverse relationship between the market price of substances and their initial environmental concentrations. Dahmus and Gutowski (2007) postulated that this inverse relationship can be attributed to material extraction and processing costs that scale with the amount of material processed. A parallel can and has been made by previous authors to the separation of gases. House et al. (2011) and Wilcox (2012) have both developed Sherwood plot correlations in order to give first pass estimates of the cost of DAC. Estimates of the expected cost for MCC, PCC, and DAC obtained using these published correlations is shown in Table 10.

Table 10. Cost estimates of MCC, PCC, and DAC using Published Sherwood Plot Correlations ($/tonne CO_2 Captured)

Source	MCC (0.135 CO2)	PCC (0.12 CO2)	DAC (0.0004 CO2)
(House et al. 2011)	$5 - $50	$5 - $52	$1160 - $3620
(Wilcox 2012)	$22	$24	$2150

House et al. (2011) used their developed correlation to argue that DAC was unlikely to cost less than $1000 per tonne of CO_2 captured, with the possibility that it could cost significantly more. Using the same analysis, MCC, on the basis of high concentration of CO_2 in the exhaust stream, would carry a cost similar to that of post-combustion capture from coal power plants and significantly lower than DAC. Again, there is no theoretical basis for why DAC should represent a more viable strategy for mobile emissions mitigation than direct capture from fuel exhaust. However, theoretical estimates can vary significantly from actual costs. To more

precisely understand the expected costs of MCC and whether an MCC system is feasible it is necessary to look at the specifics of the proposed system.

4.3 Considerations for the Design of Mobile Carbon Capture Systems

As discussed in Chapter 1, a number of strategies exist for CO_2 capture from stationary power plants, including pre-combustion capture, post-combustion capture, and the use of oxy-fuel technologies. These strategies can be modified for use in mobile capture. The system proposed by Bilger and Woo (2009) is an example of an oxy-fuel system, where fuel is burned in pure oxygen and the resulting wet CO_2 gas stream can be easily purified and compressed. Damm and Fedorov (2008) and Kato, Otsuka, and Liu (2005) both proposed systems involving shift reactions of fuels, such as methane or methanol, to H_2 and CO_2. These systems are similar to the pre-combustion capture systems employed in stationary plants except the H_2 produced was assumed to power a fuel cell rather that a combustion process. In general, all of these systems require significant modification of the car engine and some necessitate storage of compressed gases, which may not be acceptable to consumers.

Sullivan and Sivak (2012) assumed that the first applications of CO_2 capture in vehicles would most likely be a post-combustion capture system, since these systems could be appended to the downstream management of exhaust gases without directly affecting the inputs to the internal combustion engine. For similar reasons, post-combustion capture is also assumed here. However, even if the CO_2 capture technology for MCC is narrowed down to post-combustion capture, there still remains a number of choices to be made with regard to the specifics of the capture system. The following section provides an overview of the various considerations that

go into the design of a mobile carbon capture system to separate CO_2 from the exhaust gas of vehicles.

4.3.1 CO_2 Produced in Automobiles by the Combustion of Gasoline

Gasoline has a density of ~0.755 kg/L (~6.30 lb/gal) and combustion of 1 gallon (~3.79 L) of gasoline results in ~8.89 kg of CO_2, or roughly 3.11 kg-CO_2/kg-gasoline. The density of CO_2 is similar to that of gasoline when the CO_2 is liquefied at high pressure (~0.74 kg/L at 90 bar and 30°C), meaning that the volume of the produced CO_2, if stored as a compressed liquid, would also be roughly three times the volume of the combusted gasoline. Automobile tanks are generally sized to provide ~350 miles of range meaning that gasoline tanks tend to vary from less than 10 gallons for high gas mileage vehicles to more than 20 gallons for low gas mileage vehicles. Combustion of a full tank of gas for current passenger vehicles will therefore produce anywhere from 80 to 160 kg of CO_2 and this produced CO_2, if stored as a compressed liquid, would take up 30 to 60 gallons of storage space. For comparison, a typical light duty vehicle might weight 1500 kg (~3300 lbs.) and have a cargo volume of approximately 264 gallons (~1000 L). On-board storage of the produced CO_2 would represent a significant weight and volume penalty to the vehicle. This is of concern because a 10% increase in vehicle mass results in a 5-9% reduction in vehicle fuel economy (An and Santini 2004; Cheah and Heywood 2011; Brooker, Ward, and Wang 2013). It is important to note that this weight penalty of the stored CO_2 does not include the weight, volume, and energy penalties associated with placing a capture system on a vehicle with the ability to produce a nearly pure stream of CO_2 at high pressure. On the other side, it is important to note that the U.S. Environmental Protection Agency and the Department of Transportation's National Highway Traffic Safety Administration have recently issued final rulings to further reduce greenhouse gas emissions

and improve fuel economy for light duty vehicles under the Clean Air Act and Energy Policy and Conservation Act, as amended by the Energy Independence and Security Act (EPA 2012):

> *"EPA's standards apply to passenger cars, light-duty trucks, and medium-duty passenger vehicles, for MYs [model years] 2017 through 2025. The final standards are projected to result in an average industry fleetwide level of 163 grams/mile of carbon dioxide (CO2) in model year 2025, which is equivalent to 54.5 miles per gallon (mpg) if achieved exclusively through fuel economy improvements."*

If the purported gas mileage improvements are achieved, the associated weight and volume penalties for mobile carbon capture would be reduced significantly.

4.3.2 Managing the Periodic Offloading of CO_2

Outside of waiting for regulated improvements in fuel economy, there are a number of other options for dealing with this expected weight penalty for capturing the produced CO_2. The most logical options are capture less CO_2 or offload the captured CO_2 more often. In their analysis, Sullivan and Sivak (2012) assumed the captured CO_2 would be offloaded during refueling based on assumptions about customer convenience. Between refueling, the captured CO_2 would be compressed and stored on-board the car, either in a separate storage tank or in a dual use gasoline/CO_2 tank. Under these assumptions, only about 33% of the produced CO_2 could be feasibly stored, significantly reducing the potential of MCC to reduce transportation emissions.

The other option, offloading the captured CO_2 more often, has not been explored in detail. One can imagine a system where consumers plug their vehicles into a home CO_2 recovery unit after their daily commutes, similar to plug-in electric vehicles. The captured CO_2 would be offloaded overnight and then incorporated into a pipeline system, paralleling the natural gas delivery system, or trucked weekly to collection facilities, in parallel with trash collection

systems. This arrangement could significantly increase the amount of CO_2 emissions mitigated while lowering the mass and volume requirements for the capture system on-board the vehicle. The drawback would be an increase in cost and complexity of the CO_2 transport infrastructure.

In order to understand the potential benefits of offloading the CO_2 during or after daily commutes rather than during refueling, it is important to understand the daily driving habits of individuals. The U.S. department of transportation conducts a national household travel survey (NHTS) (U.S. Department of Transportation 2009), which can be used to analyze how individuals use their vehicles in the U.S. (Krumm 2012). The 2009 NHTS contains detailed data on individual vehicle trips, which can be parsed to understand the impact that daily capture

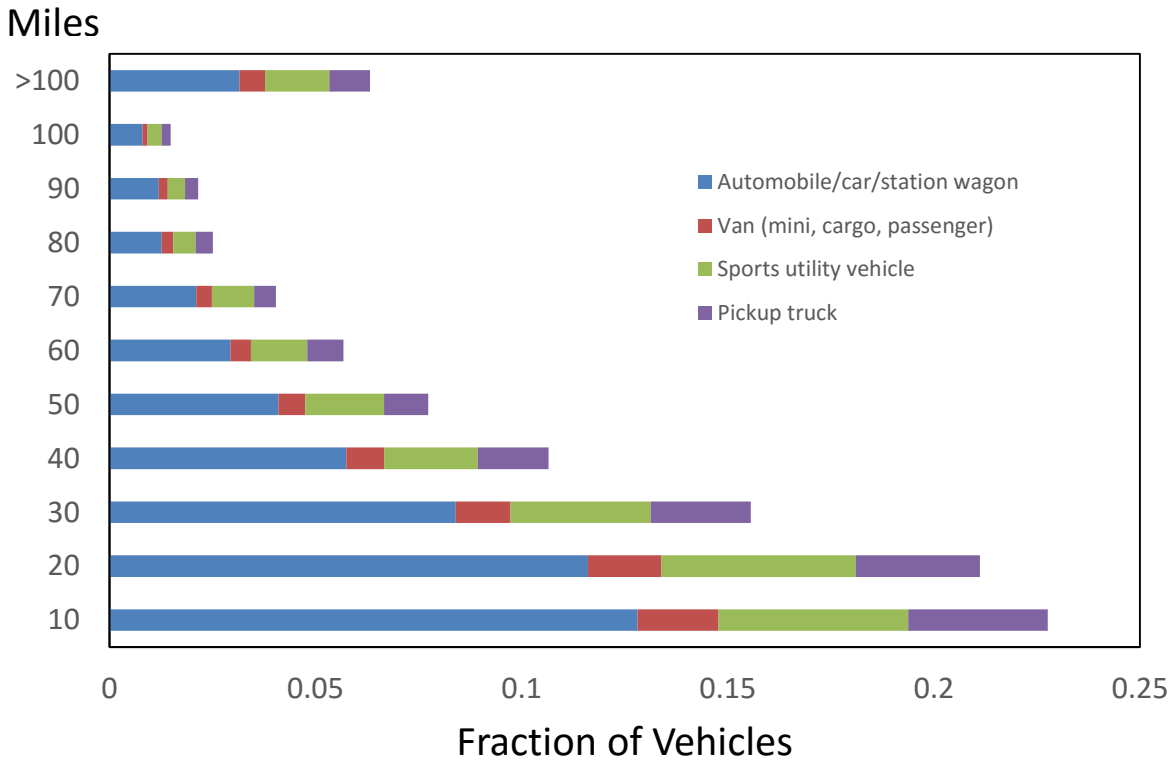

Figure 47. Daily miles driven as reported by drivers for specific vehicles. The vertical axis labels give the maximum of each histogram bin. The horizontal labels given the fraction of vehicles that were reported to drive a given bin distance daily. Vehicle types included are “automobile/car/station wagon” (Blue), “Van (mini, cargo, passenger)” (Red), “sports utility vehicle” (Green), and “pickup truck” (Purple). Vehicle types not included are “other truck”, “recreational vehicle”, “motorcycle”, “golf cart”, “refused to answer”, “don't know”, “not ascertained”, and “other”.

schemes might have on vehicle emissions. For more information on how to obtain custom statistics about personal vehicle travel from the National Household Travel Survey, the interested reader is encouraged to read the work by Krumm (2012). The specific query used in this chapter for data mining the NHTS is available in section 4.5.1. Figure 47 shows a histogram of daily miles driven reported by survey respondents for vehicles normally used for personal travel obtained from the 2009 NHTS. Approximately 60% of vehicles are driven less than 30 miles in a single day, and a significant percentage (~23%) of vehicles are driven less than 10 miles per day. This means the potential benefit of capturing the first few miles of daily travel is enormous.

Table 11 shows the potential emissions reductions achievable through MCC with daily offloading if the capture system was assumed to capture 100% of the first 10, 20, or 30 miles of emissions, with no capture after this initial capture distance. For driving distance histogram bins which exceed the capture distance but are less than 100 miles, capture is conservatively estimated as the capture distance divided by the maximum distance driven in that bin (e.g., for 30 mile capture in the 50 miles bin, which represents daily miles driven greater than 40 miles but less than or equal to 50 miles, the percent of emissions captured is estimated as 30 divided by 50, or 60%). For daily distances over 100 miles, 0% capture is assumed. Even when assuming only the first 10 daily miles are captured ($1/35^{th}$ of the vehicle's assumed driving range), vehicle emissions can be reduced by more than 43%, significantly more than the 33% proposed by Sullivan and Sivak (2012). For a daily capture distance of 30 miles, the emissions reduction could reach 80%. Such emissions reductions, combined with the fact that the onboard storage required would be far less, argue strongly for daily offloading of CO_2 over offloading during vehicle refueling.

Table 11. Potential Emissions Reductions Achievable Through Mobile Capture with Daily Offloading.

Vehicle Segment	NHTS Code*	Percent of Travel Emissions Saved if We Captured First		
		10 miles	20 miles	30 miles
Automobile/car/station wagon	01	46%	68%	80%
Van (mini, cargo, passenger)	02	44%	66%	77%
Sports utility vehicle	03	43%	66%	77%
Pickup truck	04	45%	67%	79%
Combined	01 - 04	45%	67%	79%

*Vehicle type designation used in the 2009 National Household Travel Survey. See section 4.5.1 for specific database queries used.

4.3.3 Powering the Capture System

So far we have assumed that a mobile carbon capture system would capture, separate, and compress CO_2 on-board the vehicle. This general type of system, referred to here as a Type-1 mobile carbon capture scheme (MCC-1), is not the only way to configure a mobile capture system. An alternative scheme is the capture of CO_2 on a sorbent, with the CO_2-loaded sorbent being periodically offloaded or regenerated using off-board power. This type of system is

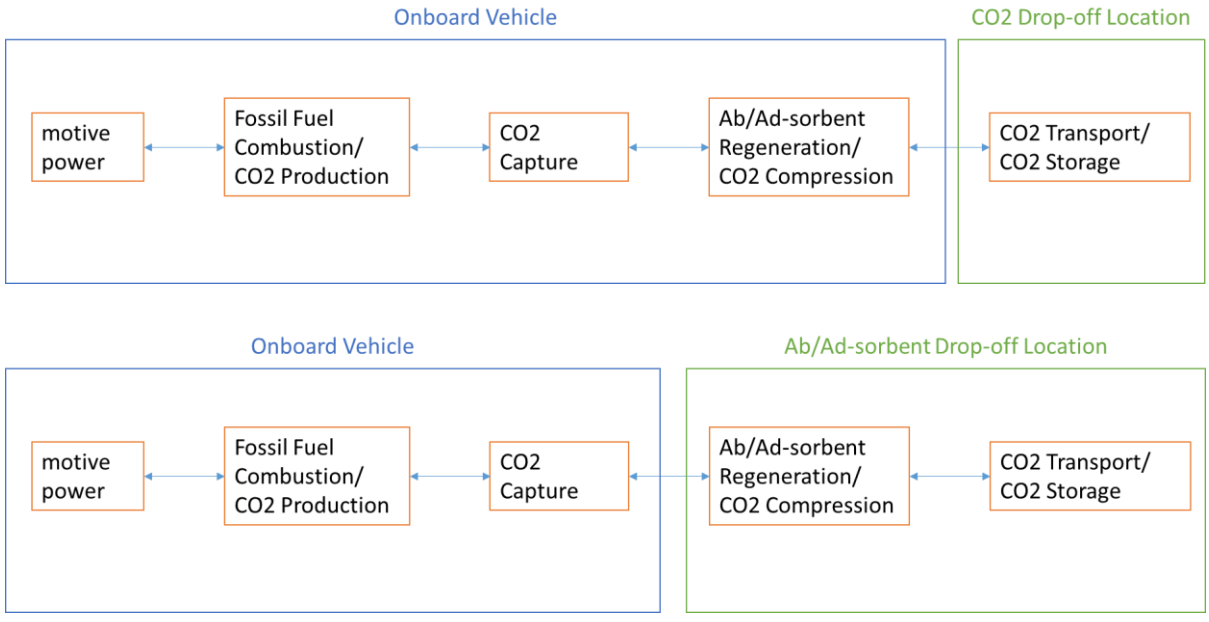

Figure 48. Two mobile carbon capture schemes: MCC-1 (Top) and MCC-2 (Bottom)

referred to here as a Type-2 mobile carbon capture scheme (MCC-2). These two systems are visually summarized in Figure 48.

When mentioned in the literature, MCC is generally assumed to follow the MCC-1 scheme. However, this may not be the most efficient MCC system design as it implies that the minimum work requirements for CO_2 capture discussed previously need to be overcome with work supplied by the car engine or battery. This drain of on-board power from the car is likely to impose significant efficiency penalties and severely hinder gas mileage which could lead to significant increases in the amount of CO_2 produced. In addition, due to its energy density and utility, gasoline tends to be more valuable than other fuels or power sources, which warns against using it as the source of power for a CO_2 capture system. In order to compare these two MCC schemes and determine which scheme is more viable, one can evaluate the overall cost of power to overcome the minimum work requirements for CO_2 capture as a first pass estimate of operating costs.

To develop this high level estimate of operating costs, it is necessary to make assumptions about the fraction of CO_2 captured, the expected second law efficiency of the separation process, and the cost of power. If power is being supplied off-board the car, the best case scenario would be to use CO_2-free electricity to power the separation and compression system, such as that supplied by wind turbines, hydro-power, or solar panels, in order to prevent additional emissions of CO_2. CO_2-free power tends to be more expensive than fossil fuel based power and is expected to range between 10¢ and 20¢ per kWh for the foreseeable future (House et al. 2011). If power is being supplied on-board the car, it can be assumed that the power source is the gasoline fed engine. Gasoline has an energy density of approximately 120 MJ/gallon. While electricity can be assumed to power the CO_2 separation system directly,

gasoline thermal energy would first have to be converted to equivalent work. The ideal thermal efficiency limit of internal combustion engines is approximately 38%, but the majority of gasoline vehicles achieve efficiencies significantly less than that, with typical tractive-load efficiencies ranging from 15-30% (An and Santini 2004). Gasoline in the U.S. has historically ranged in price from $2 to $4 per gallon. As discussed previously, second-law efficiencies for separation processes tend to range from 5-40%, although recent schemes using piperazine have been reported to reach overall second-law efficiencies for combined separation and compression of ~50% for stationary CO_2 capture at power plants (Rochelle et al. 2011). As mobile capture is a theoretical system, estimates of second law efficiencies of 5-25% for separation for 90% capture are likely appropriate. For comparison, DAC is generally expected to have second law efficiencies of <15% for 50% capture of CO_2 from ambient air.

Table 12 shows the overall cost of power to overcome the work requirements for CO_2 capture, assuming a range of second law efficiencies. A system powered with CO_2-free electricity off-board the car (equivalent to a MCC-2 scheme) would have costs for power ranging from $25 to $178 per tonne of CO_2 captured. A system powered using gasoline on-board the car (equivalent to a MCC-1 scheme) would have a cost for power roughly twice that, ranging from $49 to $357 per tonne of CO_2 captured, while DAC would have power costs above $92 per tonne of CO_2 captured under the best case scenario. The extra expense of gasoline powered separation, combined with the fact that the gasoline would no longer be available to drive motive power, suggests that there is no cost or operational benefit to attempting to fit a full separation and compression system on-board the vehicle. Such a system would simply represent additional technological hurdles to implementation, while leading to a higher cost system.

Table 12. Cost to overcome the work requirements of separation ($/tonne CO_2 captured) for DAC and MCC as a function of η_{2nd} and cost of power.

		CO_2-Free Electricity		Gasoline†	
System*	**η_{2nd}****	**$0.1/kWh**	**$0.2/kWh**	**$2/Gallon**	**$4/Gallon**
MCC	0.05	89	178	178	357
α = 0.9	0.15	35	71	71	141
	0.25	25	49	49	98
DAC	0.05	260	519	-	-
α = 0.5	0.15	92	184	-	-

*All systems were assumed to produce a CO_2 product stream at a pressure of 110 bar with a purity of 98%. α represents the fraction of CO_2 captured.
**Second-Law efficiency for separation. A second law efficiency for compression of 0.9 was assumed for all systems.
† A 30% thermal efficiency is assumed for the Gasoline Engine

4.3.4 Managing the Storage of CO_2 without Compression

Since there is an additional cost penalty associated with completing separation and compression of the captured CO_2 on-board the vehicle, it is important to consider options for storage of CO_2 without compression. If the CO_2 has been captured using a solid or liquid sorbent, then the obvious solution is simply to delay regeneration of the sorbent until the CO_2 or sorbent system can be off-loaded from the vehicle, which, as discussed previously, would benefit from being a daily occurrence. This type of system would remove the weight and energy penalties of having a regeneration and compression system on-board the vehicle but the trade-off would be a significant increase in the weight and volume of sorbent required for CO_2 capture. The magnitude of this penalty would depend on the specifics of the sorbent used, but the general trend can be observed based on weight percent (wt%) storage capacity for CO_2. To be clear, "wt%" here refers to the kg-CO_2/kg-sorbent definition commonly used for solid adsorbents, rather than the kg-CO_2/L-solution definition commonly used for liquid absorbents. For example, a 10 wt% sorbent, as defined here, would need 10 grams of sorbent material to store 1 gram of CO_2 for a total system mass during CO_2 storage of 11 grams, while a 100 wt%

sorbent would only need 1 gram of sorbent to store 1 gram of CO_2 for a total system mass of 2 grams. As discussed previously, each gram of gasoline produces ~3 grams of CO_2, so using a 10 wt% sorbent to capture that produced CO_2 would result in a total system mass of ~33 grams for each gram of gasoline consumed.

Figure 49 shows the generalized trend of system mass normalized to the amount of gasoline producing the captured emissions. As the wt% storage increases, the system mass asymptotically approaches the normalized mass of produced CO_2, which is 3 times the mass of the gasoline which produced it. As the wt% storage decreases, the system mass asymptotically approaches infinity. For comparison, liquid absorbents like monoethanolamine and piperazine solutions used in stationary carbon capture generally have wt% capacities for CO_2 of 5-20% depending on the molality of the solution (L. Li et al. 2013). Solid sorbents like alkali-metal oxides or metal-organic frameworks that have been proposed for carbon capture applications generally have capacities from 5-25% (Lee et al. 2012) although significantly higher wt% adsorption have been achieved experimentally. For example, calcium oxide can achieve 76 wt% at 600 °C and 100 kPa (Lee et al. 2012), while MOF-210 can achieve 250

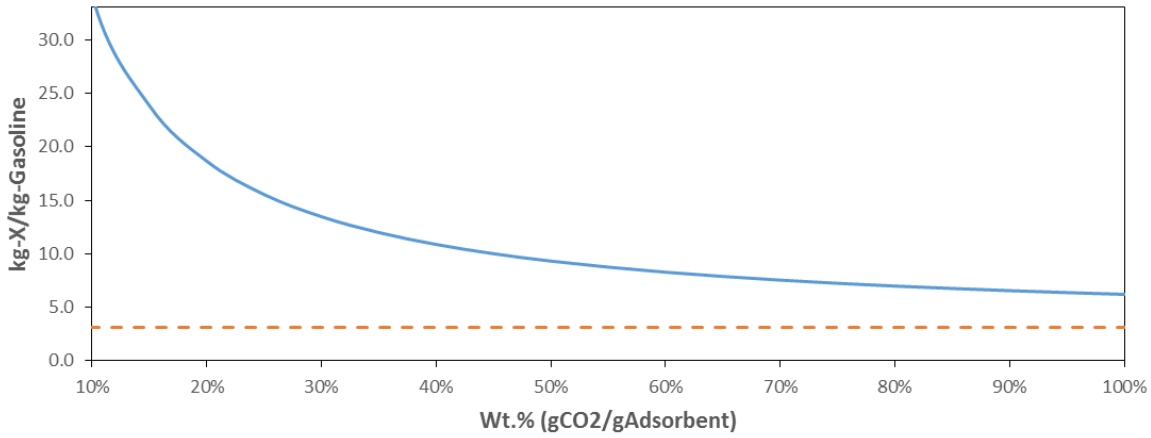

Figure 49. System mass (X) normalized to the provoking mass of gasoline consumed vs. the wt% storage capacity of the sorbent system.

wt% adsorption at 298 K and 50 bars of pressure (Furukawa et al. 2010). Clearly higher wt% adsorbents would be more amenable for use in mobile capture. In addition, higher density adsorbents would also be preferred, in order to minimize the volume penalty.

The relative volume required for sorbent storage onboard a vehicle can be generalized from the wt% of CO_2 storage and the density of the CO_2 loaded sorbent. This trend is summarized in Figure 51 in section 4.5.2. To be comparable in volume with CO_2 that has been liquefied at high pressure, sorbents for MCC application would need to combine both high storage capacity and high density. Although this combination of properties is not common in liquid sorbents, many solid sorbents, especially alkali-metal oxides, can theoretically store CO_2 at high density through the production of carbonates. For example, if produced CO_2 is stored through reactions with calcium oxides to produce calcium carbonate, the overall mass of the CO_2 storage system would be roughly 7 times that of the combusted gasoline. However, due to the higher density of solid $CaCO_3$ (~2.7 kg/L), the required volume is less than 2 times the volume of the combusted gasoline rather than 3 times as required for compressed CO_2.

Current practice has steered carbon capture materials towards low energy of adsorption and easy regeneration rather than towards maximizing wt% storage due to operational consideration at stationary plants. The optimum balance of wt% adsorption and easy regeneration for mobile capture applications is likely to differ significantly from stationary capture applications due to the weight and volume concerns associated with mobile capture and storage.

4.3.5 Management of Sorbent Packs

The previous section detailed the option of storing the CO_2 on a sorbent. Off-loading of the stored CO_2 could be accomplished by periodically regenerating the sorbent or swapping out

spent sorbent for fresh material. In the latter case it may become necessary to develop procedures for sorbent pack replacement. This type of process could be expected to parallel battery pack replacement strategies in electric vehicles, for which a number of patents have been developed (Hammerslag 1999; Merkle and Meyer 1978; Gwyn 1984; Aarseth 1999; Guimarin and Janik 1997; Chaney 2007). Due to concerns about system management, battery storage, and customer acceptance, battery swapping systems are not expected to see widespread use outside of public transportation, large managed systems, or long distance travel (Zheng et al. 2014; Andersen, Mathews, and Rask 2009; Frade et al. 2011). However, these types of swapping systems may be useful for sorbent management as the sorbent is not technically needed to operate the vehicle. Whereas a spent battery leads directly to restricted mobility, a fully loaded sorbent, as discussed by Sullivan and Sivak (2012), should not necessarily restrict refueling of the vehicle or general mobility. Additional CO_2 capture could simply be discontinued until a suitable discharge location was encountered. These sorbent packs could then be incorporated into a distribution and reclamation system that parallels trash collection systems, as discussed previously. Fresh sorbent packs could be delivered to the sorbent drop-off location, while loaded sorbent packs could be picked up and delivered by truck to local regeneration infrastructure for collection and disposal of the captured CO_2. An additional benefit of such a sorbent transfer system is that sorbent packs could be monitored for degradation or loss in CO_2 capacity and replaced with virgin or fresh material before being returned to the vehicle. This sorbent pack delivery system would likely result in additional carbon dioxide emissions depending on the distance traveled and carbon intensity of the transportation system. Mckinnon and Piecyk (2010) suggest an emission factor of 62 gCO_2-eq./tonne-kilometer for truck transport in the European chemical industry. The cost for truck

transport of sorbent is not known but could be expected to cost on the order of a few cents per tonne-kilometer. Note that the option of foregoing sorbent regeneration and simply landfilling or otherwise disposing of CO_2 loaded sorbent is one possible option for managing sorbent packs. Whether CO_2 sorbents are regenerated/reused or disposed of would depend on the cost of the sorbent and the environmental impacts associated with disposal balanced against the costs and impacts associated with sorbent regeneration.

4.3.6 Estimating Capital Costs

In addition to the operational costs of transportation and sorbent material regeneration, it is important to consider the capital costs associated with deploying an MCC system. As opposed to operational costs, which can be roughly estimated using the minimum work requirements, it is difficult to precisely estimate the capital costs of an undefined fictitious system. Instead, it is valuable to look at the ratio of capital expenditures to operational costs for similar systems.

In a technology assessment of direct air capture for the American Physical Society, Socolow et al. (2011) detailed the expected capital and operational costs for both post-combustion capture at power plants and direct air capture. They estimated that post-combustion capture would cost approximately $80 per ton of CO_2 avoided, with operating costs exceeding capital costs by more than half. For direct air capture, they estimated much higher costs of $610 per ton of CO_2 avoided, with capital costs exceeding operating costs by more than half. In the absence of knowing whether operating costs or capital costs will dominate the MCC system, it is logical to assume that capital costs will be roughly equivalent to operating costs, halfway between the ratios expected for PCC and DAC, at least for high level estimation purposes. This estimate of capital cost should include allowances for the initial purchase of the significant amounts sorbents required for CO_2 capture and transportation.

4.4 Cost of Mobile Carbon Capture

4.4.1 Baseline System

Given the discussion in the previous sections, it is now possible to imagine what a mobile capture system might look like and develop a high level estimate of cost. The model system is summarized in Table 13. Based on the assumptions in Table 13, the MCC system captures 3.56 kg/day of CO_2 on 17.8 kg of sorbent for a total daily system weight of 21.3 kg. Ignoring the weight of additional components but conservatively assuming that the system mass is invariant with time, the total mass penalty to the car is 1.42%. This mass penalty leads to an MPG penalty of 1.00% or a modified fuel economy of 49.5 MPG. Over a total period of 10 days (time between refueling) this results in 35.6 kg of captured CO_2, which is stored on 178 kg of adsorbent. The car consumes an additional 0.060 gallons/refueling due to the weight penalty, resulting in a gasoline consumption cost of $0.181/refueling and 0.536 kg/refueling of additional CO_2 emissions. Being an MCC-2 system, no additional penalties to the car are expected.

After being unloaded from the car, the CO_2 loaded sorbent would be trucked 50 kilometers to CO_2 management infrastructure and then the regenerated sorbent (sans CO_2) would be trucked back to the drop-off location for a roundtrip distance of 100 kilometers. This would result in truck transport cost of $4.89/refueling and 1.21 kg/refueling of additional CO_2 emissions. At the CO_2 management infrastructure the sorbent would be regenerated and the released CO_2 would be compressed using 0.478 kWh of CO_2-free energy per kg CO_2 captured, resulting in an additional $2.55/refueling, with no additional CO_2 being released. Assuming capital costs are 100% of compression and separation costs leads to an additional $2.55/refueling. Note that

the above calculations are provided with 3 significant digits not to imply additional accuracy but to allow the interested reader to follow the calculations easily.

Table 13. MCC System Parameters for Baseline Estimate of Cost

Model Car		
Car Weight	1500	kg
Fuel Economy	50	MPG
Refueling distance	300	miles
Daily commute	30	miles
Fuel CO_2 Intensity	8.89	kg-CO_2/gallon
Fuel Cost	3	$/gallon
MPG/Weight Equivalency	7	%/10% mass change
Model Capture/Separation/Compression System		
Capture Distance	20	miles/day
Sorbent Capacity	20	wt%
Minimum Work Separation	165	kJ/kg Captured
Minimum Work Compression (1 to 110 bar)	265	kJ/kg Captured
Overall η_{2nd} for separation/compression	25	%
Cost of CO_2-Free Power	0.15	$/kWh
Capital Costs	100	% of Separation/Compression Costs
Model Sorbent Transport System		
Truck Transport Cost	0.25	$/tonne-kilometer
Truck Transport Distance (One-Way)	50	Kilometers
Truck Transport CO_2 emissions	0.062	kgCO_2-eq/tonne-kilometer

Table 14. Summary of CO_2 Emissions and Costs for the Baseline MCC System.

Balance of CO_2 emissions		
Total CO_2 Captured	35.6	kg/refueling
Additional CO_2 emissions	1.75	kg/refueling
CO_2 Avoided	33.8	kg/refueling
Balance of Costs		
Operational Costs	7.62	$/refueling
Capital Costs	2.55	$/refueling
Total Cost (CO_2 Captured)	286	$/tonne
Total Cost (CO_2 Avoided)	301	$/tonne

Based on these calculations, the total cost of CO_2 capture is \$286 per tonne of CO_2 captured or \$301 per tonne of CO_2 avoided (Table 14). Of this cost, only 2% is experienced as additional fuel costs by the driver, 48% is trucking costs, while 50% is capital and operational costs of the CO_2 separation and compression infrastructure. This cost for MCC is significantly lower than the costs expected for DAC and only about 3.5 times the cost of stationary capture for coal power plants estimated by the American Physical Society (Socolow et al. 2011). The premium of MCC over stationary capture can mostly be attributed to the high cost to transport the sorbent and the conservative estimate of separation and compression costs. Given a properly design system, one might expect the cost for MCC to be only 2-5 times the cost of stationary capture at power plants, significantly lower than the 10 times estimated for DAC (Brandani 2012).

4.4.2 Sensitivity Analysis

A sensitivity analysis was performed in order to further investigate the impact of various parameters on the calculated cost of the MCC-2 system. The results of this sensitivity analysis are given in Figure 50. The cost estimate is most sensitive to the overall second law efficiency

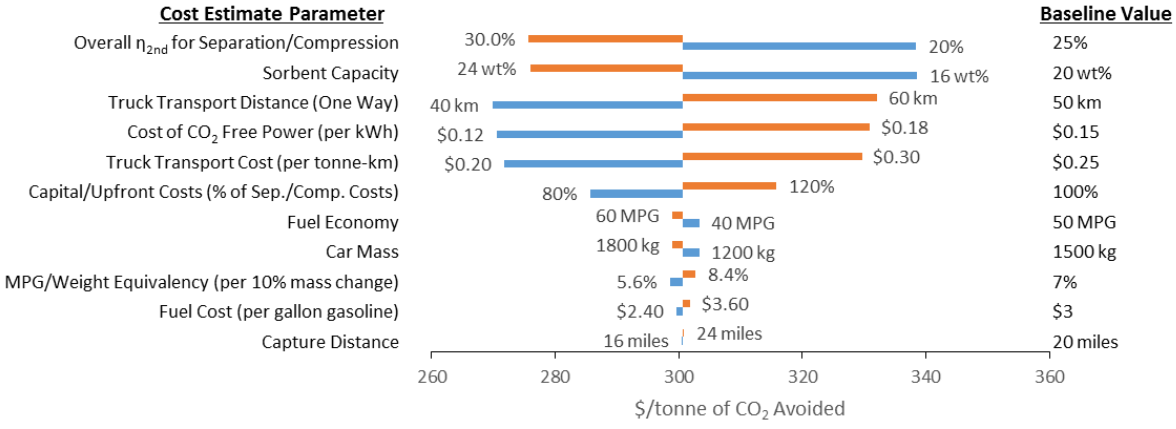

Figure 50. Sensitivity analysis of the cost estimate for the MCC-2 system. Parameter values were adjusted by ±20% of the baseline value.

for the separation and compression processes. This is not unexpected as the second-law efficiency is the basis for calculating both the power costs and the capital costs for the system, which make up 50% of the total cost for carbon capture in the MCC-2 system. The cost estimate is sensitive to the cost of CO_2-free power for similar reasons. The cost estimate is also sensitive to the parameters associated with truck transport costs, such as sorbent capacity, truck transport distance, and truck transport cost. This is also expected as the trucking costs are nearly comparable in magnitude to the power and capital costs for the system. Interestingly, for a mobile capture system, parameters associated with the actual car, such as fuel economy, car mass, MPG/weight equivalency, fuel cost, and capture distance, have relatively little impact on the system costs. This result highlights the fact that, in the system under study here, direct costs to the consumer during operation of the vehicle are only 2% of the total system costs. The total future cost for capture of CO_2 from distributed sources will be most dependent on the supporting CO_2 management infrastructure rather than on individual distributed capture devices.

4.4.3 Market Considerations

Given a suitable estimate for the costs of MCC, we can now explore the conditions under which MCC might be economically viable. All CO_2 capture technologies are dependent on mechanisms that assign a price or cost to carbon emissions. Sullivan and Sivak (2012) discussed a number of strategies to incentivize consumers to participate in MCC schemes such as the use of taxes, credits, deposits, or surcharges. The acceptability of MCC to consumers will depend on whether the price of MCC is lower than the costs associated with emitting the CO_2 or switching to an alternate form of transportation. Based on the carbon content of gasoline and allowing for well to tank emissions, each dollar-per-ton of CO_2 charge for CO_2 emissions

is equivalent to a surcharge of about one cent per gallon of gasoline (Socolow et al. 2011) meaning that a cost of $300 per tonne of CO_2 avoided roughly translates to a surcharge of approximately $3 per gallon of gasoline, which would double the cost of gasoline assumed for the cost estimate. This would represent a significant burden to the typical consumer.

The pricing of CO_2 could also be determine by markets under emissions trading schemes (ETS) like those being piloted in California, Canada, the European Union, Kazakhstan, and China. These schemes often involve a cap on the maximum number of emissions from the regulated industries within the region, with the ability of individual entities to sell allowances/permits that they do not need to entities that do need the emissions. Generally, the intention is for the maximum cap on emissions to be lowered over time such that the price of CO_2 drifts higher, forcing technological shifts. Carbon prices vary by region and market system. In California, the current traded market price for carbon allowance futures, as of April 14th, 2016, is $12.34 per tonne of CO_2 equivalents ("California Carbon Dashboard" 2016). This price for carbon dioxide emissions in California has remained relatively stable over the past two years. In China, four municipalities (Beijing, Chongqing, Shanghai and Tianjin), two provinces (Guangdong and Hubei) and the special economic zone of Shenzhen City are being used as pilot regions for ETS (De Boer, Roldao, and Slater 2015). In 2014 these markets experienced average prices ranging from 20 RMB (~$3) per tonne CO_2 in Tianjin to 60 RMB (~$9) per tonne CO_2 in Shenzen. Clearly these market prices are not high enough to support MCC at this point in time. However, it is expected that carbon prices will rise as emissions caps are lowered over time and that the expected price for MCC will fall as actual systems are developed and optimized.

4.5 Supporting Information

4.5.1 Sorbent Volume Requirements

Figure 51 shows the generalized trend of system volume with wt% storage of CO_2 and sorbent density.

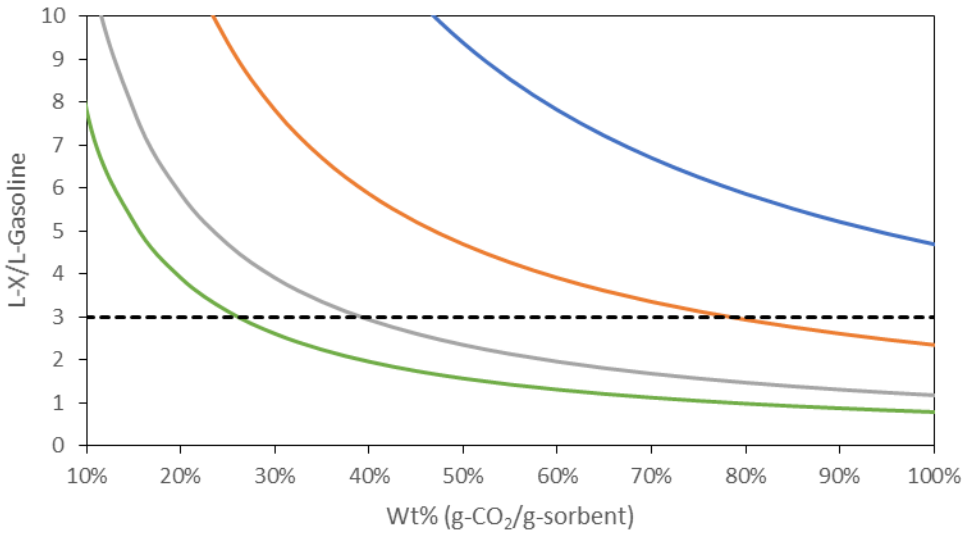

Figure 51. System Volume (X) normalized to the provoking volume of gasoline consumed vs. the wt% storage capacity of the sorbent system at sorbent densities (solid lines) of 0.5 g/ml (blue), 1 g/ml (orange), 2 g/ml (grey), and 3 mg/l (green). The approximate normalized volume of CO_2 when liquefied at high pressure is included for comparison (black dashed line).

4.5.2 SQL Statement used to Extract Statistics from NHTS

The following structured query language (SQL) code was used to extract statistics from the 2009 NHTS, specifically statistics related to daily travel distance, for individual cars within each household. The only table used was the "Travel Day Trip File", whose name is DAYV2PUB in the SQL statement. This table contains one record for each trip, and it was downloaded from http://nhts.ornl.gov/download.shtml.

The only vehicle types included are automobile/car/station wagon, van (mini, cargo, passenger), sports utility vehicle, and pickup truck. In order to avoid double counting, only trips where the survey respondent was the driver of the vehicle are included. In addition, the code ignores trips whose duration (TRVL_MIN) or distance (TRPMILES) was negative, indicating that the number was not available. The SQL code is provided to eliminate any ambiguity in how the statistics were derived. The SQL code is specifically for use with Microsoft Access.

```
SELECT DAYV2PUB.HOUSEID, DAYV2PUB.VEHID, DAYV2PUB.VEHTYPE,
Sum(DAYV2PUB.TRVL_MIN) AS DailyTravelMinutes, Sum(DAYV2PUB.TRPMILES) AS
DailyTravelMiles, Avg(DAYV2PUB.WTTRDFIN) AS WeightAverage
FROM DAYV2PUB
WHERE (((DAYV2PUB.[DRVR_FLG])=1) AND ((DAYV2PUB.[VEHTYPE]) In (1,2,3,4))
AND ((DAYV2PUB.[TRVL_MIN])>=0) AND ((DAYV2PUB.[TRPMILES])>=0))
GROUP BY DAYV2PUB.HOUSEID, DAYV2PUB.VEHID, DAYV2PUB.VEHTYPE;
```

CHAPTER 5

Conclusion

5.1 Summary of Current Work

Emissions of greenhouse gases into the atmosphere represent a long-term social and environmental challenge. Fossil fuels, which are the main source of these emissions, will likely continue to be used in energy production and transportation for the foreseeable future. In order to mitigate these emissions and prevent the worst potential effects of climate change, cheap, effective, and socially acceptable carbon capture technologies will need to reach widespread use across various industries. In this dissertation, two technologies were explored in detail to assess their potential for use in next-generation carbon capture and storage systems.

5.1.1 Flexible Frameworks as Next Generation Carbon Capture Materials

The first technology, flexible metal-organic frameworks, represent alternative materials for carbon capture. It has been suggested by previous authors that flexible frameworks, which exhibit exotic adsorption behaviors, could represent an improvement over the current standard, amine-based absorbents, due to their low energy of regeneration. In this work, two other aspects that affect the potential of flexible frameworks for carbon capture, performance under exposure to unwanted trace gases and breakthrough performance, were explored using elastic layered metal organic frameworks (ELMs) as a representative class of materials.

The ability of ELMs to maintain their structure and capture performance in the presence of unwanted trace species present in flue gas streams, such as NO_x, SO_x, and water vapor, was explored in Chapter 2 using both experimental and computational techniques. Of the two ELM variants explored experimentally, ELM-11 was found to lose CO_2 capacity with each cycle of water vapor exposure. In contrast, ELM-12 retained CO_2 capacity through at least four exposure cycles. Using density functional theory, it was found that molecules with strong dipoles, like H_2O, SO_2, and H_2S, show stronger binding energies on ELM frameworks than quadrupolar molecules like CO_2 and N_2. However, by leveraging the tunability of metal organic frameworks, the impact of these strongly binding molecules could be reduced. Replacing the copper vertex with nickel or cobalt lowered binding energies, while changing the counter ion from the simple tetrafluoroborate (BF_4^-) to the larger and more complex trifluoromethanesulfonate ($CF_3SO_3^-$) could limit the impact of competitive adsorption between gas molecules.

The breakthrough performance of flexible frameworks was explored in Chapter 3, using ELM-11 as a representative example. ELM-11 shows a "stepped" breakthrough curve that is not seen in rigid adsorbents, but is representative of the breakthrough curves of flexible frameworks. This experimentally observed step was a function of temperature, pressure, and mixture composition. To understand this unexpected phenomenon from a theoretical level, the level of the breakthrough curve step was compared with expected gate pressures obtained from osmotic framework absorbed solution theory (OFAST), which has previously been shown to correctly predict the gating transition in flexible frameworks. It was found that the OFAST method could be used to predict the expected step level from single component isotherms, supporting the theory that the step level is a function of the gating transition of flexible frameworks. In

addition, it was observed that mixing gas species with small kinetic diameter like helium into the gas stream could lead to lower than expected step levels. This was attributed to trace adsorption of the smaller gas species, which helped to prop open the ELM-11 layer structure, leading to lower gate pressures. This phenomenon was termed the “door-stop” effect.

In summary, this work shows that ELMs, and by extension flexible frameworks, can indeed be tailored for robust performance in flue gas streams, removing one of the potential concerns about their use as carbon capture materials. However, this work also highlights a potential trade-off regarding their exotic isotherms. While it is indeed possible to easily regenerate flexible frameworks, the trade-off is an unwanted step in the breakthrough curve. This step level makes it difficult for flexible frameworks to capture large percentages of the CO_2 from the flue gas stream, unless their gating transition is finely tuned to the particular conditions under which capture occurs.

5.1.2 Mobile Carbon Capture as a Next Generation Carbon Capture Strategy

The second technology, mobile carbon capture, represents an alternative strategy for mitigating emissions from the transportation sector. The thermodynamic minimum work to separate CO_2 from the exhaust stream of vehicles was found to be similar to that of stationary power and significantly less than that of competing direct air capture. It was determined that a mobile system which captures carbon dioxide from the first 30 miles of a vehicle’s daily commute and is regenerated daily could reduce emissions from automobiles in the U.S. by 80%. Under conservative assumptions, these significant reductions in CO_2 emissions could be achieved for a cost on the order of $300 per tonne of CO_2 avoided, significantly cheaper than the $600-$1000 per tonne of CO_2 expected for direct air capture. The majority of the cost premium over stationary capture at power plants was attributed to the high costs of sorbent transport. Based

on the analysis performed in this work, it is expected that mobile capture will carry a cost two to five times greater than that of stationary capture, which is still significantly less than the tenfold cost increase estimated for direct air capture.

In summary, the disdain for mobile carbon capture observed in the literature is unwarranted. Although mobile capture would indeed be more expensive than capture at large stationary sources like power plants, it would be significantly cheaper to implement than alternative mitigation schemes like direct air capture, which suffer from significant thermodynamic penalties.

5.2 Suggestions for Future Work

5.2.1 *In Situ* Structural Analysis and Performance under Realistic Conditions

In this work, two ELM variants were cyclically exposed to water vapor using pure water isotherms at room temperature. The conditions of these static experiments diverge significantly from the realities of CO_2 capture, which is likely to occur in high temperature flue gas streams with low absolute humidity in flow-through systems. The logical next step of analysis is to test the capture performance of ELMs using breakthrough curves of humidified gases to understand whether low absolute humidity would limit some of the worst impacts of water vapor exposure and whether the impact of water vapor exposure is sensitive to the temperature at which exposure occurs. Given that ELMs and other flexible frameworks have crystal structures that are highly sensitive to atmospheric conditions, analysis of the structural degradation or stability of ELMs would benefit from experiments that involve X-ray diffraction or IR-spectroscopy measurements performed *in situ*, as opposed to the measurements that were reported in this dissertation, which were obtained before and after, but not during, water vapor exposure.

5.2.2 Exploration of Size Exclusion and the "Door-Stop" Effect in ELMs

In this dissertation, ideal adsorbed solution theory (IAST) was used to determine mixture co-adsorption for use during application of OFAST models to the gating transition in ELM-11. Mixed-gas modeling techniques like IAST are often used to predict mixed gas adsorption in novel materials, to determine their suitability for carbon capture applications. However, as shown in this work, flexible frameworks show a special sensitivity to the adsorbing gas mixture, with both differences in molecule size and type affecting the likelihood that gating transitions will occur. This can lead to significant deviation from OFAST estimates based on IAST, even those that use rigid approximations of the expanded framework. These deviations were attributed to either size exclusion or the "door-stop" effect. In order to better understand these effects, the breakthrough curve experiments should be expanded to other gas mixtures where the molecules differ significantly in size and interaction type in order to generate general guidelines for when, and by how much, deviations from theory-based estimates will occur.

5.2.3 Prototyping Mobile Carbon Capture and Assessing its Potential for Market Penetration

In Chapter 4, a high level estimate of cost was developed for mobile carbon capture. This cost estimate depended on a number of broad assumptions, as no real system currently exists. Specific costs associated with material choice, or system design, were not included or explored in any detail. The next logical step is to explore the various material choices and capture designs which could be implemented on board a vehicle, with the goal of developing a workable prototype, in order to better assess the potential capital and upfront costs that would be borne by consumers. In addition, it would be important to understand how quickly these system could penetrate the vehicle market and obtain market share, considering the various consumer mobility options and in the context of various policy schemes. The importance of

mobile capture as an emission reduction strategy may depend on whether market penetration can occur at a fast enough pace to impact regional or global emissions at the time scales associated with mitigating global climate change.

REFERENCES

Aarseth, Einar. 1999. Electric vehicle service center and method for exchanging and charging vehicle batteries. U.S. Patent 5,998,963, issued December 7, 1999.

An, Feng, and Danilo J Santini. 2004. "Mass Impacts on Fuel Economies of Conventional vs. Hybrid Electric Vehicles." In *SAE Technical Paper*. SAE International. doi:10.4271/2004-01-0572.

Andersen, Poul H., John A. Mathews, and Morten Rask. 2009. "Integrating Private Transport into Renewable Energy Policy: The Strategy of Creating Intelligent Recharging Grids for Electric Vehicles." *Energy Policy* 37 (7): 2481–86. doi:10.1016/j.enpol.2009.03.032.

Baciocchi, Renato, Giuseppe Storti, and Marco Mazzotti. 2006. "Process Design and Energy Requirements for the Capture of Carbon Dioxide from Air." *Chemical Engineering and Processing: Process Intensification* 45 (12): 1047–58. doi:10.1016/j.cep.2006.03.015.

Bae, Youn-Sang, and Randall Q Snurr. 2011. "Development and Evaluation of Porous Materials for Carbon Dioxide Separation and Capture." *Angewandte Chemie (International Ed. in English)* 50 (49): 11586–96. doi:10.1002/anie.201101891.

Bilger, Robert W., and Zhijun Wu. 2009. "Carbon Capture for Automobiles Using Internal Combustion Rankine Cycle Engines." *Journal of Engineering for Gas Turbines and Power* 131 (3). American Society of Mechanical Engineers: 034502. doi:10.1115/1.3077657.

Blake, Alexander J, Stuart J Hill, Peter Hubberstey, and Wan-sheung Li. 1997. "Rectangular Grid Two-Dimensional Sheets of copper(II) Bridged by Both Co-Ordinated and Hydrogen Bonded 4,4′-Bipyridine (4,4′-Bipy) in [Cu(μ-4,4′-bipy)(H2O)2(FBF3) 2]·4,4′-Bipy." *Journal of the Chemical Society, Dalton Transactions*, no. 6: 913–14. doi:10.1039/a700036g.

Boot-Handford, Matthew E., Juan C. Abanades, Edward J. Anthony, Martin J. Blunt, Stefano Brandani, Niall Mac Dowell, José R. Fernández, et al. 2014. "Carbon Capture and Storage Update." *Energy Environ. Sci.* 7 (1). Royal Society of Chemistry: 130–89. doi:10.1039/C3EE42350F.

Bousquet, David, François-Xavier Coudert, Alexandre G J Fossati, Alexander V Neimark, Alain H Fuchs, and Anne Boutin. 2013. "Adsorption Induced Transitions in Soft Porous Crystals: An Osmotic Potential Approach to Multistability and Intermediate Structures." *The Journal of Chemical Physics* 138 (17): 174706. doi:10.1063/1.4802888.

Boutin, Anne, François-Xavier Coudert, Marie-Anne Springuel-Huet, Alexander V Neimark, Gérard Férey, and Alain H Fuchs. 2010. "The Behavior of Flexible MIL-53(Al) upon CH 4 and CO 2 Adsorption." *The Journal of Physical Chemistry C* 114 (50): 22237–44. doi:10.1021/jp108710h.

Brandani, Stefano. 2012. "Carbon Dioxide Capture from Air: A Simple Analysis." Edited by Simon Shackley and Elisabeth Dütschke. *Energy & Environment* 23 (2-3). Multi Science Publishing: 319–28. doi:10.1260/0958-305X.23.2-3.319.

Brooker, Aaron David, Jacob Ward, and Lijuan Wang. 2013. "Lightweighting Impacts on Fuel Economy, Cost, and Component Losses." *SAE World Congress & Exhibition, SAE Paper 2013-01-0381* 2013-01-03. doi:10.4271/2013-01-0381.

"California Carbon Dashboard." 2016. Accessed April 16. http://calcarbondash.org/.

Chaney, George T. 2007. Electric vehicle chassis with removable battery module and a method for battery module replacement. U.S. Patent 7,201,384, issued April 10, 2007.

Cheah, Lynette, and John Heywood. 2011. "Meeting U.S. Passenger Vehicle Fuel Economy Standards in 2016 and beyond." *Energy Policy* 39 (1): 454–66. doi:10.1016/j.enpol.2010.10.027.

Cheng, Yan, Hiroshi Kajiro, Hiroshi Noguchi, Atsushi Kondo, Tomonori Ohba, Yoshiyuki Hattori, Katsumi Kaneko, and Hirofumi Kanoh. 2011. "Tuning of Gate Opening of an Elastic Layered Structure MOF in CO2 Sorption with a Trace of Alcohol Molecules." *Langmuir : The ACS Journal of Surfaces and Colloids* 27 (11): 6905–9. doi:10.1021/la201008v.

Cheng, Yan, Atsushi Kondo, Hiroshi Noguchi, Hiroshi Kajiro, Koki Urita, Tomonori Ohba, Katsumi Kaneko, and Hirofumi Kanoh. 2009. "Reversible Structural Change of Cu-MOF on Exposure to Water and Its CO2 Adsorptivity." *Langmuir : The ACS Journal of Surfaces and Colloids* 25 (8): 4510–13. doi:10.1021/la803818p.

Coudert, François-Xavier. 2010. "The Osmotic Framework Adsorbed Solution Theory: Predicting Mixture Coadsorption in Flexible Nanoporous Materials." *Physical Chemistry Chemical Physics : PCCP* 12 (36): 10904–13. doi:10.1039/c003434g.

Coudert, François-Xavier, Anne Boutin, Marie Jeffroy, Caroline Mellot-Draznieks, and Alain H Fuchs. 2011. "Thermodynamic Methods and Models to Study Flexible Metal-Organic Frameworks." *Chemphyschem : A European Journal of Chemical Physics and Physical Chemistry* 12 (2): 247–58. doi:10.1002/cphc.201000590.

Coudert, François-Xavier, Marie Jeffroy, Alain H Fuchs, Anne Boutin, and Caroline Mellot-Draznieks. 2008. "Thermodynamics of Guest-Induced Structural Transitions in Hybrid Organic-Inorganic Frameworks." *Journal of the American Chemical Society* 130 (43): 14294–302. doi:10.1021/ja805129c.

Coudert, François-Xavier, Caroline Mellot-Draznieks, Alain H Fuchs, and Anne Boutin. 2009. "Prediction of Breathing and Gate-Opening Transitions upon Binary Mixture Adsorption in Metal-Organic Frameworks." *Journal of the American Chemical Society* 131 (32): 11329–31. doi:10.1021/ja904123f.

D'Alessandro, Deanna M, Berend Smit, and Jeffrey R Long. 2010. "Carbon Dioxide Capture: Prospects for New Materials." *Angewandte Chemie (International Ed. in English)* 49 (35): 6058–82. doi:10.1002/anie.201000431.

Dahmus, Jeffrey B., and Timothy G. Gutowski. 2007. "What Gets Recycled: An Information Theory Based Model for Product Recycling." *Environmental Science & Technology* 41 (21). American Chemical Society: 7543–50. doi:10.1021/es062254b.

Damm, David L., and Andrei G. Fedorov. 2008. "Conceptual Study of Distributed CO2 Capture and the Sustainable Carbon Economy." *Energy Conversion and Management* 49 (6): 1674–83. doi:10.1016/j.enconman.2007.11.011.

Dangi, Ganga P., Renjith S. Pillai, Rajesh S. Somani, Hari C. Bajaj, and Raksh V. Jasra. 2010. "A Density Functional Theory Study on the Interaction of Hydrogen Molecule with MOF-177." *Molecular Simulation* 36 (5): 373–81. doi:10.1080/08927020903487404.

De Boer, Dimitri, Renato Roldao, and Huw Slater. 2015. "The 2015 China Carbon Pricing Survey." *China Carbon Forum*.

DeCicco, John M. 2013. "Factoring the Car-Climate Challenge: Insights and Implications." *Energy Policy* 59 (August): 382–92. doi:10.1016/j.enpol.2013.03.052.

———. 2015. "The Liquid Carbon Challenge: Evolving Views on Transportation Fuels and Climate." *Wiley Interdisciplinary Reviews: Energy and Environment* 4 (1): 98–114. doi:10.1002/wene.133.

EIA. 2015. "Annual Energy Outlook 2015." U.S. Energy Information Administration, Washington, D.C. https://www.eia.gov/forecasts/aeo/pdf/0383%282015%29.pdf.

EPA. 2012. "EPA and NHTSA Set Standards to Reduce Greenhouse Gases and Improve Fuel Economy for Model Years 2017-2025 Cars and Light Trucks." https://www3.epa.gov/otaq/climate/documents/420f12051.pdf.

———. 2016. "Draft Inventory of U.S. Greenhouse Gas Emissions and Sinks: 1990-2014." U.S. Environmental Protection Agency. https://www3.epa.gov/climatechange/ghgemissions/usinventoryreport.html.

Férey, Gérard, and Christian Serre. 2009. "Large Breathing Effects in Three-Dimensional Porous Hybrid Matter: Facts, Analyses, Rules and Consequences." *Chemical Society Reviews* 38 (5): 1380–99. doi:10.1039/b804302g.

Finsy, Vincent, Christine E a Kirschhock, Gill Vedts, Michael Maes, Luc Alaerts, Dirk E De Vos, Gino V Baron, and Joeri F M Denayer. 2009. "Framework Breathing in the Vapour-Phase Adsorption and Separation of Xylene Isomers with the Metal-Organic Framework MIL-53." *Chemistry (Weinheim an Der Bergstrasse, Germany)* 15 (31): 7724–31. doi:10.1002/chem.200802672.

Finsy, Vincent, L. Ma, L. Alaerts, D.E. De Vos, G.V. Baron, and J.F.M. Denayer. 2009. "Separation of CO2/CH4 Mixtures with the MIL-53(Al) Metal–organic Framework." *Microporous and Mesoporous Materials* 120 (3). Elsevier Inc.: 221–27. doi:10.1016/j.micromeso.2008.11.007.

Frade, Inês, Anabela Ribeiro, Gonçalo Gonçalves, and António Antunes. 2011. "Optimal Location of Charging Stations for Electric Vehicles in a Neighborhood in Lisbon, Portugal." *Transportation Research Record: Journal of the Transportation Research Board* 2252 (December). Transportation Research Board of the National Academies: 91–98. doi:10.3141/2252-12.

Fukuhara, Katsuo, Shin-ichiro Noro, Kunihisa Sugimoto, Tomoyuki Akutagawa, Kazuya Kubo, and Takayoshi Nakamura. 2013. "Porous Coordination Polymer Polymorphs with Different Flexible Pores Using a Structurally Flexible and Bent 1,3-bis(4-Pyridyl)propane Ligand." *Inorganic Chemistry* 52 (8): 4229–37. doi:10.1021/ic301949n.

Furukawa, Hiroyasu, Kyle E Cordova, Michael O'Keeffe, and Omar M Yaghi. 2013. "The Chemistry and Applications of Metal-Organic Frameworks." *Science (New York, N.Y.)* 341 (6149): 1230444. doi:10.1126/science.1230444.

Furukawa, Hiroyasu, Nakeun Ko, Yong Bok Go, Naoki Aratani, Sang Beom Choi, Eunwoo Choi, A Ozgür Yazaydin, et al. 2010. "Ultrahigh Porosity in Metal-Organic Frameworks." *Science (New York, N.Y.)* 329 (5990): 424–28. doi:10.1126/science.1192160.

Gaussian 09. 2010. *Revision C.01, M. J. Frisch, G. W. Trucks, H. B. Schlegel, G. E. Scuseria, M. A. Robb, J. R. Cheeseman, G. Scalmani, V. Barone, B. Mennucci, G. A. Petersson, H. Nakatsuji, M. Caricato, X. Li, H. P. Hratchian, A. F. Izmaylov, J. Bloino, G. Zheng, J. L. Son*. Gaussian, Inc., Wallingford CT.

Goeppert, Alain, Miklos Czaun, G. K. Surya Prakash, and George A. Olah. 2012. "Air as the Renewable Carbon Source of the Future: An Overview of CO2 Capture from the Atmosphere." *Energy & Environmental Science* 5 (7). Royal Society of Chemistry: 7833. doi:10.1039/c2ee21586a.

Grajciar, Lukáš, Andrew D Wiersum, Philip L Llewellyn, Jong-san Chang, and Petr Nachtigall. 2011. "Understanding CO2 Adsorption in CuBTC MOF: Comparing Combined DFT–ab Initio Calculations with Microcalorimetry Experiments." *The Journal of Physical Chemistry C* 115 (36): 17925–33. doi:10.1021/jp206002d.

Gücüyener, Canan, Johan van den Bergh, Jorge Gascon, and Freek Kapteijn. 2010. "Ethane/ethene Separation Turned on Its Head: Selective Ethane Adsorption on the Metal-Organic Framework ZIF-7 through a Gate-Opening Mechanism." *Journal of the American Chemical Society* 132 (50): 17704–6. doi:10.1021/ja1089765.

Guimarin, David C, and Wayne M Janik. 1997. Battery exchange system for electric vehicles. U.S. Patent 5,612,606, issued March 18, 1997.

Gwyn, Marion V. 1984. Battery replacement system for electric vehicles. U.S. Patent 4,450,400, issued May 22, 1984.

Hammerslag, Julius G. 1999. Battery charging and transfer system for electrically powered vehicles. U.S. Patent 5,951,229, issued September 14, 1999.

Hamon, Lomig, Philip L Llewellyn, Thomas Devic, Aziz Ghoufi, Guillaume Clet, Vincent Guillerm, Gerhard D Pirngruber, et al. 2009. "Co-Adsorption and Separation of CO2-CH4 Mixtures in the Highly Flexible MIL-53(Cr) MOF." *Journal of the American*

Chemical Society 131 (47): 17490–99. doi:10.1021/ja907556q.

Haszeldine, R Stuart. 2009. “Carbon Capture and Storage: How Green Can Black Be?” *Science (New York, N.Y.)* 325 (5948): 1647–52. doi:10.1126/science.1172246.

Heidel, Kenton, David Keith, Arvinder Singh, and Geoff Holmes. 2011. “Process Design and Costing of an Air-Contactor for Air-Capture.” *Energy Procedia* 4: 2861–68. doi:10.1016/j.egypro.2011.02.192.

Holmes, Geoffrey, and David W Keith. 2012. “An Air-Liquid Contactor for Large-Scale Capture of CO2 from Air.” *Philosophical Transactions. Series A, Mathematical, Physical, and Engineering Sciences* 370 (1974): 4380–4403. doi:10.1098/rsta.2012.0137.

Horike, Satoshi, Yasutaka Inubushi, Takashi Hori, Tomohiro Fukushima, and Susumu Kitagawa. 2012. “A Solid Solution Approach to 2D Coordination Polymers for CH4/CO2 and CH4/C2H6 Gas Separation: Equilibrium and Kinetic Studies.” *Chemical Science* 3 (1): 116. doi:10.1039/c1sc00591j.

Horike, Satoshi, Satoru Shimomura, and Susumu Kitagawa. 2009. “Soft Porous Crystals.” *Nature Chemistry* 1 (9): 695–704. doi:10.1038/nchem.444.

House, Kurt Zenz, Antonio C Baclig, Manya Ranjan, Ernst A van Nierop, Jennifer Wilcox, and Howard J Herzog. 2011. “Economic and Energetic Analysis of Capturing CO2 from Ambient Air.” *Proceedings of the National Academy of Sciences of the United States of America* 108 (51): 20428–33. doi:10.1073/pnas.1012253108.

House, Kurt Zenz, Charles F. Harvey, Michael J. Aziz, and Daniel P. Schrag. 2009. “The Energy Penalty of Post-Combustion CO2 Capture & Storage and Its Implications for Retrofitting the U.S. Installed Base.” *Energy & Environmental Science* 2 (2): 193. doi:10.1039/b811608c.

IEA. 2008. *Energy Technology Perspectives 2008: Scenarios and Strategies to 2050*. Energy Technology Perspectives. OECD Publishing. doi:10.1787/9789264041431-en.

IPCC. 2013. “Summary for Policymakers.” In *Climate Change 2013 - The Physical Science Basis*, edited by Intergovernmental Panel on Climate Change, 1–30. Cambridge: Cambridge University Press. doi:10.1017/CBO9781107415324.004.

Jiang, Yijiao, Jun Huang, Besnik Kasumaj, Gunnar Jeschke, Michael Hunger, Tamas Mallat, and Alfons Baiker. 2009. “Adsorption-Desorption Induced Structural Changes of Cu-MOF Evidenced by Solid State NMR and EPR Spectroscopy.” *Journal of the American Chemical Society* 131 (6): 2058–59. doi:10.1021/ja8088718.

Jones, Christopher W. 2011. “CO(2) Capture from Dilute Gases as a Component of Modern Global Carbon Management.” *Annual Review of Chemical and Biomolecular Engineering* 2 (January). Annual Reviews: 31–52. doi:10.1146/annurev-chembioeng-061010-114252.

Kajiro, Hiroshi, Atsushi Kondo, Katsumi Kaneko, and Hirofumi Kanoh. 2010. “Flexible Two-Dimensional Square-Grid Coordination Polymers: Structures and Functions.” *International Journal of Molecular Sciences* 11 (10): 3803–45. doi:10.3390/ijms11103803.

Kanoh, Hirofumi, Atsushi Kondo, Hiroshi Noguchi, Hiroshi Kajiro, Aya Tohdoh, Yoshiyuki Hattori, Wei-Chun Xu, et al. 2009. “Elastic Layer-Structured Metal Organic Frameworks (ELMs).” *Journal of Colloid and Interface Science* 334 (1). Elsevier Inc.: 1–7. doi:10.1016/j.jcis.2009.03.020.

Kato, Y., K. Otsuka, and C.Y. Liu. 2005. “Carbon Dioxide Zero-Emission Hydrogen Carrier System for Fuel Cell Vehicle.” *Chemical Engineering Research and Design* 83 (7): 900–904. doi:10.1205/cherd.04321.

Keith, David W., Minh Ha-Duong, and Joshuah K. Stolaroff. 2005. “Climate Strategy with Co2 Capture from the Air.” *Climatic Change* 74 (1-3): 17–45. doi:10.1007/s10584-005-9026-x.

Kitagawa, Susumu, Ryo Kitaura, and Shin-ichiro Noro. 2004. “Functional Porous Coordination Polymers.” *Angewandte Chemie (International Ed. in English)* 43 (18): 2334–75. doi:10.1002/anie.200300610.

Kitagawa, Susumu, and Ryotaro Matsuda. 2007. “Chemistry of Coordination Space of Porous Coordination Polymers.” *Coordination Chemistry Reviews* 251 (21-24): 2490–2509. doi:10.1016/j.ccr.2007.07.009.

Kizzie, Austin C, Antek G Wong-Foy, and Adam J Matzger. 2011. “Effect of Humidity on the Performance of Microporous Coordination Polymers as Adsorbents for CO2 Capture.” *Langmuir : The ACS Journal of Surfaces and Colloids* 27 (10): 6368–73. doi:10.1021/la200547k.

Kondo, Atsushi, Ayako Chinen, Hiroshi Kajiro, Tomohiro Nakagawa, Kenichi Kato, Masaki Takata, Yoshiyuki Hattori, et al. 2009. “Metal-Ion-Dependent Gas Sorptivity of Elastic Layer-Structured MOFs.” *Chemistry (Weinheim an Der Bergstrasse, Germany)* 15 (31): 7549–53. doi:10.1002/chem.200901208.

Kondo, Atsushi, Hiroshi Kajiro, Hiroshi Noguchi, Lucia Carlucci, Davide M Proserpio, Gianfranco Ciani, Kenichi Kato, et al. 2011. “Super Flexibility of a 2D Cu-Based Porous Coordination Framework on Gas Adsorption in Comparison with a 3D Framework of Identical Composition: Framework Dimensionality-Dependent Gas Adsorptivities.” *Journal of the American Chemical Society* 133 (27): 10512–22. doi:10.1021/ja201170c.

Kondo, Atsushi, Hiroshi Noguchi, Lucia Carlucci, Davide M Proserpio, Gianfranco Ciani, Hiroshi Kajiro, Tomonori Ohba, Hirofumi Kanoh, and Katsumi Kaneko. 2007. “Double-Step Gas Sorption of a Two-Dimensional Metal-Organic Framework.” *Journal of the American Chemical Society* 129 (41): 12362–63. doi:10.1021/ja073568h.

Kondo, Atsushi, Hiroshi Noguchi, Shunsuke Ohnishi, Hiroshi Kajiro, Aya Tohdoh, Yoshiyuki Hattori, Wei-Chun Xu, Hideki Tanaka, Hirofumi Kanoh, and Katsumi Kaneko. 2006. “Novel Expansion/shrinkage Modulation of 2D Layered MOF Triggered by Clathrate Formation with CO(2) Molecules.” *Nano Letters* 6 (11): 2581–84. doi:10.1021/nl062032b.

Krumm, John. 2012. “How People Use Their Vehicles: Statistics from the 2009 National Household Travel Survey.” In . doi:10.4271/2012-01-0489.

Lackner, K. S., S. Brennan, J. M. Matter, A.- H. A. Park, A. Wright, and B. van der Zwaan. 2012. “The Urgency of the Development of CO2 Capture from Ambient Air.” *Proceedings of the National Academy of Sciences* 109 (33): 13156–62. doi:10.1073/pnas.1108765109.

Lackner, K.S. 2009. “Capture of Carbon Dioxide from Ambient Air.” *The European Physical Journal Special Topics* 176 (1): 93–106. doi:10.1140/epjst/e2009-01150-3.

Lee, Zhi Hua, Keat Teong Lee, Subhash Bhatia, and Abdul Rahman Mohamed. 2012. “Post-Combustion Carbon Dioxide Capture: Evolution towards Utilization of Nanomaterials.” *Renewable and Sustainable Energy Reviews* 16 (5). Elsevier Ltd: 2599–2609. doi:10.1016/j.rser.2012.01.077.

Li, Di, and Katsumi Kaneko. 2001. “Hydrogen Bond-Regulated Microporous Nature of Copper Complex-Assembled Microcrystals.” *Chemical Physics Letters* 335 (1-2): 50–56. doi:10.1016/S0009-2614(00)01419-6.

Li, Jian-Rong, Yuguang Ma, M. Colin McCarthy, Julian Sculley, Jiamei Yu, Hae-Kwon Jeong, Perla B. Balbuena, and Hong-Cai Zhou. 2011. “Carbon Dioxide Capture-Related Gas Adsorption and Separation in Metal-Organic Frameworks.” *Coordination Chemistry Reviews* 255 (15-16). Elsevier B.V.: 1791–1823. doi:10.1016/j.ccr.2011.02.012.

Li, Le, Han Li, Omkar Namjoshi, Yang Du, and Gary T. Rochelle. 2013. “Absorption Rates and CO2 Solubility in New Piperazine Blends.” *Energy Procedia* 37: 370–85. doi:10.1016/j.egypro.2013.05.122.

Liu, Jian, Praveen K Thallapally, B Peter McGrail, Daryl R Brown, and Jun Liu. 2012. “Progress in Adsorption-Based CO2 Capture by Metal-Organic Frameworks.” *Chemical Society Reviews* 41 (6): 2308–22. doi:10.1039/c1cs15221a.

Martin, Marcus G. 2013. “MCCCS Towhee: A Tool for Monte Carlo Molecular Simulation.” *Molecular Simulation* 39 (14-15). Taylor & Francis: 1212–22. doi:10.1080/08927022.2013.828208.

Martin, Marcus G., and J. Ilja Siepmann. 1998. “Transferable Potentials for Phase Equilibria. 1. United-Atom Description of N-Alkanes,” March. American Chemical Society. doi:10.1021/jp972543+.

MATLAB and Statistics Toolbox. 2015. *Version 8.5.0 (R2015a)*. The MathWorks, Inc., Natick, Massachusetts, United States.

Mayo, Stephen L., Barry D. Olafson, and William A. Goddard. 1990. “DREIDING: A Generic Force Field for Molecular Simulations.” *The Journal of Physical Chemistry* 94 (26). American Chemical Society: 8897–8909. doi:10.1021/j100389a010.

McKinnon, Alan Campbell, and Maja Piecyk. 2010. “Measuring and Managing CO2 Emissions in European Chemical Transport.” *CEFLC*.

Mehio, Nada, Sheng Dai, and De-en Jiang. 2014. “Quantum Mechanical Basis for Kinetic Diameters of Small Gaseous Molecules,” January. American Chemical Society. doi:10.1021/jp412588f.

Merkle, Theodor, and Paul Meyer. 1978. Apparatus for positioning battery-operated road vehicles at battery replacement stations. U.S. Patent 4,102,273, issued July 25, 1978.

Myers, A L, and J M Prausnitz. 1965. “Thermodynamics of Mixed-Gas Adsorption.” *AIChE Journal* 11 (1): 121–27. doi:10.1002/aic.690110125.

Neimark, Alexander V., François-Xavier Coudert, Anne Boutin, and Alain H. Fuchs. 2010. “Stress-Based Model for the Breathing of Metal−Organic Frameworks.” *The Journal of Physical Chemistry Letters* 1 (1): 445–49. doi:10.1021/jz9003087.

Nijem, Nour, Peter Thissen, Yanpeng Yao, Roberto C Longo, Katy Roodenko, Haohan Wu, Yonggang Zhao, et al. 2011. “Understanding the Preferential Adsorption of CO2 over N2 in a Flexible Metal-Organic Framework.” *Journal of the American Chemical Society* 133 (32): 12849–57. doi:10.1021/ja2051149.

Noguchi, Hiroshi, Atsushi Kondo, Yoshiyuki Hattori, Hiroshi Kajiro, Hirofumi Kanoh, and Katsumi Kaneko. 2007. “Evaluation of an Effective Gas Storage Amount of Latent Nanoporous Cu-Based Metal-Organic Framework.” *Journal of Physical Chemistry C* 111 (1): 248–54. doi:10.1021/jp064035i.

Noguchi, Hiroshi, Atsushi Kondoh, Yoshiyuki Hattori, Hirofumi Kanoh, Hiroshi Kajiro, and Katsumi Kaneko. 2005. “Clathrate-Formation Mediated Adsorption of Methane on Cu-Complex Crystals.” *The Journal of Physical Chemistry. B* 109 (29): 13851–53. doi:10.1021/jp052515o.

Noro, Shin-ichiro, Yuh Hijikata, Munehiro Inukai, Tomohiro Fukushima, Satoshi Horike, Masakazu Higuchi, Susumu Kitagawa, Tomoyuki Akutagawa, and Takayoshi Nakamura. 2013. “Highly Selective CO2 Adsorption Accompanied with Low-Energy Regeneration in a Two-Dimensional Cu(II) Porous Coordination Polymer with Inorganic Fluorinated PF6(-) Anions.” *Inorganic Chemistry* 52 (1): 280–85. doi:10.1021/ic301823j.

Notz, R. J., I. Tönnies, N. McCann, G. Scheffknecht, and H. Hasse. 2011. “CO2 Capture for Fossil Fuel-Fired Power Plants.” *Chemical Engineering & Technology* 34 (2): 163–72. doi:10.1002/ceat.201000491.

Ortiz, Aurélie U, Marie-Anne Springuel-Huet, François-Xavier Coudert, Alain H Fuchs, and Anne Boutin. 2012. “Predicting Mixture Coadsorption in Soft Porous Crystals: Experimental and Theoretical Study of CO2/CH4 in MIL-53(Al).” *Langmuir : The ACS Journal of Surfaces and Colloids* 28 (1): 494–98. doi:10.1021/la203925y.

Pielke, Roger A. 2009. “An Idealized Assessment of the Economics of Air Capture of Carbon Dioxide in Mitigation Policy.” *Environmental Science & Policy* 12 (3): 216–25. doi:10.1016/j.envsci.2009.01.002.

Pires, J.C.M., F.G. Martins, M.C.M. Alvim-Ferraz, and M. Simões. 2011. “Recent Developments on Carbon Capture and Storage: An Overview.” *Chemical Engineering Research and Design* 89 (9). Institution of Chemical Engineers: 1446–60. doi:10.1016/j.cherd.2011.01.028.

Potoff, Jeffrey J., and J. Ilja Siepmann. 2001. “Vapor–liquid Equilibria of Mixtures Containing Alkanes, Carbon Dioxide, and Nitrogen.” *AIChE Journal* 47 (7): 1676–82.

doi:10.1002/aic.690470719.

Pritchard, C., A. Yang, P. Holmes, and M. Wilkinson. 2015. “Thermodynamics, Economics and Systems Thinking: What Role for Air Capture of CO2?” *Process Safety and Environmental Protection* 94 (March): 188–95. doi:10.1016/j.psep.2014.06.011.

Ramsahye, N.A., G Maurin, S Bourrelly, P.L. Llewellyn, C Serre, T Loiseau, T Devic, and G. Ferey. 2008. “Probing the Adsorption Sites for CO2 in Metal Organic Frameworks Materials MIL-53 (Al, Cr) and MIL-47 (V) by Density Functional Theory.” *Journal of Physical Chemistry C* 112 (2): 514–20. doi:10.1021/jp075782y.

Rana, Malay Kumar, Hyun Seung Koh, Haroon Zuberi, and Donald J Siegel. 2014. “Methane Storage in Metal-Substituted Metal–Organic Frameworks: Thermodynamics, Usable Capacity, and the Impact of Enhanced Binding Sites.” *The Journal of Physical Chemistry C* 118 (6): 2929–42. doi:10.1021/jp4104273.

Rochelle, Gary, Eric Chen, Stephanie Freeman, David Van Wagener, Qing Xu, and Alexander Voice. 2011. “Aqueous Piperazine as the New Standard for CO2 Capture Technology.” *Chemical Engineering Journal* 171 (3): 725–33. doi:10.1016/j.cej.2011.02.011.

Ruthven, Douglas M. 2014. “CO2 Capture: Value Functions, Separative Work and Process Economics.” *Chemical Engineering Science* 114 (July): 128–33. doi:10.1016/j.ces.2014.04.020.

Seifritz, W. 1993. “Partial and Total Reduction of CO2 Emissions of Automobiles Using CO2 Traps☆.” *International Journal of Hydrogen Energy* 18 (3): 243–51. doi:10.1016/0360-3199(93)90026-7.

Serre, Christian, Sandrine Bourrelly, Alexandre Vimont, Naseem a. Ramsahye, Guillaume Maurin, Philip L. Llewellyn, Marco Daturi, et al. 2007. “An Explanation for the Very Large Breathing Effect of a Metal–Organic Framework during CO2 Adsorption.” *Advanced Materials* 19 (17): 2246–51. doi:10.1002/adma.200602645.

Serre, Christian, Franck Millange, Christelle Thouvenot, Marc Noguès, Gérard Marsolier, Daniel Louër, and Gérard Férey. 2002. “Very Large Breathing Effect in the First Nanoporous Chromium(III)-Based Solids: MIL-53 or Cr III (OH)·{O 2 C−C 6 H 4 −CO 2 }·{HO 2 C−C 6 H 4 −CO 2 H} X ·H 2 O Y.” *Journal of the American Chemical Society* 124 (45): 13519–26. doi:10.1021/ja0276974.

Sing, K. S. W. 1985. “Reporting Physisorption Data for Gas/solid Systems with Special Reference to the Determination of Surface Area and Porosity (Recommendations 1984).” *Pure and Applied Chemistry* 57 (4). doi:10.1351/pac198557040603.

Socolow, Robert, Michael Desmond, Roger Aines, Jason Blackstock, Olav Bolland, Tina Kaarsberg, Nathan Lewis, Marco Mazzotti, Allen Pfeffer, and Karma Sawyer. 2011. “Direct Air Capture of CO2 with Chemicals: A Technology Assessment for the APS Panel on Public Affairs.” American Physical Society.

Sugiyama, Hayato, Satoshi Watanabe, Hideki Tanaka, and Minoru T Miyahara. 2012. “Adsorption-Induced Structural Transition of an Interpenetrated Porous Coordination Polymer: Detailed Exploration of Free Energy Profiles.” *Langmuir : The ACS Journal of*

Surfaces and Colloids 28 (11): 5093–5100. doi:10.1021/la205063f.

Sullivan, John M., and Michael Sivak. 2012. "CARBON CAPTURE IN VEHICLES: A REVIEW OF GENERAL SUPPORT, AVAILABLE MECHANISMS, AND CONSUMER-ACCEPTANCE ISSUES," no. May.

Sumida, Kenji, David L Rogow, Jarad a Mason, Thomas M McDonald, Eric D Bloch, Zoey R Herm, Tae-Hyun Bae, and Jeffrey R Long. 2012. "Carbon Dioxide Capture in Metal-Organic Frameworks." *Chemical Reviews* 112 (2): 724–81. doi:10.1021/cr2003272.

Tanaka, Hideki, Shotaro Hiraide, Atsushi Kondo, and Minoru T. Miyahara. 2015. "Modeling and Visualization of CO 2 Adsorption on Elastic Layer-Structured Metal–Organic Framework-11: Toward a Better Understanding of Gate Adsorption Behavior." *The Journal of Physical Chemistry C* 119 (21). American Chemical Society: 11533–43. doi:10.1021/jp512870p.

Taylor, Kathleen C. 1993. "Nitric Oxide Catalysis in Automotive Exhaust Systems." *Catalysis Reviews* 35 (4). Taylor & Francis Group: 457–81. doi:10.1080/01614949308013915.

The Royal Society. 2009. "Geoengineering the Climate: Science, Governance and Uncertainty." https://royalsociety.org/~/media/Royal_Society_Content/policy/publications/2009/8693.pdf.

Torrisi, Antonio, Caroline Mellot-Draznieks, and Robert G Bell. 2009. "Impact of Ligands on CO2 Adsorption in Metal-Organic Frameworks: First Principles Study of the Interaction of CO2 with Functionalized Benzenes. I. Inductive Effects on the Aromatic Ring." *The Journal of Chemical Physics* 130 (19): 194703. doi:10.1063/1.3120909.

———. 2010. "Impact of Ligands on CO(2) Adsorption in Metal-Organic Frameworks: First Principles Study of the Interaction of CO(2) with Functionalized Benzenes. II. Effect of Polar and Acidic Substituents." *The Journal of Chemical Physics* 132 (4): 044705. doi:10.1063/1.3276105.

Tran, Trinh D. 2012. "Molecular Simulation of Carbon Dioxide Capture on Elastic Layered Metal-Organic Framework Adsorbents." (Doctoral Dissertation). University of Michigan. http://deepblue.lib.umich.edu/bitstream/2027.42/94064/1/tdtrinh_1.pdf.

Triguero, Carles, François-Xavier Coudert, Anne Boutin, Alain H Fuchs, and Alexander V Neimark. 2011. "Mechanism of Breathing Transitions in Metal–Organic Frameworks." *The Journal of Physical Chemistry Letters* 2 (16): 2033–37. doi:10.1021/jz2008769.

U.S. Department of Transportation, Federal Highway Administration. 2009. "National Household Travel Survey." http://nhts.ornl.gov.

Watanabe, Satoshi, Hayato Sugiyama, Hirobumi Adachi, Hideki Tanaka, and Minoru T Miyahara. 2009. "Free Energy Analysis for Adsorption-Induced Lattice Transition of Flexible Coordination Framework." *The Journal of Chemical Physics* 130 (16): 164707. doi:10.1063/1.3122988.

Wilcox, Jennifer. 2012. *Carbon Capture*. Springer Science & Business Media. https://books.google.com/books?hl=en&lr=&id=CAh3HF4z6XoC&pgis=1.

Yang, Yue, Michael N Weaver, and Kenneth M Merz. 2009. “Assessment of the ‘6-31+G** + LANL2DZ’ mixed Basis Set Coupled with Density Functional Theory Methods and the Effective Core Potential: Prediction of Heats of Formation and Ionization Potentials for First-Row-Transition-Metal Complexes.” *The Journal of Physical Chemistry. A* 113 (36). American Chemical Society: 9843–51. doi:10.1021/jp807643p.

Yu, Jiamei, Yuguang Ma, and Perla B Balbuena. 2012. “Evaluation of the Impact of H2O, O2, and SO2 on Postcombustion CO2 Capture in Metal-Organic Frameworks.” *Langmuir : The ACS Journal of Surfaces and Colloids* 28 (21): 8064–71. doi:10.1021/la3009514.

Zeman, Frank. 2007. “Energy and Material Balance of CO 2 Capture from Ambient Air.” *Environmental Science & Technology* 41 (21). American Chemical Society: 7558–63. doi:10.1021/es070874m.

———. 2014. “Reducing the Cost of Ca-Based Direct Air Capture of CO 2.” *Environmental Science & Technology* 48 (19). American Chemical Society: 11730–35. doi:10.1021/es502887y.

Zhao, Ming, Andrew I. Minett, and Andrew T. Harris. 2013. “A Review of Techno-Economic Models for the Retrofitting of Conventional Pulverised-Coal Power Plants for Post-Combustion Capture (PCC) of CO2.” *Energy & Environmental Science* 6 (1): 25. doi:10.1039/c2ee22890d.

Zheng, Yu, Zhao Yang Dong, Yan Xu, Ke Meng, Jun Hua Zhao, and Jing Qiu. 2014. “Electric Vehicle Battery Charging/Swap Stations in Distribution Systems: Comparison Study and Optimal Planning.” *IEEE Transactions on Power Systems* 29 (1): 221–29. doi:10.1109/TPWRS.2013.2278852.